The Dissertation Committee for Jaime Guillermo Plazas Tuttle Certifies that this is the approved version of the following dissertation:

Nano-Enabled Water Disinfection Technology Development that Harnesses the Power of Microwaves

Committee:

Navid B. Saleh, Supervisor

Benny D. Freeman

Lynn E. Katz

Mary J. Kirisits

Desmond F. Lawler

Nano-Enabled Water Disinfection Technology Development that Harnesses the Power of Microwaves

by

Jaime Guillermo Plazas Tuttle, B.S.; M.S.; M.S.

Dissertation

Presented to the Faculty of the Graduate School of

The University of Texas at Austin

in Partial Fulfillment

of the Requirements

for the Degree of

Doctor of Philosophy

The University of Texas at Austin

May 2017

Dedication

To the memory of my late father Jaime and my mother Sarita

To my wife Adriana

All good things that have come to my life have been because of your example and guidance Papá, affection and comprehension Mamá, unconditional love, emotional support, and patience Adri.

Acknowledgements

I would like to express my admiration, appreciation, and gratitude to my supervisor, Dr. Navid Saleh, for his guidance and mentorship, all the way from when I was first considering joining his group in South Carolina to completion of this degree. Dr. Saleh's intellectual heft is matched only by his genuinely good nature and down-to-earth humility, and I am truly fortunate to have had the opportunity to work with him.

It has been an honor and a pleasure to take classes from Dr. Desmond Lawler, Dr. Lynn Katz, and Dr. Mary Jo Kirisits, and to have them in my committee. I am also fortunate to be able to claim myself as a part of the EWRE program at UT. Thank you for all your feedback, help, and inspiration. I would also like to thank Dr. Benny Freeman for taking the time to carefully read and evaluate my dissertation and provide valuable feedback during the proposal and final defense.

To all the friends that I have met and have been there when I needed them the most. Manga and Gustavo who helped us find the way. To my friends of parranda, tertulia, extreme activities, support and cheering group, Farith, Carlos and Marifer, and Silvia; they were always there. Leo Gutierrez thanks for helping us start in Illinois.

My deepest gratitude to all who have in one way or another contributed to this journey, especially my research group members Nirupam Aich, Dipesh Das, Lewis Stetson Rowles III, and Indu Venu Sabaraya. I am fortunate to have worked with such a kind group. I would like to extend my gratitude to my EWRE colleagues and the departmental staff.

To my mother and late father for their eternal love and unconditional support. Papá, you passed away soon after I embarked on this project, but I have always felt your presence next to me. Mamita, thank you for always being there, and always be caring through your never-ending love.

To my family-in-law, Lourdes and Oscar for their affection and for being so supportive.

To my wife Adriana, thank you for all your patience, sacrifice, understanding, support, and encouragement. I adore you. We have had difficult times and only you, the person that has walked beside me, know how difficult it has been. But now, it is a new dawn and we can continue this journey with renewed strengths and new objectives. If there is fairness in this world, you should also receive a doctoral degree for enduring this journey besides me.

Special acknowledgements to Universidad de los Andes for their support, and Fulbright, Colciencias-DNP for the scholarship.

Nano-Enabled Water Disinfection Technology Development that Harnesses the Power of Microwave

Jaime Guillermo Plazas Tuttle, Ph.D.

The University of Texas at Austin, 2017

Supervisor: Navid B. Saleh

Due to the position of microwave (MW) radiation in the electromagnetic spectrum, it has not yet been successfully utilized to inactivate waterborne microorganisms at a reasonable (energy) cost. Exceptional properties at the nano-scale, namely MW absorption-abilities of carbon nanotubes and excellent spectral conversion-capabilities of lanthanide series metal oxides in concert, hold promise to overcome the energetic barrier of this widely used and affordable MW technology. This dissertation reports the synthesis of a nano-heterostructure that combines carbon nanotubes' and erbium oxides' properties to generate reactive oxygen species (ROS) and inactivate *Pseudomonas aeruginosa*. Detailed characterization of the synthesized nanohybrid (NH) material with electron microscopy, X-ray techniques, and thermal gravimetric analysis confirms effective hybridization. At least one log unit of microbial inactivation was achieved via ROS generation with only 20 s of microwave irradiation at 110 W (0.0006 kW·h energy use), using a conventional MW oven. Inactivation studies with ROS scavenger molecules prove that generated oxygen species played the dominant role in bacterial inactivation. The roles of wavelength, input power, and irradiation time on inactivation are explored, in an effort to unlock the mechanism of inactivation. To achieve such results with a high degree of control, a setup including a MW power

generator and waveguide, capable of delivering precise frequency, while controlling input power and irradiation exposure time, has been designed and constructed. Results demonstrate inactivation of *P. aeruginosa* in presence of MW irradiation and aided by the nanohybrids. Finally, the inactivation efficacy of MW spectral conversion for a wide range of waterborne microorganism is determined. Inactivation of *Legionella pneumophila*, *Flavobacterium columnare*, *Bacillus subtilis* spores, and MS2 bacteriophages was also attempted using this system. A low degree of inactivation varying between (0.38 to 4.13 log removal) was achieved. These initial results are promising, but they do demonstrate a need for redesign of the NH and and reconsideration of the key irradiation parameters to achieve higher log removal, which will enable development of a technology that will be elevated from an agent of inactivation to an enabler of disinfection.

Table of Contents

List of Tables xiii

List of Figures xiv

List of Symbols and Abbreviations xxi

Chapter 1: Introduction 1

1.1 Introduction to the Study 1

1.2 Objectives and Hypotheses 5

1.3 Research Vision and Plan 6

1.4 Dissertation Structure 7

Chapter 2: Multifunctional Properties of NHs 9

2.1 Introduction 9

2.2 Literature Review 9

2.3 Principle for Discerning ANHs 13

2.4 Classification of ANHs 14

2.4.1 pH-Responsive 17

2.4.2 Thermo-Responsive 19

2.4.3 Photo-Responsive 21

2.4.4 Multi-, Bio-, and Other-stimuli Responsive Nano-Systems 23

2.5 EHS Implications 24

2.6 Carbon Nanotube Responses to Microwave Radiation 32

2.7 Key Findings 34

Chapter 3: Harnessing the Power of Microwave for Inactivation with Nanohybrids 36

3.1 Introduction 36

3.2 Experimental 38

3.2.1 Materials 38

3.2.2 Synthesis of NHs 38

3.2.3 NHs Characterization 39

3.2.4 Disinfection Potency 40
3.2.5 Disinfection Mechanism Determination 41
Measuring Temperature Change 41
Determination of H_2O_2 Concentration 42
ROS Scavengers 42
3.2.6 Enhanced Inactivation Performance 43
3.3 Results and Discussion 44
3.3.1 Synthesis and Characterization of the NHs 44
3.3.2 Disinfection Potency 47
3.3.3 Proposed Disinfection Mechanisms 50
Dissolution of metal ions 50
Microwave Heating 51
Synergistic Effects of combined MW heating and ROS species 52
ROS-Mediated Microbial Inactivation 52
ROS scanvenger study 54
Enhanced Inactivation Performance Results 55
3.3.4 Possible ROS-Generation Mechanisms 56
3.3.5 Key Findings 60

Chapter 4: Exploration of the Roles of Wavelength and Irradiation Time of MW on Inactivation Potency of *P. aeruginosa* 61
4.1 Introduction 61
4.1.1 MW Frequency and Wavelength 62
4.1.2 Waveguide 63
Cutoff frequency 65
Material Selection for the Sample Vessel 67
4.2 Experimental 68
4.2.1 Microwave Power Generator 68
4.2.2 MW waveguide 69
4.2.3 Bacterial Propagation 71
4.2.4 Inactivation Efficiency 71

4.2.5 Experimental Matrix 73
4.3 Results and Discussion 74
4.3.1 Baseline Measurements 74
4.3.2 Bacterial Inactivation Results and Optimization 77
4.3.3 Key Findings 79

Chapter 5: Evaluation of Inactivation Efficacy for a Wide Range of Waterborne Microorganisms 80
5.1 Introduction 80
5.1.1 Selected Microorganisms 81
Bacillus subtilis 81
Legionella pneumophila 82
MS2 bacteriophage 82
Flavobacterium columnare 83
5.2 Experimental 85
5.2.1 Materials 85
5.2.2 Preparation of Bacterial and Viral Strains 85
5.2.3 Inactivation Efficiency 86
5.3 Results and Discussion 89
5.3.1 *B. subtilis* inactivation 89
5.3.2 *L. pneumophila* inactivation 91
5.3.3 *F. columnare* inactivation 93
5.3.4 MS2 inactivation 94
5.3.5 Key Findings 96

Chapter 6: Conclusions and Recommendations 97
Future Work 101

Appendices 104
Appendix A – Tables 104
Appendix B – Figures 106
Appendix C – ROS Generation 112
Appendix D – Electronic Structure of Metal Oxides 114

Appendix E – Growth Media Formulations....118
Anacker and Ordal medium....118
ATCC Medium: 1099 CYE Buffered Medium....118
ATCC Medium: 271 Escherichia Medium....119
2X SG medium – Sporulation of B. subtilis....119
References....120
Vita....139

List of Tables

Table 4.1: Experimental matrix. MW frequency was maintained at 2445, 2450, and 2455 MHz. 73

Table 4.2: Sample temperature changes after irradiation at different frequencies, MW power, and irradiation intervals (1X = 20 s, 3X = 3 times 20 s, and 6X = 6 times 20 s). Baseline temperature is 4 ºC. 76

Table 5.1: Steps for the preparation of bacterial and viral strains, and their particular culturing conditions. 87

Table A.1: Loading ratios of the 3 NHs. 104

Table A.2: EDX elemental composition of the NHs synthesized. 104

Table A.3: Summary of XPS data and weight percentage of elements. 104

Table A.4: Temperature increase after 20 s MW irradiation time at 10% power (0.0006 kW·h). 105

Table A.5: ROS generating reactions[247]. 113

Table A.6: Calculated band edge energies of semiconductors at absolute vacuum scale (AVS) and normal hydrogen electrode (NHE). 116

Table A.7. Standard one-electron reduction potentials (E_H) of ROS at pH 7 with respect to NHE. 117

List of Figures

Figure 1.1: Research vision and plan of this dissertation showing interconnected spheres of knowledge. NH: nanohybrid, MW: microwave, WL: wavelength. 7

Figure 2.1: Representation of ANHs: (a) pH-responsive poly(acrylic acid) (PAA) at mesoporous silica nanoparticle (MSNPs)[82], (b) AgNPs in a thermo-responsive network of poly(styrene) (PS) and poly(N-isopropylacrylamide) (PNIPA)[83], and (c) photo-responsive Cu-doped ZnO NPs on multiwalled carbon nanotubes (MWNT)[84].....12

Figure 2.2: Number of publications per year on ANHs in the Web of Science® according to our search criteria.....15

Figure 2.3: (a) Distribution of ANH publications based on stimuli. *Include: ionic, chem, salt, electri, sound, redox, glucose, gluta, and enzyme as keywords. NR: not relevant. (b) Distribution of ANH publications on multi-stimuli. Other includes: pH-enzyme, pH-glucose, glucose-pH-thermo, photo-thermo-magnetic, and ultrasound-pH-magnetic multi-stimuli publications.....16

Figure 3.1: Representative HRTEM micrograph of (a) MWNT (> 95% carbon purity, 8-15 nm average diameter, and 10-50 μm length) and (b) NH-1 (inset shows crystalline erbium oxide lattices). (c) STEM image and elemental mapping of NH-1. Samples of aqueous dispersions for (a) and (b) were placed on lacey carbon coated copper TEM grids (SPI Supplies, West Chester, PA) and air-dried over a few minutes. HRTEM and STEM accelerating voltage set to 200 kV. Several representative micrographs were obtained. 45

Figure 3.2: (a) XPS spectra, (b) XPS region displaying typical Er4d multiplet structure, (c) XRD spectra of MWNT, erbium oxide, and NH-1, and (d) differential mass loss curve from TGA for the MWNT and NHs. Thin layers of dried samples were analyzed using a Kratos XPS equipped with a monochromated Al $K\alpha$ X-ray source (1.486 keV). XRD equiped with Cu-Kα irradiator (0.154 nm wavelength) and a graphite monochromator was used at a step width of 0.02° (between 2θ values of 20° and 60°) and a scanning rate of 2° min^{-1}. Dry samples (3-5 mg) were heated at 10 ºC min^{-1} ramp up to 800 ºC for TGA/DTG determination. 48

Figure 3.3: (a) Bacterial inactivation of *P. aeruginosa* exposed to NH-1, and appropriate controls; (b) comparison of logarithmic cell removal of *P. aeruginosa* exposed to NHs. Material concentration utilized in all experiments was maintained at 1 mg/L. Initial concentration of *P. aeruginosa* ~10^7 CFU/mL. Samples (200 µL) were irradiated in microtiter plates for 20 s at 110 W (611 mW·h) using a conventional MW oven. Error bars represent one standard deviation measured from experimental triplicates. NP: nanoparticle, MWNT: multiwalled nanotube, NH: nanohybrid.....49

Figure 3.4. (a) H_2O_2 production with and without MW irradiation by NH-1 and by the appropriate controls; (b) comparison of ROS production between the NHs. Material concentration utilized in all experiments was maintained at 1 mg/L. Samples (100 µL) were irradiated in microtiter plates for 20 s at 110 W (611 mW·h) using a conventional MW oven. LOD is 100 CFU/mL. Error bars represent one standard deviation measured from experimental triplicates.....53

Figure 3.5. Logarithmic cell reduction of *P. aeruginosa* exposed to NH-1 with and without H_2O_2, $O_2^{\bullet-}$, and $OH^{\bullet}$, scavengers CAT, SOD, and MET, respectively. Material concentration utilized in all experiments is maintained at 1 mg/L. Samples (200 µL) were irradiated in microtiter plates for 20 s at 110 W (611 mW·h) using a conventional MW oven. LOD is 100 CFU/mL. Error bars represent one standard deviation measured from triplicate samples. 54

Figure 3.6: Inactivation of *P. aeruginosa* exposed to NH-1, and appropriate controls; Bacterial cells were irradiated for 1X (20 s), 2X, 4X, and 8X duration. Temperature upon 8X irradiation increased no more than 20 °C. NH concentration utilized in all experiments was maintained at 1 mg/L. Samples (200 µL) were irradiated in microtiter plates at 110 W (611 mW·h) using a conventional MW oven. LOD is 100 CFU/mL. Error bars represent one standard deviation, measured from experimental triplicates. 56

Figure 3.7: Schematic representation of possible underlying mechanisms for ROS generation. (a) NHs suspended or attached to a relevant carrier in contact with water, (b) MW energy absorption by the NHs, (c) absorbed MW energy is transferred to neighboring nanocrystals resulting in charge separation and generation electron-hole pairs in the erbium oxide layer and MWNTs that will produce ROS, and (d) potential pathways of electron-hole pair formation and ROS generation. 58

Figure 4.1: Components of an EM wave. 63

Figure 4.2: Schematic representation of: (a) a uniform rectangular waveguide with driving and pickup stubs for waveguide design (slotted line) (b) cross section of the rectangular waveguide, and (c) example of detector standing wave pattern. 64

Figure 4.3: (a) Schematic representation of the MW setup, (b) MW power generator, (c) waveguide and copper reaction chamber, (d) closed end of the copper reaction chamber, (e) quartz vials and sample holders, and (f) sample preparation in sterilized quartz tubes. 70

Figure 4.4: Temperature change for samples as a function of MW power input and irradiation time for: (a) DI water samples in borosilicate and quartz vials, (b) DI water samples with and without 1 mg/L NH-1, (c) different volume of DI samples (at 30 W MW power), and (d) DI samples in a quartz vial with a range of input power. All experiments were conducted under 2450 MHz MW irradiation. 75

Figure 4.5: Log reduction of *P. aeruginosa* exposed to NH-1 when irradiated with (a) 2445 MHz, (b) 2450 MHz, and (c) 2455 MHz radiation for 1X = 20 s, 3X = 3 times 20 s, and 6X = 6 times 20 s at input power of 20 W, 40 W, and 60 W. Controls with no MW irradiation are presented in the inset figure. Irradiated controls were measured only for the highest irradiation condition (i.e., 6X irradiation time at 60 W). NH concentration utilized in all experiments is maintained at 1 mg/L. Initial concentration of *P. aeruginosa* ~10^7 CFU/mL. LOD is 100 CFU/mL. Error bars represent one standard deviation measured from triplicates. 77

Figure 5.1: Inactivation of *B. subtilis* exposed to NH-1, and appropriate controls. Material concentration utilized in all experiments was varied at 1 and 10 mg/L. Initial concentration of *B. subtilis* ~10^7 CFU/mL. LOD is 100 CFU/mL. Error bars represent one standard deviation measured from experimental triplicates.....90

Figure 5.2: Inactivation of *L. pneumophila* exposed to NH-1 and appropriate controls. 1 and 10 mg/L NH concentration was utilized up to three cycles of irradiation. Initial concentration of *L. pneumophila* ~2×10^4 CFU/mL. LOD is 100 CFU/mL. Error bars represent one standard deviation measured from experimental triplicates.....92

Figure 5.3: (a) Colonies of *F. columnare* grown in Anacker and Ordal agar and (b) inactivation of *F. columnare* exposed to NH-1. 1 and 10 mg/L NH concentration was utilized up to three cycles of irradiation. Initial concentration of *F. columnare* ~2×10^8 CFU/mL. LOD is 100 CFU/mL. Error bars represent one standard deviation measured from experimental triplicates.....94

Figure 5.4: Inactivation of MS2 bacteriophage exposed to NH-1 and appropriate controls. 1 and 10 mg/L NH concentration was utilized up to three cycles of irradiation. Initial concentration of MS2 ~6×10^8 PFU/mL. LOD is 50 PFU/mL. Error bars represent one standard deviation measured from experimental triplicates.....95

Figure A.1: STEM HAADF images of a representative ion-beam irradiated samples of NH-1. 106

Figure A.2: EDX spectrum of representative NH-1. Erbium, carbon, and oxygen elements are all identifiable. 107

Figure A.3: STEM images and elemental mapping of the NHs synthesized. 108

Figure A.4: TGA analyses of representative functionalized MWNT and NH samples. Temperatures of oxidation for the NHs are 475 ºC (NH-1), 474 ºC (NH-2), and 467 ºC (NH-3) respectively. 109

Figure A.5: Temperature differences between irradiated and microwave radiated samples. Differences are presented from room temperature (21 ºC).110

Figure A.6: Irradiation setup for the MW oven. (a) Top view of the microtiter plate positioned on the turntable. (b) Microtiter plate as the samples are ready to be irradiated in the MW cavity. (c) Sample location at the microtiter plate (top view). 111

List of Symbols and Abbreviations

$\boldsymbol{e^-}$	Electron
$\boldsymbol{f_{lc}}$	Lower cutoff frequency
$\boldsymbol{f_{uc}}$	Upper cutoff frequency
$\boldsymbol{h^+}$	Electron hole
$\boldsymbol{N_0}$	Number of viable microorganisms before treatment
$\boldsymbol{\varepsilon_r''}$	Dielectric loss factor
$\boldsymbol{\lambda_0}$	Free-space wavelength
$\boldsymbol{\lambda_g}$	Guide wavelength
$\boldsymbol{\lambda_{uc}}$	Upper cutoff wavelength
a	Broad-wall dimension of a waveguide
AgNP	Silver nanoparticle
ANH	Adaptive nanohybrid
ATCC	American Type Culture Collection
AuNP	Gold nanoparticle
b	Short-wall dimension of a waveguide
c	Speed of light
CAT	Catalase
CFU	Colony-forming unit
CNT	Carbon nanotube
DBP	Disinfection by-product
DI	Deionized water
EDX	Energy-dispersive X-ray spectroscopy
EHS	Environmental health and safety

EM	Electromagnetic
Er	Erbium
f	Frequency
GO	Graphene oxide
H_2O_2	Hydrogen peroxide
HRTEM	High-resolution transmission electron microscopy
IDA	Iminodiacetic acid
IEP	Isoelectric point
ISM	Industrial, scientific and medical
ISO	International Organization for Standardization
LB	Luria-Bertani liquid medium
LCST	Lower critical solution temperature
LOD	Limit of detection
MET	Methanol
MSNP	Mesoporous silica nanoparticle
MW	Microwave
MWNT	Multiwalled carbon nanotube
N	Number of viable microorganisms after treatment
NH	Nanohybrid
NM	Nanomaterial
NP	Nanoparticle
$O_2^{\bullet-}$	Superoxide
$OH^{\bullet}$	Hydroxyl radical
P2VP	Poly(2-vinylpyridine)
PAA	Poly(acrylic acid)

PBS	Phosphate buffer saline
PFU	Plaque-forming unit
PMEO2MA	poly(2-(2-methoxyethoxy)ethyl methacrylate)
PNIPA	Poly(N-isopropylacrylamide)
PS	Poly(styrene)
QD	Quantum dot
RF	Radiofrequency
ROS	Reactive oxygen species
SiNP	Silica nanoparticle
SOD	Superoxide dismutase
STEM	Scanning transmission electron microscopy
SWNT	Single-wall carbon nanotube
TGA	Thermogravimetric analysis
TiO_2	Titanium dioxide
UV	Ultraviolet
XPS	X-ray photoelectron spectroscopy
XRD	X-ray powder diffraction
ZnO	Zinc oxide
$\boldsymbol{\lambda}$	Wavelength

Chapter 1: Introduction

1.1 Introduction to the Study

The Schumpeterian trilogy of technological change, i.e., invention, innovation, and diffusion, highlights the importance and benefits of societal acceptance of any new technology[1]. Once a technology has diffused deep into the societal fabric, the spectrum of its application expands and allows for unintended uses, some of which might be transformative. One such example is mobile communication, which was not originally engineered to assist in healthcare, but now is utilized to disseminate medical information and has transformed this sector globally[2,3]. Microwave (MW) technology is affordable and similar in social adoptability and thus can be utilized to impact low-income communities across the globe, particularly to gain them access to safe drinking water. Although the position of MW radiation in the electromagnetic spectrum precludes its use in disinfecting water at a reasonable cost, finding a way to harness the power of MW radiation in an effective disinfection technology could potentially benefit a large global population.

Ensuring water safety via disinfection[4] has largely relied on the use of chemical oxidants since early 1900s[5]. Chemicals commonly used for this purpose include chlorine[6], chlorine dioxide[7], and ozone[8]. Ammonia added simultaneously or consecutively with chlorine forms another common disinfectant, chloramines, which is a less effective, but more persistent as compared to chlorine[6]. However, chemical disinfectants lead to the production of disinfection by-products (DBPs), which have raised public health concerns since the early 1970s[9]. Alternative non-chemical based disinfection technologies became

necessary, and ultraviolet (UV) irradiation has been developed as an effective disinfection alternative[10]. UV's germicidal effect is a result of the UV action on the nucleic acids of microorganisms and its efficacy depends on light intensity and exposure time[11]. Disadvantages of UV technology are the absence of disinfection residual beyond treatment facility[10,12], its need for a clear optical pathway to enable penetration of UV rays [13], and maintenance to prevent fouling of lamps[14]. Furthermore, UV technology is not commonly available at every household[15], but rather needs to be custom-made with the purpose of disinfecting water. Microwave-enabled inactivation technology can be a long-lasting, easy to use, and cost-effective alternative. The growth of the global microwave oven market in the near future[16] will enable to reap the unanticipated benefits of disinfection using this novel technology. Furthermore, such a technology can be used on a community basis where either access to electricity is limited or affordability of such a device is out of range at a household level.

Irradiation-based disinfection technologies are gaining popularity because of advances in equipment reliability and reduction of undesirable disinfection by-products[12]. The rapid growth of nanotechnology has prompted significant interest in environmental applications, and nano-scale materials are now being incorporated into such irradiation-based disinfection devices to improve reliability, reduce operating costs, and increase their disinfection efficiency[4,17]. Nanoparticles are used as photocatalysts to enhance and accelerate the inactivation rate of pathogenic microorganisms[17]. Light irradiated onto photocatalytic materials can effectively generate reactive oxygen species (ROS, see appendix C), one of the key modes of disinfection[4,18]. Of particular interest are combinations of materials and irradiation systems that use low-cost visible and/or UV

light to achieve high disinfection capacity. However, efficiency of any such technology depends on incident flux and wavelength of the radiation, specific water characteristics, absorption length in water, geometry and reactor hydrodynamics, contact efficiency of species in water and the photocatalysts, and inactivation kinetics[4].

A growing interest in enhancing low-energy electromagnetic radiation, e.g., visible and near infrared radiation, has successfully prompted new studies on production of ROS[19] as a part of the continuous effort to develop new alternative disinfection technologies. Such amplification of low energy photons to higher energy[20] has been successfully demonstrated using lanthanide series metals (e.g., Er^{3+} and Tm^{3+})[21,22]. Their unique $4f^n$ ($n = 0–14$) $5d^{0–1}$ inner shell configurations are well shielded by the outer filled $5s^25p^6$ sub-shell electrons and thus have an abundance of unique energy levels. When populated, these states can be long lived (up to 0.1 s), making these ideal to serve as electron donors[23]. This group of trivalent metals is also doped to engineer the band architecture and utilized in different applications[24]. To-date, successful utilization of low energy MW radiation for efficient generation of ROS and subsequent inactivation of waterborne pathogens has not been demonstrated. However, there is promise in carbon nanomaterials' ability to absorb MW energy[25] and lanthanide series metal's capacity to enhance spectral-conversion, if used in concert [23].

Developed during the Second World War, low-frequency MWs (at least 5 orders of magnitude lower than UV) have disseminated into industry and later into the household consumption market in a short period of time[26]. MWs lie between infrared radiation and radio frequencies and correspond to wavelengths of 10^{-3} to 1 m (300 GHz to

300 MHz frequencies, respectively)[27]. In this region, the energy of the MW photons (between 1.24×10^{-3} and 1.24×10^{-6} eV) is too weak to break chemical bonds[28], when compared to that of photons emitted by UV lamps with wavelengths ranging between 200 to 280 nm (6.20 to 4.43 eV). However, even this apparently weak MW radiation has proven to be germicidal when used at high intensity and for an extended period of time in sterilizing dry materials[29]. MW technology is effectively used to disinfect dentures and dental tools/devices[26], where 10 min of microwaving at 720 W is required for sterilization[30,31]. The antimicrobial impact of MW radiation is not well understood, but it is hypothesized to emanate mostly from thermal action[32] and also from dielectric rupture[33]. However, inactivating or disinfecting water with MW has not been successful to-date, likely due to an extended irradiation period and associated energy costs.

In this dissertation, the MW absorption-potential of carbon nanotubes (CNTs) has been combined with spectral conversion-ability of lanthanide series metal erbium oxides to attain effective inactivation of waterborne microorganisms. Such a carbonaceous-metal oxide nanohybrid (NH) has been synthesized and characterized, utilizing a modified sol-gel technique reported in a parallel dissertation work[34]. Design of the NHs for this dissertation was underway when the method was being modified. This dissertation synthesized the NHs varying the composition of the materials with the goal of harnessing the power of microwave, which is unique and independent when compared to the environmental implication aims pursued in the parallel dissertation. Inactivation of an opportunistic pathogen *P. aeruginosa* has been achieved using a conventional MW oven with the NHs, and later, using a controlled MW irradiation system that is designed and built as a part of this research effort. The dominant mechanism underlying inactivation

has been identified to be ROS-mediated inactivation. The roles of wavelength and irradiation time of MW on inactivation are also explored, and finally, the efficacy of this technology to effectively inactivate a wide range of waterborne microorganisms has been examined. Results obtained in this study show a proof-of-concept of a new irradiation-based water disinfection technology that can utilize low-energy intensive and widely available MW devices to inactivate waterborne microorganisms. This groundbreaking study paves the way for further development of such a technology that can effectively and affordably disinfect water.

1.2 OBJECTIVES AND HYPOTHESES

Below, the four primary objectives of this dissertation are stipulated. These objectives will be achieved by testing the corresponding hypotheses.

Objective 1. Perform a detailed literature review to better understand the multifunctional properties of NHs.

Objective 2. Design, synthesize, and characterize a novel NH, capable of MW spectral conversion for inactivation of *P. aeruginosa*.

Hypothesis 1: Sol-gel method can be utilized to synthesize CNT-lanthanide series metal oxide NHs with different carbon to erbium ratios and achieve control over the hybridization process.

Hypothesis 2: NHs capable of MW absorption and spectral conversion will effectively inactivate *P. aeruginosa*.

Objective 3. Exploring the roles of MW wavelength and irradiation time on inactivation effectiveness of *P. aeruginosa* in an effort to unlock the energetic balance in the disinfection system.

Hypothesis 3: Wavelength and irradiation time of MWs will strongly influence inactivation of *P. aeruginosa*.

Objective 4. Determine the inactivation efficacy of the MW spectral conversion NHs for a wide range of waterborne microorganisms.

Hypothesis 4: The NHs will be capable of MW spectral conversion and thus inactivate a wide range of waterborne microorganisms.

1.3 RESEARCH VISION AND PLAN

The research described in this dissertation presents a nascent and novel irradiation-based water disinfection technology for the first time. At the core of my research agenda lies the idea of deepening the knowledge on MW-enabled inactivation technology as well as to develop a novel material to effectively inactivate pathogens. To achieve these goals, the following tasks were performed (Figure 1.1).

Task 1: Literature review on multifunctional NHs.

***Task 2.1*:** Design, synthesis, and characterization of a novel NH, capable of MW spectral conversion.

Task 2.2: Assessment of inactivation potency of the NH and exploration of underlying inactivation mechanism(s).

Task 3: Exploration of the roles of wavelength and irradiation time of MWs on inactivation potency of *P. aeruginosa*.

Task 4: Evaluation of inactivation efficacy for a wide range of waterborne microorganisms.

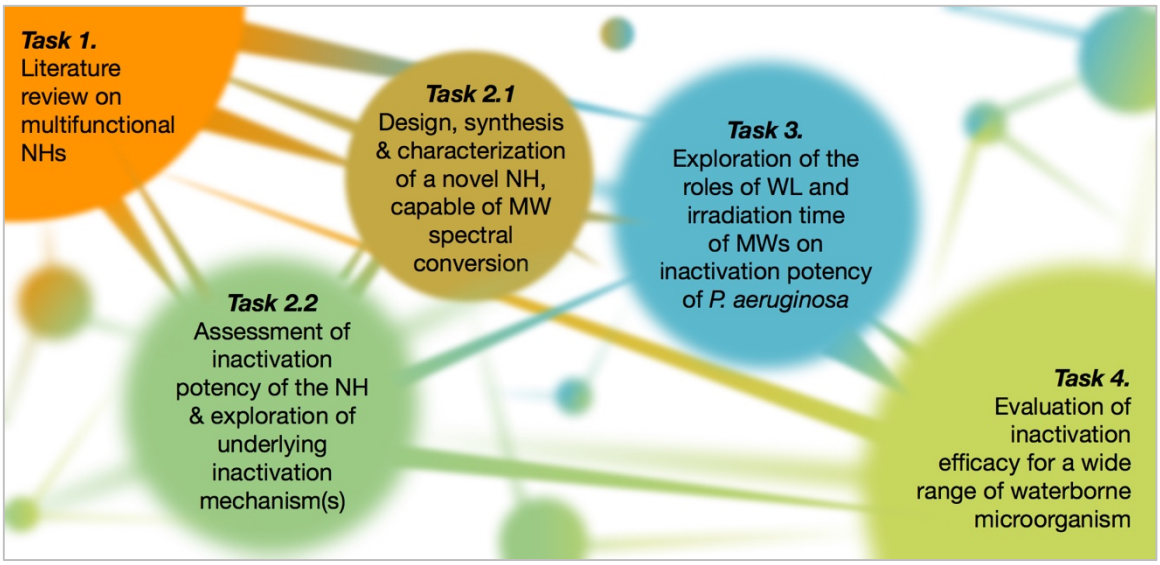

Figure 1.1: Research vision and plan of this dissertation showing interconnected spheres of knowledge. NH: nanohybrid, MW: microwave, WL: wavelength.

1.4 Dissertation Structure

This dissertation is organized into chapters containing the following information:

Chapter 2: Multifunctional Properties of NHs

Contains a detailed overview on multifunctional properties of NHs, stimuli-responsive nanomaterials, and CNT responses to MW radiation.

Chapter 3: Harnessing the Power of Microwave for Inactivation with Nanohybrids

Presents preliminary results of design, synthesis, and characterization of the novel NHs that can harness the energy of MW to inactivate *P. aeruginosa*. This is the first study of its kind presenting groundbreaking results of this emerging technology.

Chapter 4: Exploration of the Roles of Wavelength and Irradiation time of MW on Inactivation Potency of *P. aeruginosa*

Presents the first preliminary results on the design, optimization, and performance of a controlled MW irradiation system implemented at lab scale for testing waterborne pathogen inactivation with NHs.

Chapter 5: Evaluation of Inactivation Efficacy for a Wide Range of Waterborne Microorganisms

Assesses the efficacy of the designed NHs (in Chapter 3) using the reactor developed (in Chapter 4), to evaluate its "breadth" of application to inactivate surrogates for pathogenic bacteria, viruses, and protozoa of environmental relevance.

Chapter 6: Conclusions and Recommendations

Outlines major findings pertaining to the main objectives of this work and provides recommendations for future studies to advance this technology.

Chapter 2: Multifunctional Properties of NHs[i]

2.1 INTRODUCTION

This chapter intends to provide a detailed literature review to better understanding the multifunctional properties of NHs. After an extensive literature review performed on multifunctional NHs[35-37], design of a NH capable of MW absorption and spectral conversion, and thus suitable for effective inactivation of waterborne pathogens was attempted. This vast literature made it possible to better understand the synergistic aspect of multicomponent materials to gain an understanding of the state of the NH materials field. Consequently, I led a peer-reviewed article on stimuli-responsive NH[38] and gathered critical knowledge to pursue design of a multi-component NH that responds to electromagnetic radiation and will likely generate ROS, a key driver in bacterial inactivation. This review was particularly focused on stimuli-responsive materials, which activate under an external chemical or physical stimulus.

This chapter is based and adopted from the peer-reviewed article on stimuli-responsive NHs[38] and complemented with a section on carbon nanotube (CNT) responses to MW radiation.

2.2 LITERATURE REVIEW

During the past decade, material science at the nano-scale has witnessed the emergence of a new wave of research and development that has shifted from single

[i] Adopted from: **Plazas-Tuttle, J.**; Rowles, L., III; Chen, H.; Bisesi, J., Jr; Sabo-Attwood, T.; Saleh, N. B. **(2015).** Dynamism of Stimuli-Responsive Nanohybrids: Environmental Implications. *Nanomaterials*, *5* (2), 1102–1123. doi:10.3390/nano5021102. Plazas-Tuttle, J, is the main author, wrote the article, draw the figures, and performed 90% of the literature review and data collection.

passive nanostructures to complex hierarchical nanosystems[39]. Such hierarchical structures are designed via hybridization of multiple nano-scale entities or by conjugation of a nanomaterial with heterocyclic organic coatings. These nanohybrids (NHs) exhibit enhancement in their individual component properties[35] and are driving the frontier of material science development with applications in biomedicine[40,41], electronics[42,43], optical imaging[44,45], water quality management[46,47], controlled drug delivery[48,49], biomedical systems and devices[50-52], and energy related applications[53-55]. Such applications demand multifunctionality, necessitating design and development of adaptive and responsive materials where manifestation of material properties evolves in a more predictable and controllable fashion in response to the surrounding environment or stimuli. Hybridized or conjugated nanostructures are suspected to present complexity in nano-EHS[35-37]. Dynamism of the adaptive nanohybrids (ANHs) will likely introduce an additional degree of uncertainty and complexity to nano-EHS, i.e., dynamic time-dependent evolution of the soft coating.

The necessity to achieve 'on demand' control over material functionality and the ability to functionalize nanomaterials with unique combinations of organic polymer blocks have encouraged design and synthesis of stimuli-responsive nanoparticles[56] or ANHs. Today's drugs are not only required to optimize targeted delivery but are also designed to manifest superior control over their release[57]. Complex combination of multiple soft organic blocks allows for achieving such molecular level control in response to an environmental stimulus—e.g., pH[49], ionic strength[58], solvent polarity[59], heat[60], magnetic[61] or electric field[62], light[63], and sound[64]—and enable their applications in targeted drug delivery, development of artificial muscles and sensing materials, robotics,

and molecular electronics[65,66]. Next generation molecular electronics and bio-engineered applications are more encouraged to employ such stimuli-responsive ANHs and thus necessitate careful assessment of their potential environmental and toxicological consequences.

Stimuli-responsive ANHs are composed of well-studied nanostructures, e.g., carbonaceous[47,67] and metallic[53,62,68], as well as polymeric[69-71] materials, however, with a complex soft-layer at the exterior. EHS studies on nano-scale metal or metal oxide particles as well as on carbonaceous nanomaterials have been aimed at correlating EHS responses of nanomaterials (NMs) with their properties such as size, shape, surface chemistry, electronic structure and surface charge[72-77]. The role of NM surface functionality, i.e., of both covalent surface moieties and of soft polymeric/surfactant coatings, on aggregation, deposition, transformation, and toxicity has also been evaluated[76,78-81]. However, the coatings considered were rather passive in a given environment. Complexity and uncertainty in EHS of ANHs will likely arise from the dynamic nature of the surface coatings, as their surface conformation and participation in potential ligand exchange will evolve over time in presenting their chemical functionalities to the surrounding environment and biological species, while responding to the external stimuli. If a soft surface coating is composed of multiple functional blocks where one or more of these blocks respond to an external stimulus (e.g., exfoliate or compress in response to the stimuli), the aggregation/deposition (where steric interaction will dynamically change) and toxicity (cells or species interacting with the exposed block will evolve dynamically) assessment will need to account for such dynamism to accurately assess their EHS.

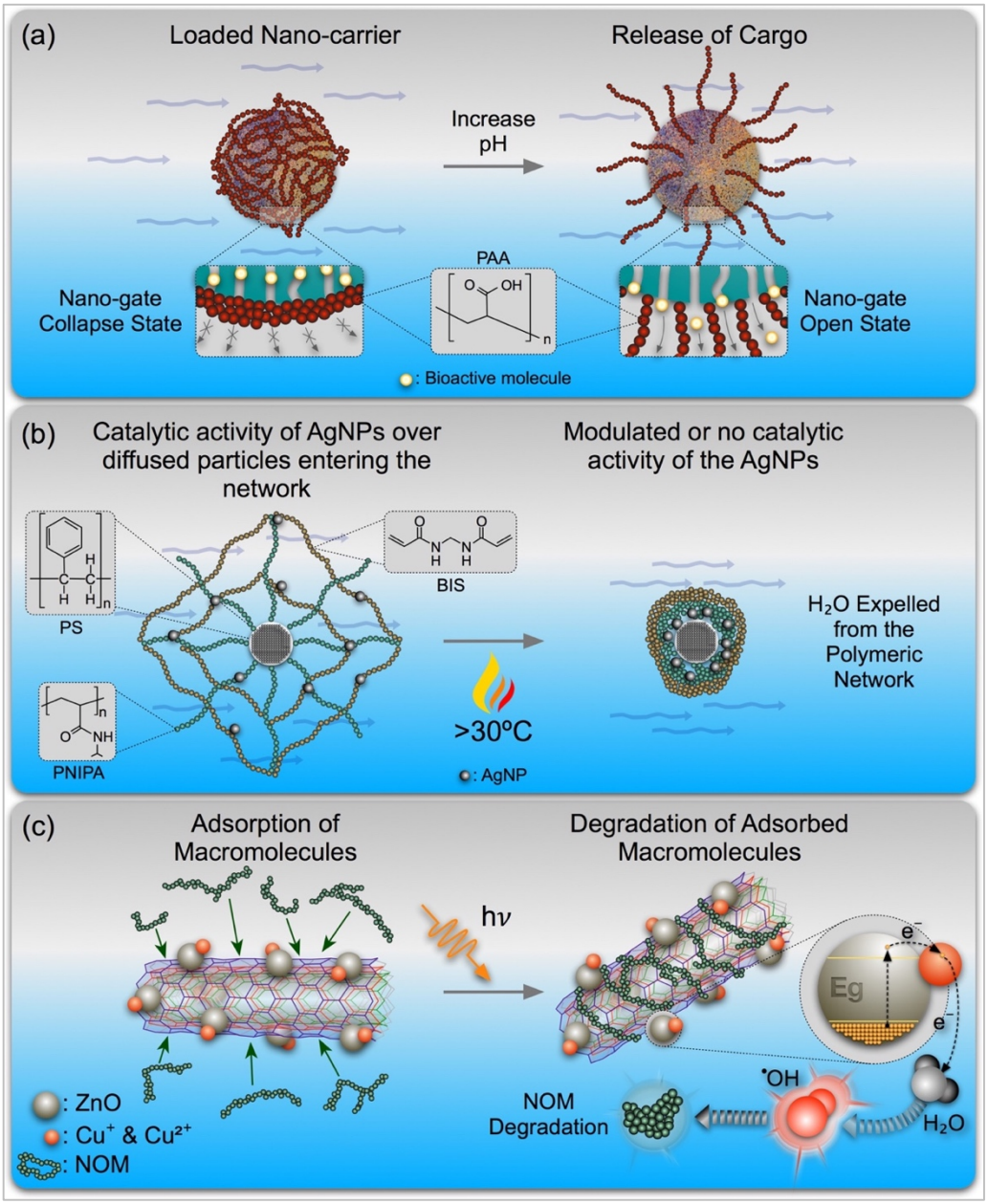

Figure 2.1: Representation of ANHs: (a) pH-responsive poly(acrylic acid) (PAA) at mesoporous silica nanoparticle (MSNPs)[82], (b) AgNPs in a thermo-responsive network of poly(styrene) (PS) and poly(N-isopropylacrylamide) (PNIPA)[83], and (c) photo-responsive Cu-doped ZnO NPs on multiwalled carbon nanotubes (MWNT)[84].

2.3 PRINCIPLE FOR DISCERNING ANHS

Since ANHs involve surface coated metallic, carbonaceous, or polymeric NMs, discerning the differences between passive and adaptive nano structures is important in directing EHS efforts appropriately. Here is the first attempt to lay down the principle for identifying ANHs. This principle is derived from earlier NH foundational work[36].

"Conjugated nano structures composed of carbonaceous, metallic, or polymeric materials when coated with a soft chemically bound exterior polymeric layer, resulting in core-shell type hybrids that respond to external stimuli that has enhanced properties or multifunctionality, can be identified as adaptive nanohybrids or ANHs." This principle includes ANHs composed of metallic, carbonaceous, or polymeric NMs and NHs functionalized with stimuli-responsive coronas or polymers[85-88] (Figure 2.1a), and NMs suspended or loaded with linear and branched stimuli-responsive co-polymers or cross-linked polymer networks[70,83,89] (Figure 2.1b). ANHs in which stimuli-responsive coatings are covalently bonded to drug molecules[90] or to metallic NMs with tunable properties[60] (Figure 2.1c), and polymer brushes grafted[91] or strongly bonded via sulfur bonds[85], can also be included.

This principle would exclude selection of the following as ANHs; (i) NMs and NHs with coatings that are not stimuli responsive (e.g., NHs comprised of dihydroxotin (IV) porphyrin functionalized single-walled carbon nanotubes (SWNTs)[44], NHs composed of quantum dots (QDs) and Cytochrome P450[42], and NHs containing carbon nanotubes (CNTs) and CdSe QDs [45]), (ii) that are not covalently bound (e.g., QDs coated with thermo-responsive[92] or pH-responsive polymers[93] by simple ligand exchange

methods), and (iii) those that will detach from the NM surfaces upon environmental contact (e.g., NHs of PS core and a multi-armed pH-responsive weak polyampholytic poly(2-vinylpyridine)-b-poly(acrylic acid) diblock copolymer[94], or MSNPs capped with poly(propylene imine) dendrimers through reducible disulfide bonds that enable detachment upon stimulus[95]). This principle will facilitate identification of ANHs for nano-EHS evaluation. However, further modification or amendment of the stated principles will likely be required as advances are made in the research and development of similar new materials.

2.4 CLASSIFICATION OF ANHS

The behavior of ANHs is controlled by the external stimulus that can cause the exterior coatings to shrink/swell, change optical, mechanical, or luminescence response of the nanostructure, to name a few. Although the field of ANHs is relatively new, there are numerous opportunities to design new nanosystems with single- or multi-stimuli-responsive attributes. The following discussion classifies ANHs on the basis of stimuli that invoke responses from the particles. A comprehensive literature search has been performed to identify relevant ANHs. A total of 812 publications from 1996-2014 were retrieved and classified using the Web of Science® search engine. After a list of relevant terms was identified, a search algorithm was designed using wildcards and Boolean operators, in combination with title field tag as the search criteria to limit the results to the most relevant studies in ANHs. Figure 2.2 shows the rapid growth rate of this ANH field as reflected by the near exponential increase in publication number over the past ten years.

Follow-up searches were performed for each individual stimulus of concern, i.e., for pH-, photo-, thermo-, ion-, chemical-, salt-, magneto-, acoustic-, redox-, glucose-, glutathione-, enzyme-, thiol-, radiation-, and multi-stimuli responsive materials. Results reveal the relative importance of each of the stimulus in the contemporary ANH literature. The distribution of ANH publications based on the most relevant stimuli is shown in Figure 2.3a, which identifies that pH, temperature, and photo-responses as the most prominent stimuli in ANH design and development.

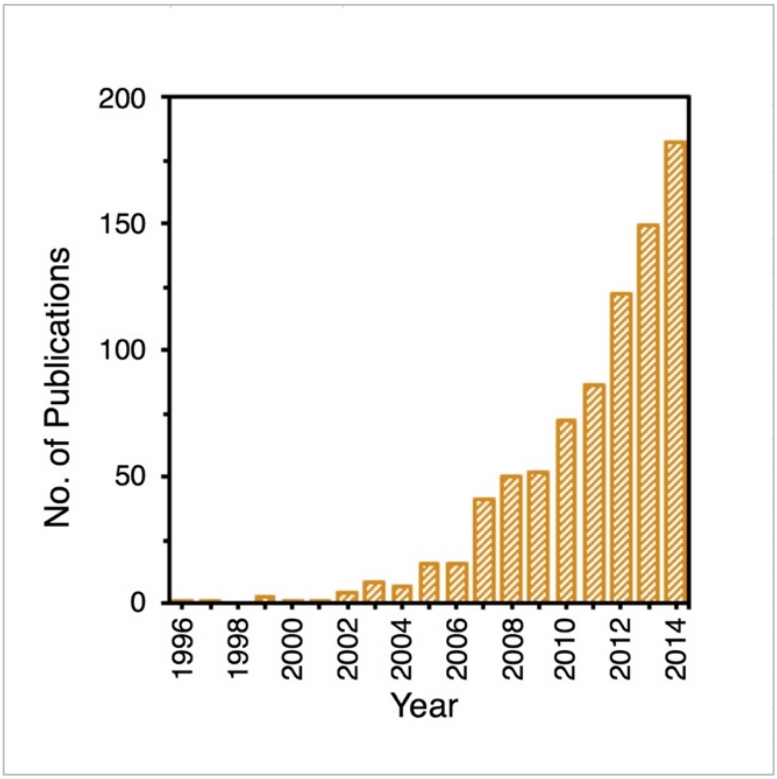

Figure 2.2: Number of publications per year on ANHs in the Web of Science® according to our search criteria[ii].

[ii] (Ti=[nanomaterial* or nano-material* or nanoparticle* or nano-particle* or nanostructure* or nano-structure* or nanohybrid* or nano-hybrid*] and Ti=[stimul*-respons* or *responsive or stimul*] and

Stimuli-responsive soft-layers enable ANHs to perform switchable functions and show considerable changes in their physical and chemical properties in response to small changes in their environment. The classification of ANHs can be done in a number of ways. Here we present a classification scheme based on key environmental stimuli, namely pH-, thermo-, photo-, and multi-stimuli-responsive ANHs.

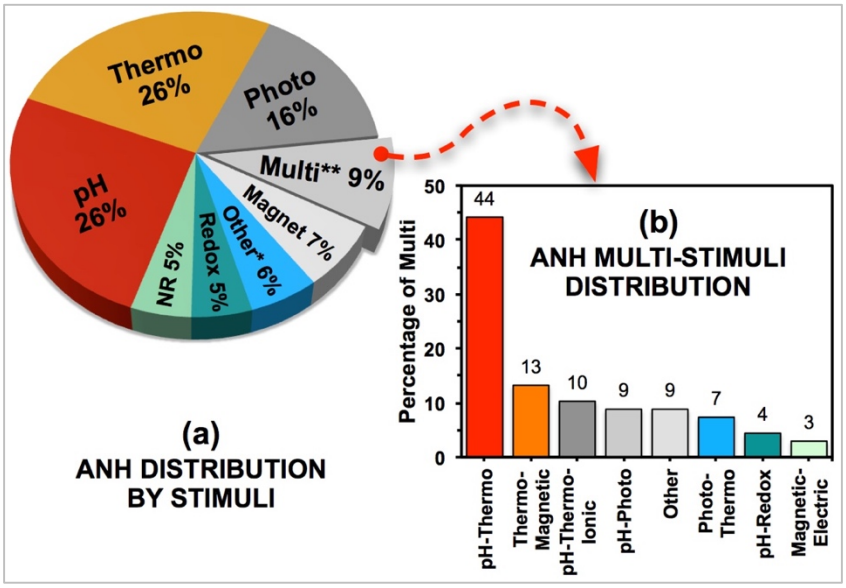

Figure 2.3: (a) Distribution of ANH publications based on stimuli. *Include: ionic, chem, salt, electri, sound, redox, glucose, gluta, and enzyme as keywords. NR: not relevant. (b) Distribution of ANH publications on multi-stimuli. Other includes: pH-enzyme, pH-glucose, glucose-pH-thermo, photo-thermo-magnetic, and ultrasound-pH-magnetic multi-stimuli publications.

Ti=[pH or light* or photo* or thermo* or temperature* or heat or ion* or chem* or salt* or *magnet* or *electri* or *sound or acoustic or *sonic* or redox* or glucose* or gluta* or enzym* or thiol* or radiat* or multi*])

2.4.1 pH-Responsive

One of the most common stimuli is pH, where functional moieties on ANH surfaces respond to specific pH range and perform desired functions. pH-responsive moieties are mostly acidic that include carboxylic, amino acid, or sulfonic acid groups. Depending on the pH, these polymers undergo a transition between protonation/deprotonation, relative to their pKa or pKb (equilibrium acidity or basicity constants). Weak acids are water-soluble via deprotonation while weak bases become less soluble at these pHs as protonation reduces surface potential and hence their relative polarity. Thus, in an aqueous environment, the ionization leads most commonly to swelling or shrinking of the polymeric shell of ANHs. For instance, at low pH, carboxylic functional groups are protonated and hydrophobic interactions dominate, leading to volume shrinkage of the polymer that contains them. On the other hand, at high pH, carboxylic groups dissociate resulting in a high charge density in the polymer, resulting in swelling of the polymer. Another common pH-responsive functional group is pyridine, which responds in the opposite way to the carboxylic group with the changes in pH values[96].

Representative polymers with pH-dependent conformational changes via protonation/deprotonation include PAA[82], poly(methacrylic acid)[97], poly(maleic anhydride)[98], poly(2-dimethylaminoethyl methacrylate) (PMAEMA)[99], and poly(4-vinylpyridine) (P4VP)[100], to name a few. But polymers containing phenylboronic acid[87] and phosphoric acid derivatives[101] have also been reported to form ANHs. Poly(amidoamine) is a biologically-responsive polymer that has also been observed to undergo conformational changes from a relatively coiled (hydrophobic) to a rather open

(hydrophilic) structure, when exposed from a neutral to an acidic environment with many interesting properties in applications in intracellular drug delivery[102].

pH-responsive ANHs are used as drug delivery carriers, imaging agents, sensors in biomedical purposes, with potential applications in other fields such as water-repellent inexpensive agents to coat glass surfaces, polymeric nanofibers, and paper surfaces as a function of the pH of interest. An example of a pH-responsive ANH capable of delivering both therapeutic cargo molecules and bio-relevant metal ions is a nano-gate composed of two iminodiacetic acid (IDA) molecules and a metal ion latch, assembled on MSNPs. This ANH forms a gating mechanism and is capable of storing and releasing metal ions and molecules trapped in the pores. Pore openings derivatized with IDA can be latched shut by forming a bis-IDA chelate complex with a metal ion. No cargo release is observed in a neutral aqueous environment; however, when the environment is acidic, ($pH \leq 5.0$) and/or when a competitive binding ligand is introduced, the cargo release is observed[103]. Similarly, MSNP cores with PAA shell can serve as nano-carriers for loading molecules for a wide range of biomedical applications[82]. The PAA layers on the surface of MSNPs could be reversibly opened and closed, triggered by pH, and thus could regulate the uptake and release of drugs from MSNPs. At low pH ($pH = 1.2$) PAA is insoluble and is collapsed, whereas, at high pH ($pH = 8.0$) PAA is soluble and rather exfoliated to allow for the bioactive molecules contained in the MSNPs to be released[82].

By altering the polymer shell structure, the ANH responsiveness to the stimulus can also be controlled. For example, a silica oxide core when modified with poly(2-vinylpyridine) (P2VP) shell, and decorated with AuNPs, can be used as free-standing

single-particle sensors in various miniaturized analytical systems. The P2VP polymer brush of the ANH undergoes reversible swelling/shrinking as pH changes from 2.5 to 5.7. Such dynamic change in the polymer brush conformation alters the access of the surrounding fluid to the metallic AuNP surfaces and Plasmon resonance behavior is also modulated by a purple-blue shift (from red)[91]. An inexpensive system for water repellent applications can be achieved using poly(2-(diisopropylamino)ethyl methacrylate) or PDP hybridized silica nanoparticles (SiNPs) with low pKa (6.3) and high hydrophobicity (pH ≥ pKa). Adsorption/desorption of PDP-SiNPs onto/from the proposed substrates can be controlled by varying solution pH resulting in the protonation/deprotonation of the PDP in a simple and effective way[104].

2.4.2 Thermo-Responsive

Due to the simplicity of control, temperature is one of the most widely used external stimulus in ANHs design. Temperature can trigger response from ANHs coated with thermo-responsive polymers that contain hydrophobic (e.g., methyl, ethyl, and propyl) moieties. The properties of thermo-responsive polymers are governed by the lower critical solution temperature (LCST), defined as the temperature at which the polymer undergoes a phase transition from a soluble to an insoluble state[71,96]. In general, the solubility of most of the polymers increases with the increase in temperature; however, in the case of polymers that exhibit LCST, increase in temperature decreases the water solubility due to hydrophobic associations of polymer molecules and reduction in hydrogen bonding between polymer and water molecules[105].

Temperature-responsive polymers can be classified depending on the mechanism and chemistry of the polymer groups: (a) poly(N-alkyl substituted acrylamides), e.g., PNIPA with an LCST of 34.5-35 ºC[106,107], and (b) poly (N-vinylalkylamides), e.g., poly(N-vinylcaprolactam), with an LCST of about 31–38 ºC, depending on the molecular weight and concentration of the polymer[108,109]. PNIPA has been widely studied for its ability to switch surface wettability, that consists of fluctuations in the competition between intermolecular and intramolecular hydrogen bonding below and above the LCST, hydrophilicity, and hydrophobicity, respectively[110].

For instance, the optical and light scattering properties of AuNPs are known to be altered by the conformational and chemical changes of their thermo-responsive polymer shells, and this property is exploited in the design of ANHs. AuNPs can be functionalized with cross-linked poly(2-(2-methoxyethoxy)ethyl methacrylate), PMEO2MA. The thermo-responsive coating undergoes a phase transition from a hydrophilic water-swollen state to a hydrophobic globular state, when heated above its LCST. Such changes result in modification of the light scattering properties of the nano-system and cause a change in the turbidity of the gel network of PMEO2MA[60]. Different degrees of swelling at high and low temperatures influence the range of applications of core-shell ANHs. AuNPs encapsulated in a thermo-responsive microgel (e.g., PNIPA) are used as catalysts in the electron-transfer reaction between hexacyanoferrate(III) and borohydride ions. The thermo-sensitive PNIPA network acts as a "nano-gate" that can be opened or closed to a certain extent, thereby controlling the diffusion of reactants toward the catalytic core; such is the control of the catalytic activity of the encapsulated AuNPs via temperature modulation[111]. Similarly, AgNPs, when embedded in a thermo-responsive polymeric

network of PNIPA cross-linked with N,N'-methylenebisacrylamide, can dictate the dissolution properties of the ANHs[83]. Metallic NPs are fully accessible to reactants at low temperature (as the polymer is exfoliated). However, at higher temperatures the rate of reactions is considerably slower due to the shrinkage of thermo-responsive polymer network[83].

2.4.3 Photo-Responsive

Light stimulation and response is a particularly useful external trigger to efficiently manipulate ANH responses. A number of parameters (light intensity, time of exposure, and wavelength) can be tuned for a specific target, which allows to designing a wide selection of stimuli-responsive ANHs. Photo-responsive, particularly, photo-cleavable polymers e.g., PNIPA-o-nitrobenzyl alcohol-poly(4-substituted-3-caprolactone)[112], poly(methyl methacrylate)-poly[poly(ethylene glycol) methyl ether methacrylate][113], and P4VP-poly(methylmethacrylate)[114] have received attention in recent years, since they can be degraded into smaller molecular fragments by irradiation. These photo-responsive polymers are used for synthesis of ANHs and applied as nano-carriers for drug delivery[112] and as photodynamic therapeutic agents[115].

Photoisomerizable molecules such as azobenzenes have been incorporated to macromolecules to produce macroscopic changes in the polymeric material. Azobenzene, is a well-known photo-responsive molecule that has been widely used in a diverse set of optical devices and to achieve multifunctionality; e.g., photo-switching[116], photo-optical image recording[117], and molecular detection[118]. The azobenzene moieties can undergo reversible photo-isomerization between the stretched trans (E-isomer) and the bent cis (Z-

isomer), when exposed to light at a certain wavelength (alternating irradiation at visible (465 nm) and UV (350 nm) range) or heating, and can lead to considerable changes in molecular shape, size, and dipole moments[116]. Thus, the azobenzene photo-responsive group allow for photo-controllable self-assembly of block copolymers and other photo-responses of lower molecular weight molecules. For instance, controlling the interparticular space between particles by reversibly bringing out the trans-cis-trans isomerization of photo-responsive molecules containing an azobenzene moiety incorporated into networks of benzyldimethyl- stearylammoniumchloride and octadecylamine capped AuNPs, results in changes from red to blue in the optical spectra of the surface Plasmon peak position of the NH network[119]. Similarly, NMs coated with polyaniline (PANI), a conducting polymer possessing interesting electronic, electrochemical, and optical properties, can be prepared by incorporating the photosensitive coumarin moieties into 2-acrylamido-2-methyl-1-propanesulfonic acid copolymer micelle. The resulting ANH exhibits reversible photo-cross-linking and photo-decrosslinking behavior upon irradiation with UV[120].

Other examples include bipyramidal DNA nanocapsules based on photo-responsive oligonucleotides that release AuNPs when photo-irradiated, via strand displacement mechanism[121]. Such release is guided by reversible cage–opening that depends on the wavelength of the photo-irradiation (i.e., from visible to UV). Aminopropyl-silsesquioxane (POSS-NH2) has been employed to functionalize graphene oxide (GO) sheets. The combination of the GO sheets with POSS-NH2 produces a hybrid silicon/graphite-based NP, which when exposed to visible light exhibits dielectric or insulating behavior, rendering photoconductive response[122].

2.4.4 Multi-, Bio-, and Other-stimuli Responsive Nano-Systems

Many ANHs are designed with polymer blocks that respond to more than one stimulus or are only responsive to biological stimuli (Figures 2.3a and 2.3b). pH and redox are two of the strongest stimulus in such multi-stimuli platforms that are designed for cancer treatment[123]. Other examples of a multi-stimuli ANH platform include a multilayer film (layer-by-layer) formed around PEGylated NPs (i.e., thiolated synthesized via self-condensation of 3-mercaptopropyltrimethoxysilane) and light-sensitive azobenzenes that respond to pH, light, and ionic strength, simultaneously[124]. Such ANHs have the potential applications as multi-responsive nano-carrier for drug delivery or as drug-releasing films. Similarly, switchable drug-release nano-platforms utilizing degradable poly(ether urethane) generates ANHs that respond to changes in temperature, pH, and redox potential[125]. A triple-stimuli of temperature, pH, and magnetism can trigger responses from poly(N-isopropylacrylamide-co-methacrylic acid) coated magnetic SiNPs[126]. Similarly, responsive polycarbonate membranes have been prepared with the combination of multi-responsive PNIPA and AuNPs to create responsive valves for the spatiotemporal delivery of bioactive agents, cell array, and advanced cell culture. The synthesized membranes showed, experimentally, a switch in response to temperature and light and achieved differences in fluid flow[127].

ANHs that are designed to respond to other stimuli include those that respond to biological molecules such as glucose[128], where insulin is released via poly(vinyl alcohol) and poly(N-vinyl-2-pyrrolidone) with pendent phenylboronic acid moieties and applied for diabetes treatment. Similarly, glutathione[129] is used as a cancer therapy agent, where

hollow SiNPs carriers of doxorubicin respond to stimulus for release of treatment agents. Biocatalytic enzymes also are employed for diagnostics, drug targeting, and drug release, where proteases are employed as cleavers[130]. ANHs that respond to biochemical stimuli are of great importance if released to the environment; however, the literature is not as elaborate.

2.5 EHS IMPLICATIONS

Environmental implications of passive nanostructures have been extensively studied, where the role of size [96], shape[131], surface functionality[132], surface coatings[133], and atomic orientation[134] have systematically been assessed. System complexity, i.e., chemical variability (pH, ionic strength, bio-fluid conditions)[135], presence of geo- and bio-macromolecules[76], heterogeneity of environmental collectors, i.e., sand and sediment[136], even presence of secondary particulates[137] have been evaluated to understand NM fate, transport, transformation, and toxicity under rather realistic environmental conditions. The key underlying overtone of such studies was that NMs were considered to be passive with respect to the surrounding environment—other than apparent charge neutralization through ionic strength effects—where the NM surface attributes were not designed to evolve over time and specifically respond to changing environments. The inception of ANHs has primarily been guided by targeted delivery of nano-scale agents where NMs were deliberately given exterior functionality (in form of surface coatings) with abilities to respond to a specific environment and dynamically evolve in response to select stimuli. Release of these ANHs to the natural environment will expose them to a variable and rather complex environment, where co-existence of multiple stimuli and

change in stimuli composition can create unforeseen environmental and toxicological behavior; hence necessitate additional considerations to assessing nano-EHS.

When NMs are released in the natural environment they undergo aggregation, primarily by the interplay of the inherent van der Waal's attractive forces and surface charge mediated electrostatic repulsive forces[138]. Aggregation can lead to 'fall out' of the NMs from the water column to the sediment and enhance the removal of these particles within the pore space by increased deposition[139] and limit organism size-selective uptake[140]. Furthermore, passive NMs undergo natural modifications and/or chemical transformations due to interactions with various environmental components such as sunlight, dissolved oxygen, ionic strength, and dissolved organic matter[35]. Since environmental systems are dynamic and unpredictable, the physicochemical changes experienced by NMs complicate the understanding of risks associated with environmental release of NMs. NMs that might show high aggregation or deposition propensity and manifest toxic responses at the laboratory-scale, are not necessarily prone to such behavior demonstration when discharged to real aquatic environments. When such uncertainty exists in the case of passive NMs, ANHs with increased dynamism on their surfaces introduce an additional degree of complexity to the EHS assessment. For instance, fullerene suspensions are destabilized in relatively weak electrolyte solutions driven by electrostatics, resulting in aggregation and filtration in environmental systems. The propensity of fullerenes to aggregate in relatively weak electrolyte solutions suggests that, if released into natural systems, typically with ionic strengths greater than 0.001 M, these materials will likely form large aggregates that may settle out of suspension, deposit to environmental collectors, or become otherwise immobilized[141]. These phenomena may

partially offset any risk presented by possible fullerene toxicity due to a reduced potential for exposure. However, other components present in natural waters, such as humic or fulvic acids may re-mobilize fullerenes and change their aggregate size, while transformation (photo or chemical) may continue to alter their potential health effects compared with those observed in laboratory-based toxicity studies[142].

The following section will discuss the role of select environmental stimuli (pH, temperature and photo-activity) in influencing the behavior and toxicity of emerging ANHs, with a focus on the aquatic environment. We will consider what we have learned from studying passive NMs in predicting how the environment should be considered with respect to ANH behavior and toxicity.

The role of pH in nano-EHS has traditionally centered around the concept of protonation/deprotonation of surface moieties, which control the surface charge and thus the stability, transport, and in some cases toxicity of the NMs. High salt concentrations and pHs close to isoelectric point (IEP) promote NM aggregation by compressing electrical double layer repulsion[73]. IEP has served as a threshold for charge-reversal, which has depended primarily on acidity/basicity of the surface groups. However, pH in any such analyses is an environmental parameter and in equilibrium with the entire particle surface (not partial) at all times, mediating particle behavior over a wide range. In the cases of pH-responsive ANHs, the polymeric coatings respond differently to pH, based on the chemistry of the polymer block. For example, PAA contains carboxylic groups that can deprotonate at high pH ($pH \geq 8$) increasing its solubility, but protonate at low pH ($pH \leq 4.0$) making it poorly soluble; i.e., it collapses onto a surface to avoid

interaction with the surrounding polar medium in such conditions[82]. On the other hand, pyridine is an acid-swellable group. Under acidic environment the pyridine groups are protonated giving rise to internal charge repulsions between neighboring protonated pyridine moieties[143].

pH-responsive ANHs that combine PAA and pyridine soft layers and other NMs have great potential for application in drug delivery systems. Thus in natural environments, the relative collapse or exfoliation of surface coatings on ANH surfaces will present with variable aggregation and deposition (each polymer/polymer block has differing electrostatic and steric stabilization contribution), transformation (differential dissolution based on the polymer conformation), and toxicity (non-uniform cell-ANH interaction, based on polymer conformational differences). Studies performed to-date have shown that coatings like PAA influence NM solubility as a function of the ambient pH. For example, metal NPs coated with PAA are typically less soluble but show enhanced ion release under acidic conditions[144] and such a low pH environment has been suggested to adversely affect fish growth and development (e.g., inhibition to hatching)[145]. Unique properties of ANHs, such as the ability to 'swell', would likely impact organism uptake and bio-distribution and will also depend on the environment that will influence such 'swelling' (i.e., water column versus gastrointestinal (GI) tract versus lysosomes). For example, in the acidic stomach environment, single AgNPs can agglomerate and precipitate, while deposition of NHs composed of AgNPs and silicate clay, in the same acidic environment is minimized[146]. Design of pH-responsive ANHs for drug delivery, such as Doxorubicin, has been shown to be successful in targeting and delivery to tumors in case of a more acidic environment (6.0 – 6.5)[147,148]. This brings up a

number of issues relevant to assessing toxicology where such ANHs are released into environments with dynamic pH ranges and could lead to a number of diverse and unpredictable scenarios. For example, ANHs in a more basic/neutral environment can carry cargo into exposed organisms where they are then released in acidic GI tracts or lysosomes or perhaps release of the cargo in an acidic environment could allow for rapid uptake of the free cargo.

It is known that pH affects hydrodynamic radii of NPs and that select size ranges are associated with observed toxic effects such as lethality, reduced growth, and reproduction rates[149-151]. In cases of metal oxides, altered pH has led to reactive oxygen species (ROS) generation and peroxidation[150], which were associated with observed toxicity. While pH has been a common parameter to monitor and assess EHS of passive NMs, ANHs that are pH responsive present a more complex surface that evolve in response to this parameter; where the ANHs behave non-uniformly, depending on the type of the polymer and its chemistry. Not only the dynamic pH responsive coatings will evolve in response to the changing environment, the metallic NPs will also likely undergo enhanced dissolution and thereby influence toxicity.

Temperature is not considered a key factor in assessing nano-EHS. However, the use of thermal-responsive polymers in decorating ANHs, introduces new complexity in understanding their environmental and toxicological behavior. The temperature range at which these ANHs respond is within the range of physiological conditions (i.e., 31-38 ºC)[96]. These thermo-responsive ANHs thus when in human body or at elevated temperature, will allow exfoliation of the polymeric coatings influencing stability and

reactivity. However, when these ANHs are released to a natural environment, the polymeric coatings will likely collapse, thus altering the fate, transport, transformation, and toxicity of these particles. For example, PNIPA swells at room temperature but undergoes phase transition around 30 °C. This transition is perfectly reversible and PNIPA is thus a great candidate for design of ANHs with specific temperature-delivery applications[83]. PMAEMA on the other hand, shows temperature sensitivity similar to PNIPA but is a uniquely responsive polymer; as observed via its response to temperature and pH in aqueous solution[96]. While the process of shrinking and re-swelling can be repeated without degradation, the polymeric network will be fully accessible to any other material at low temperatures after its intended use and the ANH then serves as a vehicle for transport of other contaminants in the environment. Certainly, this cyclic 'swelling' and 'shrinking' would likely pose varied environmental partitioning, exposure, and uptake that have strong toxicological consequences. Studies showing acute toxicity of NMs dispersed in PNIPA to amphibians was observed but these particles were 'passive' [152] and therefore adaptive parameters had not been considered in toxicity studies to-date. It is plausible that ANHs designed to swell in high temperature (e.g., in human body) may collapse in the natural low temperature environment; which will almost certainly alter the toxicokinetics of the ANHs and their potential for adverse health effects. Thus, consideration of nano-EHS of these ANHs require assessments of their behavior in changing temperature conditions, where dramatic transition in their aggregation, deposition, and toxicity is likely when temperature is near the LCSTs of their polymeric coatings.

Transformation of passive NMs primarily focuses on studying the alteration of the particles' photoactivity[153], reactivity[154], and surface properties (via adsorption of geo- and bio-macromolecules)[76]. However, none of these NMs are designed to respond to photo-irradiation, rather such transformation occurs incidentally. On the other hand, ANHs possess functional moieties that are designed to respond to photo-activation, thus are more likely to undergo such transformation when released in the natural environment. For example, o-nitrobenzyl alcohol is a photo-sensitive group that uses as a photo-cleavable junction between hydrophilic and hydrophobic polymer blocks, and can form micelles for drug delivery applications[112]. Light triggers the breakage of the block copolymer chains at the junction points and the encapsulated drug is released. Thus, these materials can be more prone to photo-transformation, where ANH surfaces may not only lose their original surface coating (via cleavage or fragmentation upon photo-irradiation) and subsequently undergo ligand-exchange with environmental ligands, but can also present contrasting behavior (with the changing polymer morphology via photo-activation). Most of the literature on photo-toxicity has been performed with TiO_2 that primarily show that photo-oxidation increases ROS and toxicity. In fact, many studies have shown that cellular uptake of NMs is not necessary to induce toxicity, however, membrane damage by photo-oxidation mediated oxidative stress control the nanotoxicity mechanism[18,155,156].

The nano-EHS community needs to consider modification of the strategies on assessing these dynamically evolving stimuli-responsive ANHs. The underlying assumption of uniform surface properties in theoretical models and experimental assessment fall apart for these new sets of materials. The assumptions of potential

transformation in the environment are also not applicable, as some of these ANHs will certainly undergo transformation, if exposed to the relevant stimulus. Furthermore, parameters that are otherwise ignored in nano-EHS, e.g., temperature, will require more attention in case of these ANHs. New experimental tools are likely required to monitor dynamic evolution of the coatings under changing stimuli conditions. The current state-of-the-art techniques mostly assess equilibrium processes, and are not capable to evaluate time-dependent changes in surface properties.

With the growing number and composition of NMs–including contemporary ANHs–it is evident that a shift to predictive modeling is needed. A number of models have been proposed to meet the growing demand to satisfy EHS testing[157-159]. A recent paper on the current state of modeling in assessing nano-EHS in aquatic systems suggest that while the nano-EHS community is making significant progress in assessment of passive nanostructures, models are evolving to reflect the dynamic nature of both the particle and environmental system[157]. The ANHs introduce a new dynamism in nano-EHS studies, where stimuli-responsive coatings demand new models that can capture such dynamism. Similarly, 'real world' environments necessitate systematic assessment of nano-EHS in complex environmental conditions; e.g., heteroaggregation, multi-particle transport, surface area-dependent chemical transformations, and toxicity evaluation in realistic biological conditions. It is thus imperative that the EHS community needs to foil material complexity with system heterogeneity and take the next big step to reliable safety assessment of these new-generation nano-conjugates.

2.6 Carbon Nanotube Responses to Microwave Radiation

Beneficial physical characteristics of CNTs are encouraging for its use in electronics, medicine, material science, and environmental applications[160]. CNTs are single or multiple concentric all carbon tubules (single-walled SWNT or multiwalled MWNT) with open or closed ends[161,162].

When CNTs are irradiated with MW, strong energy absorption has been observed with subsequent strong heat release, outgassing, light emission, even nanotube reconfiguration and/or "welding" at elevated temperature (1500 ºC)[163]. Although the mechanism of CNT-MW interaction is only partly understood, MW systems are used for purification[164], chemical functionalization of CNTs[165], or to provide a reactive setting to stimulate the modification, e.g., curing, of other materials in presence of CNTs[166].

The rapid molecular rotation induced by electric field oscillation is the principal heat-generating pathway for solvents, e.g., water (dipolar polarization). Such rapid rotation at the solvent/solute boundary layer provides efficient localized mixing[27]. However, dipolar polarization seems to have little contribution to CNT-MW absorption, i.e., no electric dipoles exist in CNTs. Conduction heating, a phenomenon in which electrons are accelerated in an electric field, cause sample heating due to electrical resistance. Due to its unique one-dimensional shape and symmetry properties, CNTs have shown to be a ballistic conductor[167,168], meaning its resistance is quantized along the tube, is independent of length, and no energy is dissipated due to electron mobility[163]. Because of this low energy dissipation, CNTs have conductivities considerably higher than that of copper[168]. But in the case of raw CNTs, impurities acquired during synthesis (e.g.,

residual metal catalyst, support materials, disordered carbon, and other nanoparticles) result in reduced ballistic transport, and subsequently, heat emission. This mechanism, which initially appears to satisfactorily explain the heating in CNT-MW interactions still remains unclear[163,168].

Response of CNTs to electromagnetic radiation has been a subject of many exciting investigations[162]. For instance, CNT irradiation has been studied as a method for producing hyperthermia in cancer research. When Malignant cells are incubated *in vitro* and subsequently irradiated with radiofrequencies, heating of aqueous suspensions due to internalized CNTs, results in thermal destruction of cancer cells that contain internalized CNTs[169]. MWs constitute one of the more interesting possibilities among the frequencies that can be employed. Although the MW spectrum covers frequencies ranging from 300 MHz to 30 GHz, most microwave systems operate at designated frequencies of either 900 MHz or 2.45 GHz[170]. MW-enabled NH catalysts are being developed to replace widely used, but potentially toxic, TiO_2 and ZnO nanoparticle photocatalysts for environmental remediation applications (i.e., degradation of dyes from textile industries)[171]. Other potential applications include high-strength but low-weight electromagnetic interference (EMI) shielding materials[172]. Because a nanotube composite's electromagnetic (EM) shielding or absorbing efficiency is dependent on the electronic structure of the CNTs, the bulk properties of composites can be effectively tuned by altering the electronic structure of CNTs, via functionalization and hybridization[173].

2.7 KEY FINDINGS

This review was particularly focused on stimuli-responsive materials, which activate under an external chemical or physical stimulus. This vast literature made it possible to better understand the synergistic aspects of multicomponent constituents to gain a better understanding of the state of the NH materials field.

Stimulation via light or electromagnetic (EM) radiation is particularly useful to efficiently modulate NH responses. A number of parameters (light intensity, time of exposure, and wavelength) can be tuned for a specific target, which allows designing a wide selection of stimuli-responsive NHs. EM in the form of MW radiation is of particular interest to this study since MW appliances have diffused into societal fabric, globally, and can be taken advantage of to extract unintended benefits. Large and small communities, in urban or rural areas, can greatly benefit from the versatility and inclusiveness of this technology at centralized water treatment facilities or as point-of use treatment solutions.

When multiwalled carbon nanotubes (MWNTs) are hybridized with metal oxide nanomaterials, the resulting hybrids exhibit excellent light absorption in visible light region, which in return demonstrates photocatalytic action and charge separation to make these materials useful in a range of applications[38,84]. NHs that respond to EM radiation and will likely generate ROS, a key driver in bacterial inactivation, hold promise for a new irradiation-based technology. But, thus far, absorption of MW radiation and spectral conversion has not been combined. If successful, this NH will be capable of using a low energy source to provide spectral conversion to a higher energy, which will have

important implications as a new disinfection development. Thus, this dissertation will focus on MW as the EM radiation, and will aim to utilize this radiation as a stimulus that can result in generation of ROS and thus inactivate waterborne microorganisms.

Chapter 3: Harnessing the Power of Microwave for Inactivation with Nanohybrids[iii,iv]

3.1 INTRODUCTION

The motivation of this chapter emanates from nanomaterials' ability to harness electromagnetic (EM) radiation and thus potentially utilize it to inactivate waterborne microorganisms. After a comprehensive literature review on multifunctional properties of nano-heterostructures, a NH comprised of carbon nananotubes and lanthanide series metal oxides has been designed, synthesized, and characterized, and its efficacy in inactivating a model microorganism has been evaluated.

Microwave (MW) radiation is at the weak-end of the EM spectrum and hence is not typically as effective to inactivate microorganisms as the smaller wavelength radiation with higher energy potency (e.g., ultraviolet rays, x-rays, and gamma rays). To overcome this limitation, localizing the radiation and increasing the energy footprint is necessary. Only then can that energy be utilized for spectral conversion. Design of the NHs thus involved combining multiwalled carbon nanotubes (MWNTs), one of the most effective materials to absorb MW radiation, with lanthanide series oxides, which are known to be one of the most efficient metal oxides capable of spectral conversion.

Enhancing low-energy electromagnetic radiation, e.g., visible and near infrared radiation, has effectively produced ROS in the past[19]. Such amplification of low energy photons to higher energy has been successfully demonstrated using lanthanide series

[iii] **Plazas-Tuttle, J.**; Das, D.; Sabaraya, I. V.; Saleh, N. B. **(2017).** Harnessing the Power of Microwave for Inactivating *Pseudomonas Aeruginosa* with Nanohybrids. *Water Res.*, (*In review*).

[iv] Saleh, N. B. and **Plazas-Tuttle, J. (2016).** Microwave Absorbing Carbon-Metal Oxides and Modes of Using, Including Water Disinfection. (Patent Pending). Application #15230041.

metals (e.g., Er^{3+} and Tm^{3+})[21,22]. Such metal ions have $4f^n5s^25p^6$ electron configuration. Their unique $4f^n$ with $n = 0–14$ is responsible for their unique optical and magnetic properties. For n electrons in 14 available orbitals there are 14 over n possible configurations and all configurations can have different energies. Their 5*s* and 5*p* shells serve as a shield for the 4*f* inner shell, and thus, the electronic transitions are independent of the surrounding host materials. To-date, successful use of MW radiation for efficient inactivation has not been confirmed. However, there is promise in carbon nanomaterials' ability to absorb MW energy[25] and lanthanide series metal's capacity to enhance spectral-conversion[23], if successful hybridization is achieved, thus producing inactivation.

In this chapter, the MW absorption properties of carbon nanotubes (CNTs) and the spectral conversion-ability of lanthanide series metal erbium oxides are combined to study inactivation of waterborne microorganisms. Such a nanohybrid (NH) has been synthesized and correctly characterized. Inactivation of an opportunistic pathogen *P. aeruginosa* has been achieved using a conventional MW oven with the NH. The dominant mechanism underlying inactivation has been identified to be ROS-mediated inactivation. Results obtained in this chapter confirm a proof-of-concept of a new irradiation-based water disinfection technology that can utilize low-energy intensive and broadly available MW devices for microbial inactivation.

3.2 EXPERIMENTAL

3.2.1 Materials

Isopropanol (2-propanol, 99%, USP), nitric acid (70%), and concentrated sulfuric acid were obtained from Fisher Scientific (Houston, TX). MWNTs (> 95% carbon purity) with an average diameter of 8-15 nm and length of 10-50 μm were obtained from Cheap Tubes Inc., (Cambridgeport, VT). Amplex® UltraRed reagent (Cat. No. A36006) and Amplex® Red/UltraRed stop reagent (Cat. No. A33855) were procured from Invitrogen (Carlsbad, CA). Erbium(III) oxide (99.5%, REO) was purchased from Alfa Aesar™ (Ward Hill, MA) while erbium(III) nitrate pentahydrate (99.9% trace metal basis) was procured from Acros Organics™ (Geel, Belgium). Catalase (CAT), superoxide dismutase (SOD), and methanol (MET, 99.9%) were obtained from Sigma (St. Louis, MO). Other reagents were purchased from Fisher Scientific (Houston, TX), unless otherwise noted.

3.2.2 Synthesis of NHs

MWNTs with an average diameter of 8-15 nm and >95% purity (Cheap Tubes Inc., Cambridgeport, VT) were first acid-etched by refluxing in a 1:1 (v/v) mixture of concentrated nitric (70%) and sulfuric acid (96.5%) at 80 ºC for 3 h. Functionalized MWNTs were thoroughly washed with ultrapure water (Synergy ultrapure water, EMD Millipore, Darmstadt, Germany) and vacuum-filtered using porous polytetrafluoroethylene (PTFE) membrane filters (0.2 μM, EMD Millipore, Darmstadt, Germany). The MWNT cake obtained was washed with distilled water until the pH was neutral, dried in a desiccator, and subsequently hand-grinded with mortar and pestle to fine powder to be dispersed in anhydrous isopropanol with an ultrasonic dismembrator (Q700 Qsonica, Newtown, CT). NHs with three C:Er molar ratios, NH-1 (16:1), NH-2

(8:1), and NH-3 (4:1), were synthesized (Table A.1) via a sol gel process[34]. For this purpose, erbium precursor ($Er(NO_3)_3 \cdot 5H_2O$) was dissolved in isopropanol (Table A.1), bath sonicated, and added drop-wise at a constant rate (0.435 mL/min) to the previously dispersed MWNTs under ultra-high purity N_2 (NI UHP15A, Airgas) at 80 ºC for 3 h. The mixture was then evaporated and the residue was calcined under N_2 at 400 ºC for 3 h in a tube furnace (Lindberg/Blue M TF55035A-1, Thermo Scientific, Asheville, NC). Finally, the NHs were hand-grinded with mortar and pestle and dispersed ultrasonically in ultrapure water before use.

3.2.3 NHs Characterization

A rich suite of characterization tools has been utilized to determine particle morphology, crystallinity of the metal oxide nanocrystals on the surface of MWNTs, composition of the materials, and the chemical bonding of the metal oxides with MWNT surfaces. A JEOL 2010F HRTEM (JEOL USA Inc., Pleasanton, CA) at various magnifications and at an accelerating voltage of 200 kV collected MWNT and NH images. The same equipment was used to obtain high annular angle dark field STEM images at high magnification alongside with EDX to obtain elemental mapping of the materials. Crystalline structures of the powdered samples were investigated by performing XRD using a Rigaku R-axis Spider (Rigaku Americas Corporation, The Woodlands, TX). The XRD has a curved imaged plate diffractometer equipped with an image plate detector and Cu-Kα irradiator (0.154 nm wavelength) and a graphite monochromator. Thermal oxidation properties were examined using a TGA with differential scanning calorimetric capabilities (Mettler-Toledo AG, Schwerzenbach, Switzerland). TGA was performed by flowing air from 25 to 800 ºC with a heating ramp

of 10 ºC min^{-1}. XPS (Kratos Axis Ultra DLD, Kratos Analytical Ltd., Manchester, UK) spectra were recorded on dry powders to examine the surface chemistry of the samples.

3.2.4 Disinfection Potency

Microbial inactivation was assessed by exposing a Gram-negative opportunistic pathogenic strain of *P. aeruginosa* PAO1 to the NHs with appropriate controls. *P. aeruginosa* is ubiquitous in the natural environment, resistant to conventional disinfection, and its biofilm form protects it from chemical disinfectants, UV light, and other environmental stressors[174]; these attributes make it a perfect model microorganism that is more resistant than other planktonic bacteria[174]. A freezer stock of PAO1 was streaked on a Luria Bertani (LB) agar plate and grown overnight. A single colony from the plate was inoculated in 15 mL LB medium and incubated at 37 °C on a shaker (200 rpm) for 16 h. 100 µL of the culture was added to a fresh LB medium and was incubated at 37 °C for 4-6 h until the culture reached mid-exponential phase (optical density at 600 nm of 0.25-0.30). The suspension was then centrifuged (5810R, Eppendorf AG, Hamburg, Germany) at 2,500 × g for 15 min, and the supernatant was removed. The remaining cell residue was re-suspended in 15 mL 1X GibcoTM phosphate buffer saline (PBS) solution (Fisher Scientific, Pittsburgh, PA). This procedure of centrifugation and re-suspension in PBS media was repeated twice to remove the remaining LB growth medium. Concentrations of 10 mg/L erbium salts, erbium oxide, MWNTs, and NHs samples were prepared in 1X PBS as stocks. Each sample was autoclaved and bath sonicated for 30 min prior to the exposure studies. A 20-µL aliquot was then added to 180 µL of the bacterial suspension (in PBS) on a microtiter plate to achieve a final bacterial exposure concentration of 1 mg/L for each sample. A control was also prepared

by adding 20 μL sterile ultrapure DI water to the bacterial suspension to account for the same dilution as that of the other samples. Bacterial suspensions were then subjected to MW irradiation (20 s at 110 W), while an identical set of samples was kept in the dark for the same exposure time. Each sample was tested in triplicate. The samples were then serially diluted using 1X PBS, 10 μL samples were pipetted and grown on LB agar plates, incubated for 12-16 h at 37 ºC, and finally colonies were enumerated by viable plate counts.

3.2.5 Disinfection Mechanism Determination

During nanomaterial exposure, bacteria can experience stress from a selected set of stressors, among which dissolved metal ions and ROS are most common. Bacteria can also be stressed via heat shock and other chemical stressors, e.g., hydrogen peroxide. To identify the dominant underlying mechanism for disinfection, the following protocols were established.

Measuring Temperature Change

The temperature of the samples was measured by a k-type beaded wire stainless steel thermocouple (SC-GG-K-30-36, Omega, Stamford, CT) before and after MW irradiation. The thermocouple was connected to a digital thermometer (CL3512A, Omega, Stamford, CT), with a temperature range of -220 to 1372 °C. It is acknowledged that such measurements will produce bulk change in temperature and will be incapable of determining local variation at the nano-scale.

Determination of H_2O_2 Concentration

A non-radical derivative of oxygen as a surrogate for ROS, H_2O_2, was monitored with Amplex® UltraRed Reagent (Cat. No. A36006) hydrogen peroxide/peroxidase assay kit with Amplex® Red/UltraRed Stop Reagent (Cat. No. A33855). This compound is non-fluorescent until it is reacted with a combination of H_2O_2 and horseradish peroxidase. Samples of erbium salt, erbium oxide, MWNTs and NHs were individually dispersed in ultrapure DI water at 1 mg/L. The prepared samples and nanomaterial suspensions were added to the working solution of the ROS assay kit using a 96-well black assay microplate (Corning, NY), following the manufacturer's protocol. To evaluate the MW-induced H_2O_2 generation, the suspended samples were irradiated for 20 s at 110 W (611 mW·h) with a conventional MW oven (1100 W, 2.4 GHz, JES1460DSBB, GE®). An identical set of samples was kept in the dark for the same time of exposure. Amplex Ultrared stop reagent was added to each sample to capture the fluorescence of the oxidized product until measured using a Synergy-HT microplate reader (Biotek, Winooski, VT) with appropriate excitation (485 nm) and emission filters (590 nm). Each measurement was performed on triplicates and the background fluorescence intensity (for DI water) was subtracted from all readings.

ROS Scavengers

To further investigate the potential role of ROS by MW-irradiated NHs, CAT, SOD, and MET scavengers of H_2O_2, superoxide ($O_2^{\bullet-}$), and hydroxyl radical ($OH^{\bullet}$) respectively, were utilized. Cell suspensions (2 mL) were treated with 1.0 mg/L of NH-1 in the presence or absence of CAT (286 units, Sigma, St. Louis, MO), SOD (200 units Sigma, St. Louis, MO) and MET (0.3 M, Sigma, St. Louis, MO). The bacterial

suspensions were then subjected to MW irradiation (20 s at 110 W), while an identical set of samples was kept in the dark for the same exposure time. Each sample was tested in triplicates. Antimicrobiality was assessed by plating onto LB agar medium and subsequent counting of colonies following the method described in the disinfection potency section.

3.2.6 Enhanced Inactivation Performance

Additional experiments were performed to increase the inactivation performance of the irradiated samples. For this purpose, bacterial samples (with and without NPs) and appropriate controls were prepared as previously described in the disinfection potency section. Then, 200 μL sample were pipetted into wells of a microtiter plate, at equidistant points from the center of rotation of the MW oven's turntable, so that the samples could get equal amount of irradiation (Figure A.6). Bacterial suspensions were then subjected to MW irradiation (1X=20 s, 2X, 4X, and 8X, at 110 W), while an identical set of samples was kept in the dark. Each sample was tested in triplicates. The samples were then serially diluted using 1X PBS, and 10 μL samples were pipetted and grown on LB agar plates, incubated for 12-16 h at 37 ºC, and finally colonies were enumerated by direct count. Temperature of the sample was carefully controlled as mentioned earlier. This is important in order to avoid convolution of the inactivation mechanisms by introducing heat shock.

3.3 RESULTS AND DISCUSSION

3.3.1 Synthesis and Characterization of the NHs

NHs with three C:Er^{3+} molar ratios, i.e., 16:1 (NH-1), 8:1 (NH-2), and 4:1 (NH-3), were synthesized (Table A.1) via a sol gel process. Representative HRTEMs and STEM micrographs show successful hybridization of MWNTs with Er (Figure 3.1 and Figure A.1). The HRTEM micrograph displays debundled MWNTs with average shell thickness of 21.3±2.6 nm (Figure 3.1a), where some crystalline features are uniformly distributed at the surfaces of the MWNTs indicating hybridization with a metal/metal oxide nanocrystal (Figure 3.1b and Figure A.1). The elemental composition of the hybridized MWNTs and the uniformity of the metal oxide nanocrystals are presented via STEM imaging (Figure 3.1c). Representative STEM element-specific micrographs show uniform distribution for C, Er, and O, throughout the MWNT backbone. Control over synthesis with loading and distribution uniformity of erbium oxide on MWNTs is demonstrated via STEM images, elemental mapping, and elemental composition (Table A.2 and Figures A.2 and A.3).

Quantitation of elemental composition for the NHs is presented with XPS analysis (Figure 3.2a). XPS spectra for the NHs with varied Er loading reveal the presence of characteristic O1s, C1s, and Er 4d peaks (Figure 3.2a). O1s peaks (at 532 eV) are narrow and confirm the presence of different forms of erbium oxide and C-O bonds on the surface of the MWNTs. C1s (at 284.8 eV) peaks are typical for sp^3 hybridized C-C bonds. The region of Er 4d does not exhibit a typical free ion doublet structure at the region between binding energies of 167.5 and 169.5 eV, and the complex multiplet structure to the left of the peak at 169.5 eV is attenuated as shown by the 3 NH signals

(Figure 3.2b)[175]. However, the peaks at binding energy 169 eV are typical of Er_2O_3 compound, which will change the spacing and intensity of the doublet peaks after an annealing process[175]. The atomic ratios of C:Er^{3+} obtained (Table A.3) via XPS are 1.29 (NH-1), 0.72 (NH-2), and 0.19 (NH-3), which demonstrate achieving control over the hybridization process.

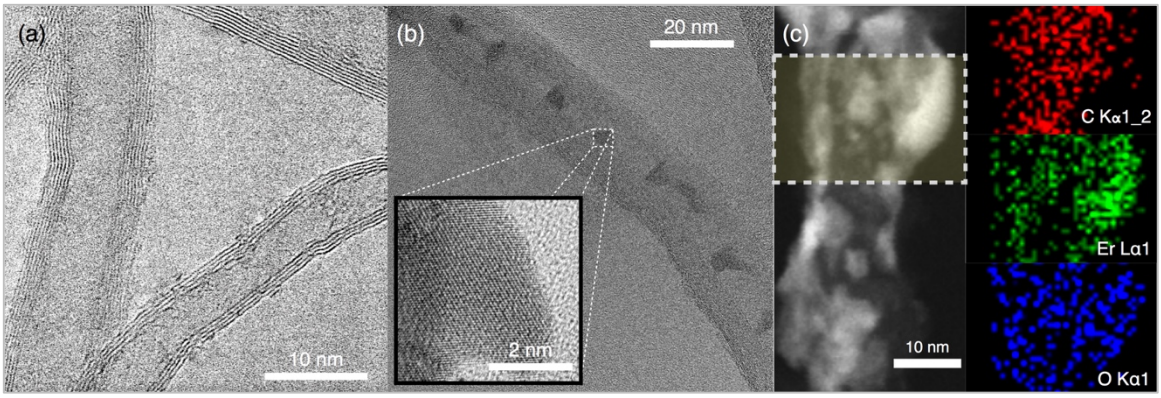

Figure 3.1: Representative HRTEM micrograph of (a) MWNT (> 95% carbon purity, 8-15 nm average diameter, and 10-50 μm length) and (b) NH-1 (inset shows crystalline erbium oxide lattices). (c) STEM image and elemental mapping of NH-1. Samples of aqueous dispersions for (a) and (b) were placed on lacey carbon coated copper TEM grids (SPI Supplies, West Chester, PA) and air-dried over a few minutes. HRTEM and STEM accelerating voltage set to 200 kV. Several representative micrographs were obtained.

EDS (Table A.2) and XPS analyses (Table A.3) on the three NHs showed consistent results for the Er nanocrystal loading on MWNTs. Estimating the precise stoichiometry of the reactions is challenging due to a lack of information on the accurate spatial distribution of the carboxylic groups on the nanotubes as well as due to the variations in number and type of defect sites specific to each individual tube. These factors have an influence on the position and configuration of nanocrystals in the

resulting NH. In light of the latter, Tables A.2 and A.3 demonstrate that the quantity of Er has been overestimated when compared to the reagents added during synthesis.

The crystallinity of erbium oxides on MWNT surfaces is confirmed with XRD spectra (Figure 3.2c). MWNT XRD spectrum (gray) shows a distinctive sharp peak and small broad peaks at 26.3º and 43º, which correspond to (002) and (100) lattice planes, respectively[176]. The XRD spectrum of erbium oxide (dash blue) shows highly crystalline Er_2O_3 signature with a sharp peak at 29.4°, which corresponds to (222) diffraction planes. Other diffraction planes analyzed, i.e., (211), (431), (440), and (622), are consistent with literature reports[177]. The XRD spectrum of the representative NH-1 shows suppressed peak occurrences for those of the MWNTs. The relatively less defined peaks for NHs indicate either presence of amorphous structures, which can be hydroxides and/or oxides of Er metal[178]. The chemical binding between the metal structures and the MWNTs can also cause such broadening of the peaks[178]. Further adjustment of the synthesis conditions, e.g., calcination temperature, may lead to more ordered nanostructures.

To determine whether the erbium oxide nanocrystals crystalized onto MWNT surfaces with no chemical bonding or rather true hybridization has been achieved, peak oxidation temperature of the MWNTs and NHs is determined. TGA results (Figure 3.2d) show a significant downward shift of the peak oxidation temperature (from 636 ºC to 475 ºC) for MWNTs upon hybridization. Such a shift can be attributed to enhanced heat flow onto MWNT surfaces via chemically bonded metallic nanocrystals[179,180]. The downward shift in the peak temperature persisted with the increase in erbium oxide content, which further supports the heat flow analysis. Analyzing the %mass loss profiles of these

materials (Figure A.4) reveals mass remaining percentages of unhybridized and hybridized MWNTs, i.e., 6.8% (MWNT), 48.1% (NH-1), 60.7% (NH-2), and 73.2% (NH-3), which concur well with the metal content analysis obtained from EDX (Table S2). The differences between XPS and TGA/EDX ratios for $C:Er^{3+}$ suggest that erbium oxides are being crystalized not only on the surfaces but might also be incorporated within the carbon tubules as may be observed in Figure 3.1b.

3.3.2 Disinfection Potency

Inactivation of the opportunistic pathogen *P. aeruginosa* with an initial population density of ~10^7 CFU/mL is successfully achieved with MW irradiation in presence of NHs (Figure 3.3). The control samples (irradiated and non-irradiated Er salt, Er oxide particles, and MWNTs) show no significant impact on bacterial viability (Figure 3.3a). NH-1 shows at least one log unit reduction of *P. aeruginosa* when compared to appropriate non-irradiated controls and other irradiated materials. Inactivation of *P. aeruginosa* with other samples is not observed. The increase in Er oxide loading onto MWNTs (irradiated samples) shows a negative correlation with bacterial viability reduction (Figure 3.3b).

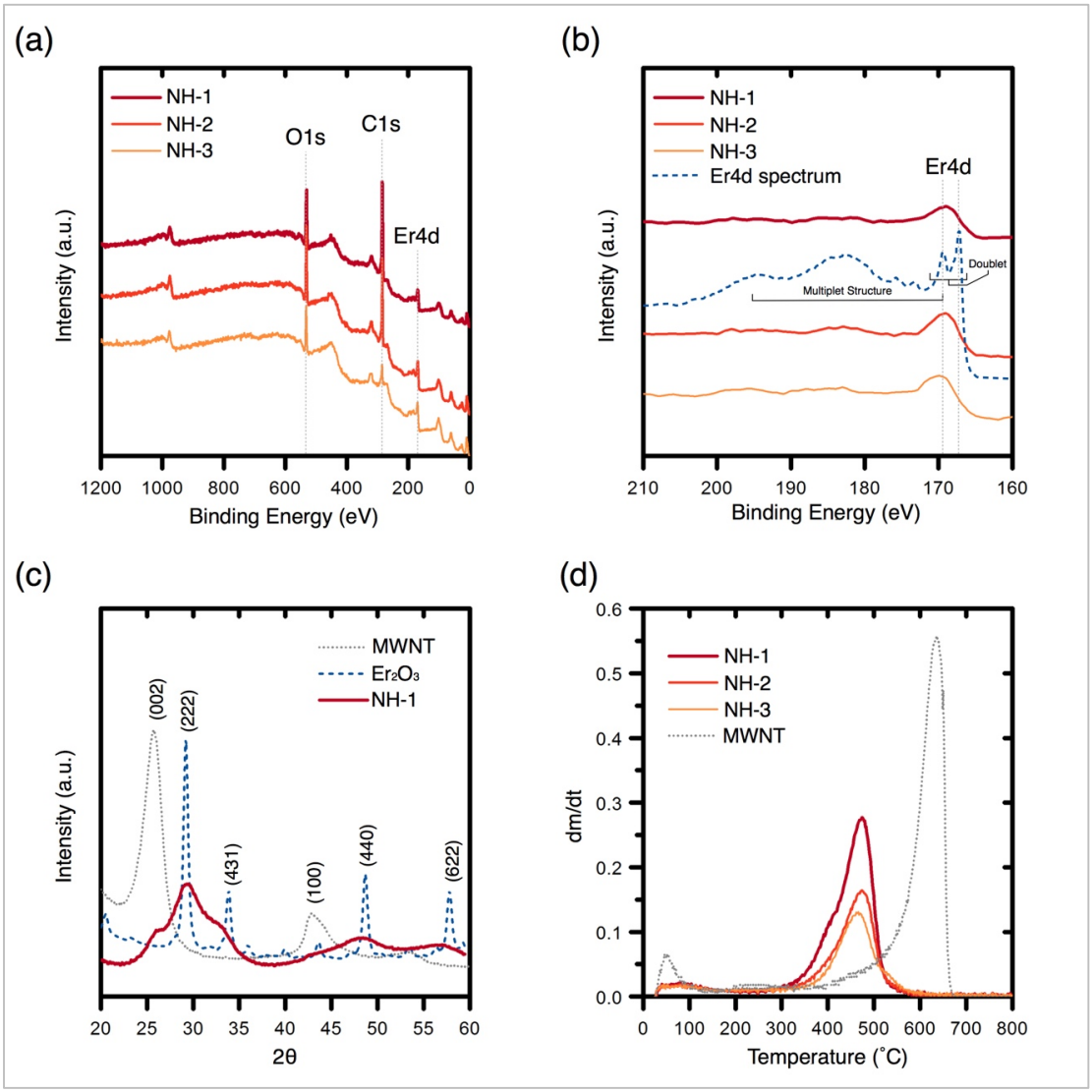

Figure 3.2: (a) XPS spectra, (b) XPS region displaying typical Er4d multiplet structure, (c) XRD spectra of MWNT, erbium oxide, and NH-1, and (d) differential mass loss curve from TGA for the MWNT and NHs. Thin layers of dried samples were analyzed using a Kratos XPS equipped with a monochromated Al K_α X-ray source (1.486 keV). XRD equiped with Cu-Kα irradiator (0.154 nm wavelength) and a graphite monochromator was used at a step width of 0.02° (between 2θ values of 20° and 60°) and a scanning rate of 2° min^{-1}. Dry samples (3-5 mg) were heated at 10 ºC min^{-1} ramp up to 800 ºC for TGA/DTG determination.

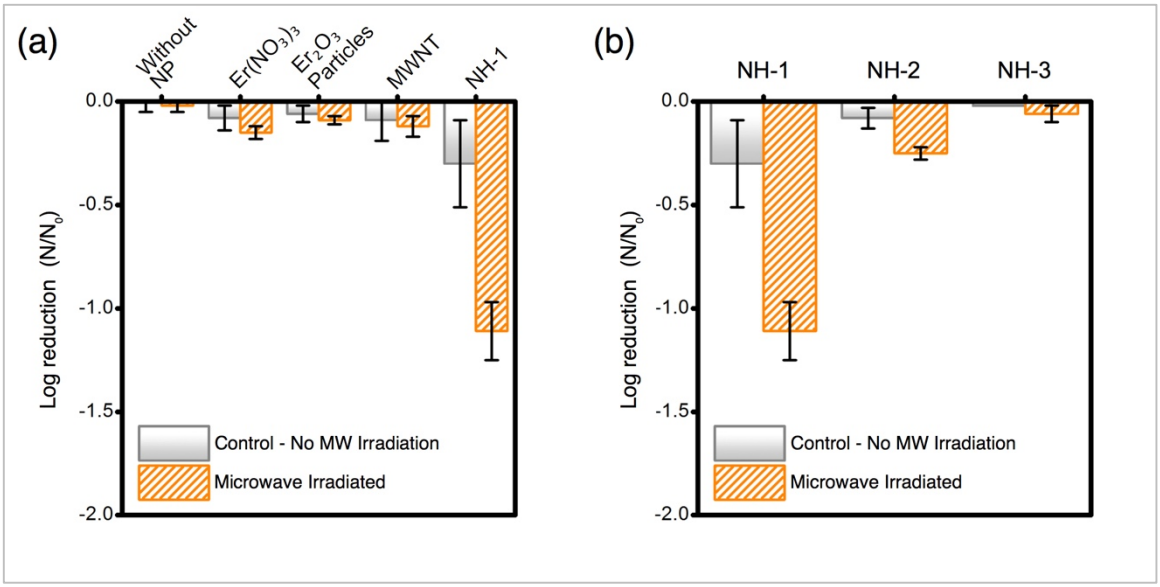

Figure 3.3: (a) Bacterial inactivation of *P. aeruginosa* exposed to NH-1, and appropriate controls; (b) comparison of logarithmic cell removal of *P. aeruginosa* exposed to NHs. Material concentration utilized in all experiments was maintained at 1 mg/L. Initial concentration of *P. aeruginosa* ~10^7 CFU/mL. Samples (200 µL) were irradiated in microtiter plates for 20 s at 110 W (611 mW·h) using a conventional MW oven. Error bars represent one standard deviation measured from experimental triplicates. NP: nanoparticle, MWNT: multiwalled nanotube, NH: nanohybrid.

Microwave's potency of inactivating *P. aeruginosa* compares well with literature reports; however, such reports are based on photocatalytic disinfection of water as a function of a complex set of variables. Our study presents breakthrough inactivation results, and as such, comparison of these results with other reported data is presented to highlight its potential to compete with other irradiation-based technologies. Literature evidence suggests that strains of *P. aeruginosa* (AOH1 and NCIMB 10421), when exposed to photocatalytic Ag-TiO_2 films and irradiated with UV for at least 1-6 h, can result in one log bacterial reduction (energy expenditure: 2.24 mW·cm^{-2})[181]. Similarly

single log inactivation of *P. aeruginosa* (NCTC 10662) was also achieved by photocatalytic TiO_2 thin film treatment, when irradiated with UV (3 $mW \cdot cm^{-2}$) for 35 min[182]. Comparable inactivation efficiency of *P. aeruginosa* (ATCC 9027) is observed for solar irradiated TiO_2 when irradiated for 1 h (energy expenditure: 1 kW·h)[183]. *Escherichia coli* (OH157:H7), a more susceptible bacterial species to irradiative inactivation (compared to *P. aeruginosa*), underwent single log inactivation with C_{70}-modified TiO_2 NHs under 10 min irradiation of visible light (energy expenditure: 0.05 kW·h). The results presented herein demonstrate superior inactivation performance of the novel NHs prepared in this study, where an opportunistic pathogenic strain is irradiated with the lowest intensity electromagnetic radiation, MWs. In this study, a significant reduction in exposure time (20 s) and expended energy (0.0006 kW·h) compared to literature reported UV and visible radiation excited nanomaterial cases, further proves the efficacy and transformative nature of this nano-enabled disinfection technology.

3.3.3 Proposed Disinfection Mechanisms.

Dissolution of metal ions

Literature suggests that dissolution of metal ions from high curvature nano-sized particles can serve as a dominant mechanism for disinfection; e.g., nano-Ag, which contributes ionic silver, is utilized as an effective disinfectant[135]. The NHs utilized in this study, however, contain a lanthanide series metal oxide (i.e., erbium), which has extremely low aqueous solubility[184], thus likely will not incur antimicrobiality via dissolution. Results presented in Figure 3.3a further validates this claim. *P. aeruginosa* when exposed to dissolved Er^{3+} in an amount equivalent to Er present in the NHs show

no appreciable inactivation. Thus, dissolved ions are not likely the cause of bacterial inactivation in this case.

Microwave Heating

An increase of temperature over time can result in denaturation, damage to the cell membrane, and coagulation of protein materials inside the bacterial cells, affecting their viability. Studies have shown that viable counts of high bacterial density cultures of *P. aeruginosa* (1.7×10^9 CFU cm^{-2}) decrease up to 6 orders of magnitude when subjected to 50-80 ºC for 1-30 min[185]. However, the maximum temperature change recorded in this study is 2.10±0.30 ºC from room temperature, when the samples were MW-irradiated for 20 s at 110 W (Table A.4 and Figure A.5). Such evidence suggests that inactivation by thermal shock of *P. aeruginosa* or MW heating is unlikely to be the dominant mechanism for inactivation for this study; however, it should be noted that adaptation of *P. aeruginosa* to temperature change needs further assessment. As indicated above, a global change of temperature may not play a significant role on bacterial inactivation; however, local temperature at the NH-water interface might experience higher temperature differentials, and such changes might occur over a short duration. Both the local temperature changes (hyperthermia) and its rate of change may contribute to stresses that *P. aeruginosa* might experience in such conditions[185,186]. These effects need to be further evaluated.

Synergistic Effects of combined MW heating and ROS species

Antimicrobial action via MW heating can be enhanced significantly if complemented with a low concentration of H_2O_2[187]. Both cell destruction and DNA injuries can be achieved as shown for exposure of *E. coli* (K-12) and *P. aeruginosa* (102) to consecutive MW irradiation (up to 50 ºC) and addition of H_2O_2 (0.08% v/v). It is believed that the synergistic effects consist of inhibition of the repair mechanisms in bacteria due to ROS addition. However, in this study, no additional H_2O_2 was added to the system. The range of temperature increase (~2 ºC) and no H_2O_2 addition thus remove this mechanism as a possible route for disinfection in this study.

ROS-Mediated Microbial Inactivation

The remaining possible mechanism for disinfection is extracellular ROS, which can be produced due to irradiation of the samples with an external energy source (i.e., MW). Formation of H_2O_2 species is measured as a surrogate for ROS generation in this study (Figure 3.4). When irradiated with MW, NH-1 produces at least two twice the amount of H_2O_2 (8.71 μM) compared to the unirradiated case (4.46 μM), and at least 7 times as much as the control samples (i.e., Er salt, Er oxide, and MWNTs) as shown in Figure 3.4a. It is possible that the peroxide production in the absence of MW radiation is due to stray visible light impacting the NH, as can be observed in the un-irradiated case (Figure 3.4a). NH-1 (16:1 molar ratio) is the most effective of the 3 NHs synthesized in producing H_2O_2 (Figure 3.4b). The increase in Er loading on MWNTs negatively correlates with the ROS production ability, as presented in Figure 3.4b. NH-2 and NH-3 do not produce significant amounts of H_2O_2 as compared to NH-1. A balance between the

MW absorption ability of the MWNTs and the electron donation capacity of the metal oxides is necessary to achieve enhanced disinfection efficiency.

The role of catalases in in protecting planktonic and biofilm cells of *P. aeruginosa* against H_2O_2 has been investigated in previous studies[188]. Such investigations have reveal that cell viability decreased steadily in planktonic cells exposed to a single dose of peroxide, whereas cell viability remains steady after an initial decrease when *P. aeruginosa* is exposed to H_2O_2, meaning that bacteria can quickly adapt to ROS stressors. The effect of H_2O_2 was the only species measured and the synergistic effect of other ROS species has not been evaluated.

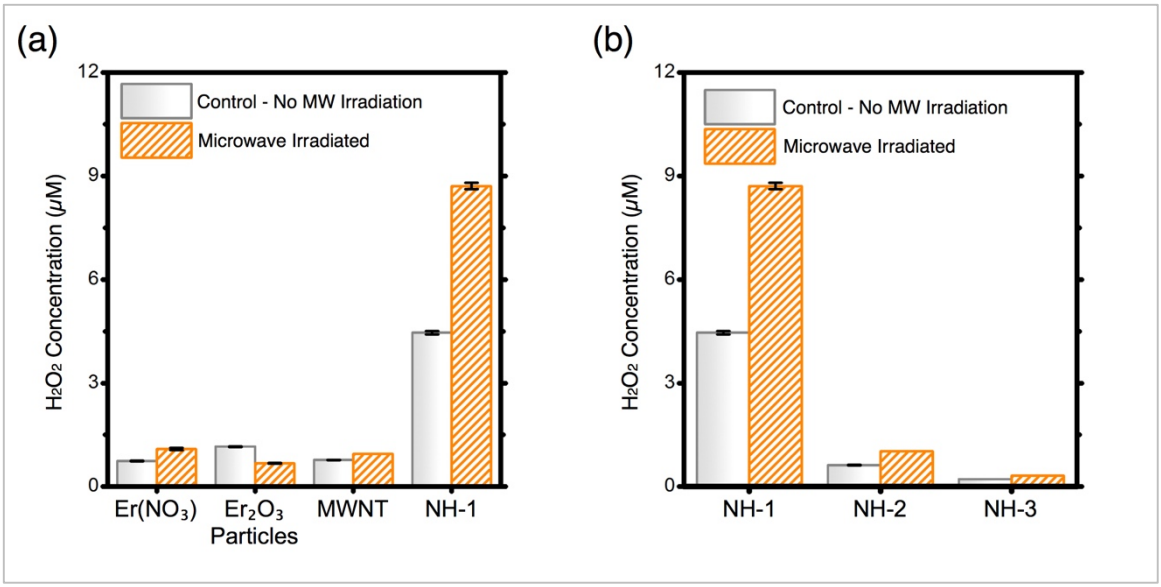

Figure 3.4. (a) H_2O_2 production with and without MW irradiation by NH-1 and by the appropriate controls; (b) comparison of ROS production between the NHs. Material concentration utilized in all experiments was maintained at 1 mg/L. Samples (100 µL) were irradiated in microtiter plates for 20 s at 110 W (611 mW·h) using a conventional MW oven. LOD is 100 CFU/mL. Error bars represent one standard deviation measured from experimental triplicates.

ROS scanvenger study

Bacterial inactivation in the presence of CAT, SOD, and MET scavengers definitively prove that ROS played a leading role in the antimicrobiality of *P. aeruginosa*. Figure 3.5 shows that significant bacterial inactivation was not observed in any of the controls, irrespective of MW irradiation. What these results particularly reveal is that NH-1, when irradiated with MW in presence of any (or all) of the three scavengers shows little to no inactivation, but it shows 1.64±0.09 log removal of bacteria in absence of the scavengers. Such scavenger studies have been utilized in earlier studies to demonstrate a definitive role of ROS in antimicrobiality[189-192].

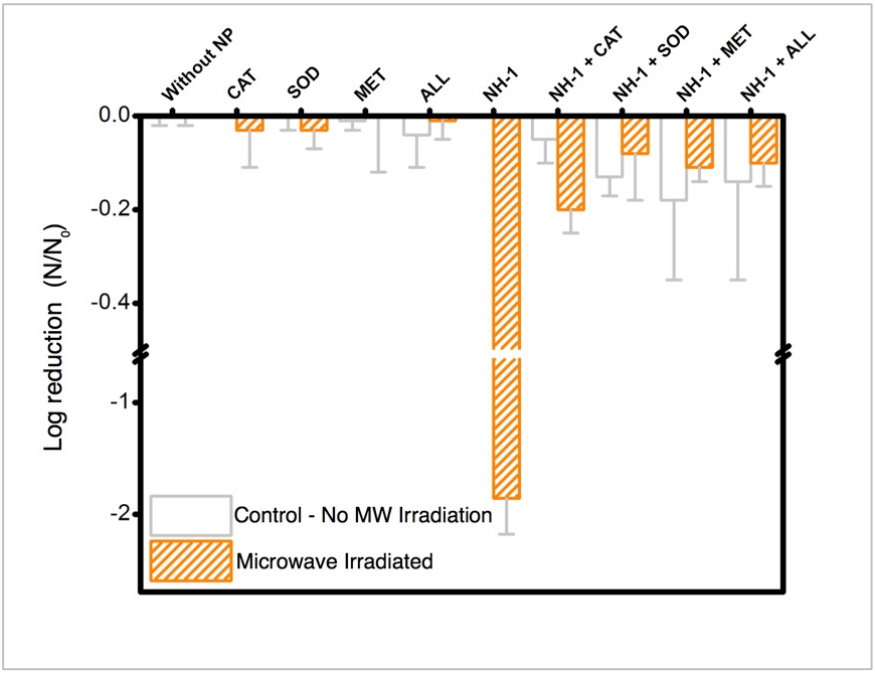

Figure 3.5. Logarithmic cell reduction of *P. aeruginosa* exposed to NH-1 with and without H_2O_2, $O_2^{\bullet-}$, and $OH^{\bullet}$, scavengers CAT, SOD, and MET, respectively. Material concentration utilized in all experiments is maintained at 1 mg/L. Samples (200 µL) were irradiated in microtiter plates for 20 s at 110 W (611 mW·h) using a conventional MW oven. LOD is 100 CFU/mL. Error bars represent one standard deviation measured from triplicate samples.

Enhanced Inactivation Performance Results

Results after irradiation of bacteria in the presence of NH-1, confirm more than 1-log inactivation of *P. aeruginosa*. Significant inactivation is accomplished only after MW irradiation is performed (Figure 3.6). Importantly, samples irradiated for longer periods of time, in 20 s intervals, show a minor increase in logarithmic reduction after a second cycle of irradiation of *P. aeruginosa* (initial population density of ~10^7 CFU/mL), but they did not show any further increase in inactivation upon additional cycles of irradiation (Figure 3.6). Log reduction reaches a maximum of 1.25±0.07 after the second cycle. A possible explanation might lie in the aggregation propensity of the NHs, thus affecting their distribution in the aqueous solution and thus losing available sites for harnessing MW and generating ROS, which eventually causes the inactivation. Further studies to assess the role of NH aggregation during an extended period of irradiation need to be performed. However, this limitation can be avoided by device engineering, where the NHs will not be suspended in the water sample but will be immobilized, for instance on a surface. However, such immobilization of the NHs could also limit the ability to produce ROS in sufficient amount. Device engineering thus needs immediate attention to further this technology.

It is also to be noted that the experiments were performed under a strong electrolyte condition (in presence of the buffer), hence can induce aggregation to the NHs. Thus, MW harnessing process by the nanotube surfaces might become limited and ROS produced might also be sequestered within the aggregates, limiting the potency to inactivation. Thus, subsequent cycles of irradiation, for NH-1, show limited enhancement in inactivation (Figure 3.6).

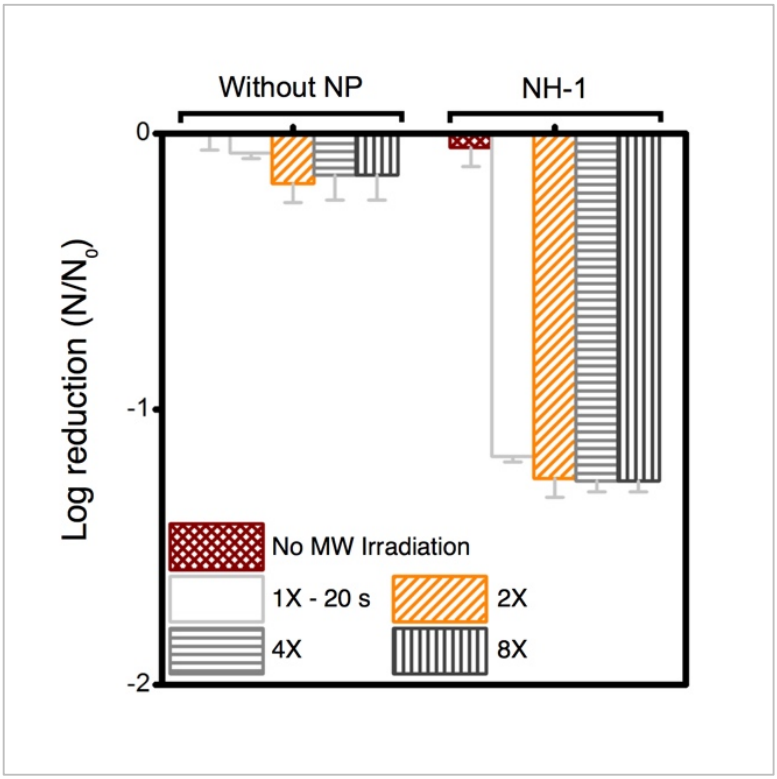

Figure 3.6: Inactivation of *P. aeruginosa* exposed to NH-1, and appropriate controls; Bacterial cells were irradiated for 1X (20 s), 2X, 4X, and 8X duration. Temperature upon 8X irradiation increased no more than 20 °C. NH concentration utilized in all experiments was maintained at 1 mg/L. Samples (200 µL) were irradiated in microtiter plates at 110 W (611 mW·h) using a conventional MW oven. LOD is 100 CFU/mL. Error bars represent one standard deviation, measured from experimental triplicates.

3.3.4 Possible ROS-Generation Mechanisms

The synergistic effect of MWNT and Er_2O_3 to favorably generate ROS may be explained with published literature on photocatalytic nanomaterials, e.g., carbon nanotubes-TiO_2 nanohybrids[193-200]. The overall phenomenon is likely a two-step process of electron promotion and subsequent electron transport to the neighboring MWNT or

Er_2O_3 surfaces with the following possible scenarios. i) MW absorption ability of MWNTs likely allows for the weak and otherwise dissipated MW energy to be localized on the tubular carbon surfaces (Figures 3.7a and 3.7 b)[25]. MWNTs acting as sensitizers, absorb this energy and as a result electron-hole pairs are generated on the MWNTs (Eq. 3.1 and Figure 3.7c). An energized electron from MWNT can get transported to chemically bonded Er_2O_3's conduction band allowing the formation of superoxide radicals (Eq. 3.2). ii) Subsequently, the positively charged MWNTs can remove an electron[201] from the valence band of Er_2O_3, leaving a hole on the metal oxide crystal, which can then react with water to form hydroxyl radicals (Eq. 3.3). iii) Alternatively, the localized energy may reach sufficient intensity to excite electrons from Er_2O_3 valence band to a higher energy state, while leaving a hole behind. The promoted electron on Er_2O_3 crystals can either react with dissolved oxygen in the surrounding water envelope to form ROS or iv) can get transported to MWNT (due to its exceptional electron transport ability[201]) and generate ROS via the pathway described earlier. The potential pathways of electron-hole pair formation and ROS generation are illustrated in Figure 3.7d and captured in the following set of reactions. It is to be noted that these ROS species undergo further reactions to form hydrogen peroxide (Appendix C), which has been measured in this study.

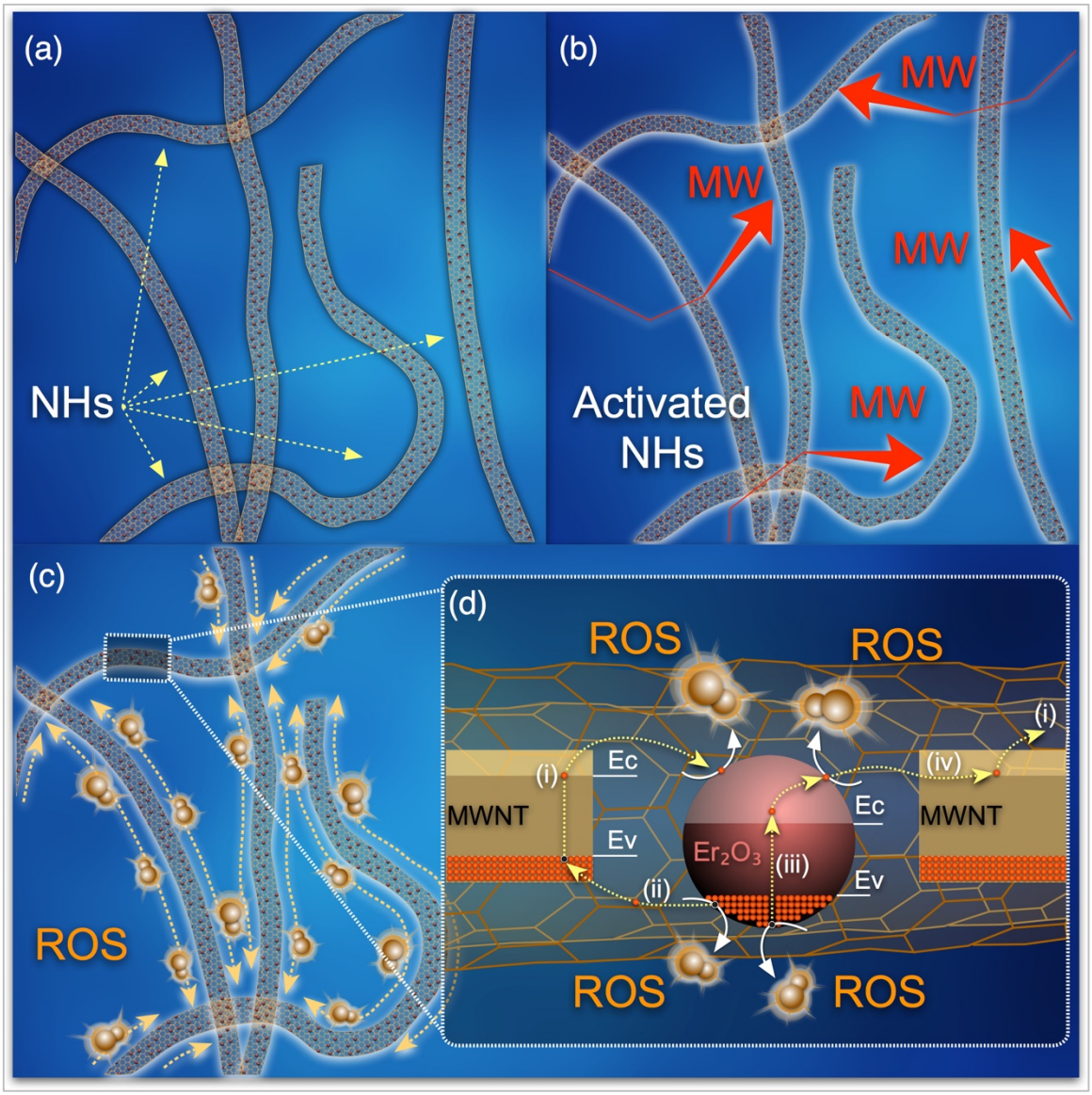

Figure 3.7: Schematic representation of possible underlying mechanisms for ROS generation. (a) NHs suspended or attached to a relevant carrier in contact with water, (b) MW energy absorption by the NHs, (c) absorbed MW energy is transferred to neighboring nanocrystals resulting in charge separation and generation electron-hole pairs in the erbium oxide layer and MWNTs that will produce ROS, and (d) potential pathways of electron-hole pair formation and ROS generation.

$$MWNT/Er_2O_3 \xrightarrow{MW} MWNT/Er_2O_3 + h^+ + e^- \quad \textbf{Eq. 3.1}$$

$$O_2 + e^- \rightarrow O_2^{\bullet -} \quad \textbf{Eq. 3.2}$$

$$H_2O + h^+ \rightarrow OH^{\bullet} + H^+ \quad \textbf{Eq. 3.3}$$

It is also reported that modification of the electromagnetic properties of MWNTs via hybridization with Er oxide results in improved MW absorbing abilities[202], and carbon-oxygen-erbium bonds eventually enable expansion of electromagnetic absorption range[195]. Such phenomena also can lead to improvement of catalytic activity of the NHs.

We acknowledge that generated ROS are temporal in nature and undergo a series of consecutive reactions where these acquire different chemical form (details in Appendix C). H_2O_2 forms as a reaction product and appears in a later period in the reaction sequence (Section S1). Production of H_2O_2 in this study is thus likely a result of electron donation from the NHs when irradiated with MW and production of molecular superoxide radical. It is to be noted that formation of other ROS is yet to be determined, which will further elucidate the kinetics of oxygen species formation and their subsequent effects in disinfection. Electron spin resonance spectroscopy with appropriate spin traps can be utilized to determine all ROS generated in this disinfection process.

3.3.5 Key Findings

This is the first study that has developed a nano-scale heterostructure effective in harnessing and utilizing MW radiation for ROS production and microbial inactivation. Synergistic abilities of MWNTs' MW absorption-ability with lanthanide series oxides' spectral conversion-capacity has allowed for successful charge-separation and generation of ROS. Effective inactivation of waterborne microorganisms via ROS generation with the lowest energy radiation (MW) at exceptionally low energy cost (0.0006 kW·h) is potentially transformative. This simple yet elegant technological breakthrough will allow achieving a beneficial unintended use (of disinfection) from this widely-distributed MW technology. The nascent benefits of MW, i.e., its ability to operate in absence of clear optical pathways (e.g., in turbid waters), its diffused presence deep into the societal fabric, and its potentially low economic and energetic footprints will allow for future implementation as an effective point-of-use water treatment solution. The authors acknowledge challenges that this technology will need to overcome to be the panacea and serve as a platform for disinfection processes in the future. Factors such as costs of the technology as compared to proven existing disinfection processes, treatable volume of water, material lifespan, and effectiveness of treating water with a wide range of physical and chemical characteristics are yet to be determined. Mode of application of the material to achieve an effective operational and maintenance feat and systematic evaluation of nano environmental health and safety issues have also to be determined. Once the material design and parameters of irradiation are optimized and this technology is further developed as an affordable and effective point-of-use system, it can potentially be transformative to impact a global population by gaining them access to safe drinking water.

Chapter 4: Exploration of the Roles of Wavelength and Irradiation Time of MW on Inactivation Potency of *P. aeruginosa*

4.1 INTRODUCTION

Optimization the efficacy of this nano-scale heterostruction, effective in harnessing and utilizing MW radiation for ROS production and bacterial inactivation necessitates defining and controlling the wavelength (or frequency), irradiation time, and other important parameters. To reveal the mechanism(s) of reactive oxygen species (ROS) production, the first challenge is to attain control over the incident radiation, to correctly characterize the energetics of the system. A kitchen microwave, like the one used in studies described in Chapter 3, lacks control over the irradiation process (in terms of the wavelength and irradiation intensity) and thus an improved design of the microwave (MW) irradiation system must be developed.

This study aims to develop a reactor where incident MW radiation parameters can be controlled and the radiation can be guided into a water sample containing microorganisms of concern. The setup consisting of a MW power generator has been connected to a copper waveguide. Conventional MW frequency (2450 MHz) has been used for such a design. The copper waveguide guarantees that a sample inserted will receive the maximum MW radiation energy and input power. Baseline measurements are performed to confirm the most appropriate sample holder material. Temperature of DI water and NHs suspended in DI and contained in quartz and borosilicate tubes is measured. Cyclic irradiation is also investigated to control temperature increase in the irradiated samples. Finally, inactivation of *P. aeruginosa* is studied for a range of MW frequency, input power, and irradiation time. Results obtained in this chapter provide

guidance for parameter control of a MW-irradiation based microorganism inactivation system.

4.1.1 MW Frequency and Wavelength

MWs are electromagnetic (EM) radiation at frequencies between 300 MHz and 300 GHz frequency[27]. Like all EM waves, MWs propagate in free space at the speed of light (Figure 4.1). EM waves have both electric and magnetic components (electric field and magnetic field), and the wavelength is related to frequency as follows.

$$\lambda = c/f \qquad \textbf{Eq. 4.1}$$

Where λ is the wavelength (in m), c is the speed of light (3×10^8 m/s), and f is the frequency (in Hz). To avoid interference between different MW applications, e.g., air-traffic control, weather forecasting, and telecommunications, a limited number of frequency bands are assigned. The US Federal Communications Commission (FCC) allocates frequency bands for industrial, scientific, and medical (ISM) applications, with basic frequencies centered around 896 MHz and 2450 MHz for industrial and domestic purposes, respectively[203].

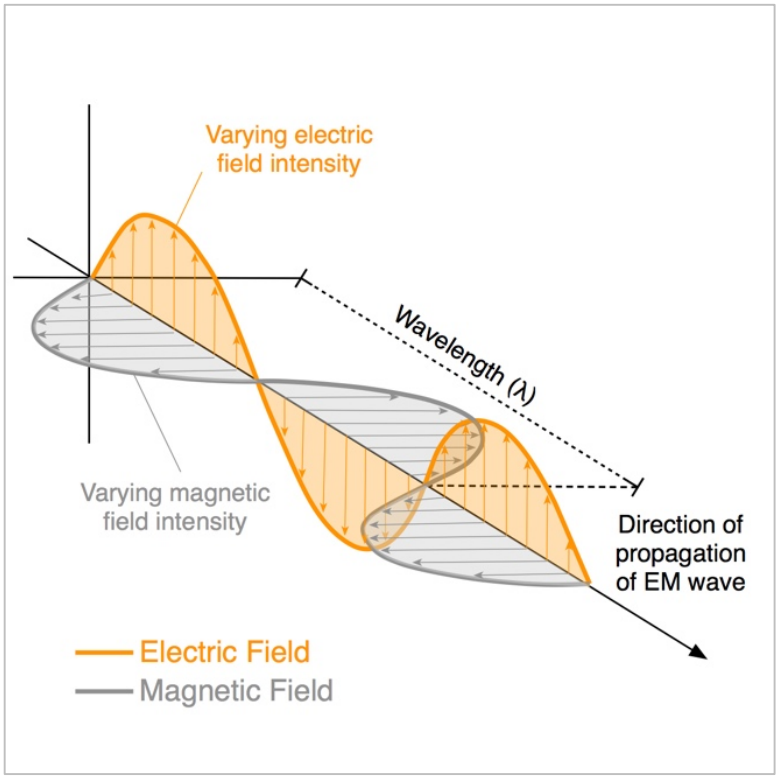

Figure 4.1: Components of an EM wave.

4.1.2 Waveguide

Waveguides can be considered as "transmission lines" for high frequency EM waves[204,205]. For such frequencies, EM signals and power are usually transmitted via coaxial line, i.e., a wire inside a cylindrical outer-conductor. If the central conductor in such coaxial line is removed, it can still carry EM power –a remarkable phenomenon that occurs at higher frequencies only. In other words, at high frequencies a hollow tube will work just as well as wires[204,205]. By convention, since the "conduit" is being used to carry waves, such a conveyor is called a waveguide which may have either circular or rectangular cross sections (Figure 4.2 a and b).

Design of a waveguide involves measuring the EM wave using a slotted line setup as follows. Energy can be conducted into a waveguide by an antenna (vertical wire or driving stub). Figure 4.2a shows the schematic of a driving stub used to connect a coaxial cable transmitting MW power to a rectangular waveguide. In order to quantify the EM energy an additional stub serving as a probe (pickup stub) can be connected to a detector, and moved back and forth along the guide (slotted line) to determine the values and locations of the maximum and minimum EM fields waves (Figure 4.2c).

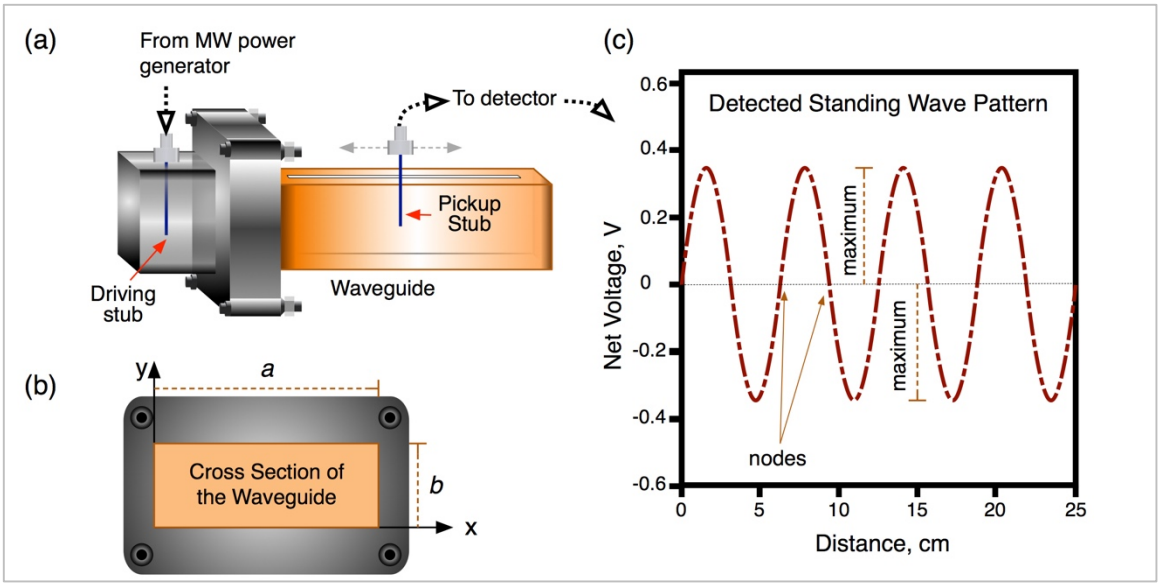

Figure 4.2: Schematic representation of: (a) a uniform rectangular waveguide with driving and pickup stubs for waveguide design (slotted line) (b) cross section of the rectangular waveguide, and (c) example of detector standing wave pattern.

Cutoff frequency

The lower cutoff frequency (or upper cutoff wavelength) defines the limits of operation of a waveguide. Frequencies below the lower cutoff frequency do not propagate down the guide. The accepted limits of operation for rectangular waveguides are approximately between 135% and 189% of the lower cutoff frequency. Waveguides can support many modes of transmission. The mode depicted in the rectangular waveguide in Figure 4.2a is called transverse electric (or $TE_{m,n}$) mode. Subscripts *m*, and *n* represent the number of ½-wavelength variations of fields in the "*a*" dimension (broad-wall) and the "*b*" dimension (short-wall). Other kinds of transmission modes are described elsewhere[204,205] and will be dictated by the geometry of the cross section of the waveguide. The lower cutoff frequency, f_{lc}, or upper cutoff wavelength (λ_{uc}) for this $TE_{m,n}$ mode is given by:

$$f_{lc} = c/(2 \cdot a), \lambda_{uc} = 2 \cdot a \qquad \textbf{Eq. 4.2}$$

Where, *a* is the dimension of the broad wall and *c* is the speed of light defined previously. The upper cutoff frequency is exactly one octave above the lower cutoff frequency. Thus, $f_{uc} = 2 \times f_{lc}$ [205]. If the signal generator, e.g., MW generator, is set at a frequency in the range between the lower and upper cutoffs, there will be waves propagating down the guide from the driving stub. At laboratory-scale, infinitely long waveguides can be studied and modeled by terminating the guide with an absorber in such a way that there are no reflections from the far end. Then, since the detector measures the time average of the fields near the probe, it will pick up a signal which is independent of the position along the guide; its output will be proportional to the power being transmitted[204].

However, if the far end of the guide is shut in a way that produces a reflected wave, e.g. closed-off with a cooper sheet, there will be a reflected wave in addition to the incoming forward wave. These two waves will interfere and produce a *standing wave* inside the guide. If a pickup probe is moved along the slotted line (Figure 4.2a), the detector reading will rise and fall periodically, showing a *maximum* in the fields at each loop of the standing wave and a *minimum* at each node (Figure 4.2c). The existence of a *maximum* and a *minimum* allow for the design of a sample port cavity in which a sample can be placed so as to receive the maximum irradiation from a MW power generator.

The free-space wavelength (λ_0), or wavelength in vacuum, is different than the real wavelength that travels through the waveguide with a unique guide wavelength (λ_g). The relationship between the two also involves the uppercut wavelength (λ_{uc}), and the dimension of the broad wall (a) and is given as follows:

$$\frac{1}{{\lambda_g}^2} - \frac{1}{{\lambda_0}^2} = \frac{1}{{\lambda_{uc}}^2} = \frac{1}{(2a)^2} \qquad \textbf{Eq. 4.3}$$

The distance between two successive nodes of the standing wave is ½ the wavelength in the waveguide ($½\lambda_g$). This gives a convenient way of measuring the guide wavelength[204]. The wavelength in the guide can also be calculated as:

$$\lambda_g = \frac{\lambda_0}{\sqrt{1-(\lambda_0/\lambda_{uc})^2}} = \frac{\lambda_0}{\sqrt{1-(\lambda_0/2\cdot a)^2}} \qquad \textbf{Eq. 4.4}$$

Where λ_g is the wavelength of the oscillations along the z-direction (the "guide wavelength"), λ_0 is the free-space wavelength (also equal to c/f) and a is the width of the rectangular waveguide as defined earlier.

By calculating λ_g, one can easily determine the maximum (peak) and minimum (node) values of the wavelength in the waveguide, and thus, the location of the points of maximum and minimum radiation for an exposed sample.

Material Selection for the Sample Vessel

MW can generate heat by directly transforming the EM energy into molecular kinetic energy. Heat generated by a certain volume is a function of the electric field strength, the frequency, and dielectric properties of the material represented by its MW power dissipation:

$$P = 2\pi f \varepsilon_0 \varepsilon_r'' E^2 \qquad \textbf{Eq. 4.5}$$

Where P is the power absorbed per unit volume or volume energy density (W/m^3), f is the operating frequency (Hz), ε_0 is the permittivity of free space ($8.85418782 \times 10^{-12}$ $m^{-3} \cdot kg^{-1} \cdot s^4 \cdot A^2$), ε_r'' is the dielectric loss factor, and E is the electric field strength in (V/m). The loss factor is dependent on both the frequency and temperature. The higher the loss factor of a material, the better the substance can be heated with MW irradiation. By determining the heat loss, one can select a material that is "transparent" to MW radiation, and does not generate heat by absorbing radiation. Thus, a material with a low loss factor is essential

to ensure that biological irradiated samples are unaffected by external factors, e.g., temperature increase, by the sample vessel.

Depending on the MW absorption behavior, materials can be classified as: (i) absorbers, e.g., water ($\varepsilon_r'' = 0.15^*$); (ii) transparents, e.g., fused quartz ($\varepsilon_r'' = 0.0001^*$) or Teflon($\varepsilon_r'' = 0.00015^*$); and (iii) reflectors, e.g., metals, graphite[205]. A high loss factor for water and other diluted aqueous substances results in significant MW energy absorption. Unfortunately, on account of complexity within interrelationships among parameters, calculations of field strength distribution, and therefore volume energy density are only possible for simple and ideal experiments. Thus, design of a MW reactor and its components still depends strongly on experience and trial runs[205].

4.2 EXPERIMENTAL

4.2.1 Microwave Power Generator

A variable MW power generator (GMP150, Opthos Instruments Inc., Rockville, MD) was used to generate MW radiation at the desired wavelength or frequency (Figure 4.3a and 4.3b). The operating frequency of the generator is 2.45 GHz ± 25 MHz, and it is capable of measuring incident and reflected MW intensities (0–150 W at 1-W resolution). The unit has built-in protection to manage total reflected power (i.e., reflected power needs to be less than 50 W over 1 min or greater duration). Ripple in the radiofrequency signal is less than 0.2%, providing a stable radiation signal that is sensitive to small changes in frequency and wavelength.

* Measured at 3 GHz.

4.2.2 MW waveguide

A copper reactor was designed and fabricated and a waveguide is utilized to irradiate the samples with MW radiation at a desired wavelength (or frequency) (Figure 4.3a and 4.3b). This design is modified from a previously published work that used a similar setup to study MW absorption by MWNTs [166] and to detect MWNTs in biological samples[206,207]. The MW power generator is equipped with a coaxial radiofrequency (RF) cable that connects to a brass waveguide (WR340-CPRF 2.10-3.00 GHz, Microtech, Cheshire, CT) (Figure 4.3b and 4.3c). The waveguide extends through a custom-built copper reaction chamber (l = 16.000 cm; a = 8.634 cm; b = 4.317 cm), which is closed at its far end with a removable copper lid and is sealed with copper tape to avoid radiation leak. By using Eq. 4.4, the length of the chamber can be calculated from the driving stub in the WR340 (17.32 cm), i.e., λ_g. Thus, a hole to insert a quartz vial was drilled at 4.33 cm (¼ λ_g) from the closed end of the copper chamber. This ensures that the sample is located at an EM maximum and that each sample is uniformly exposed to the same radiation conditions.

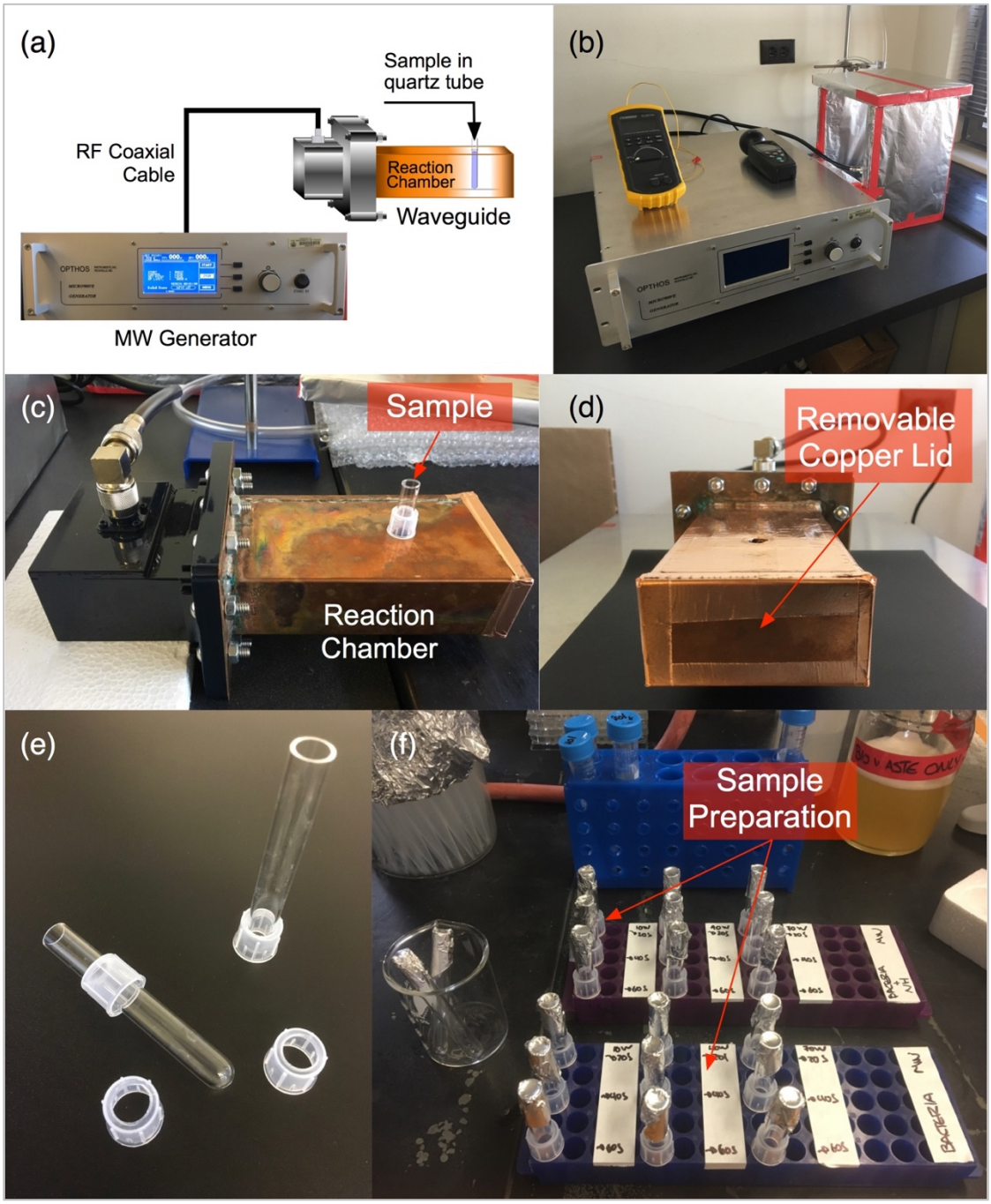

Figure 4.3: (a) Schematic representation of the MW setup, (b) MW power generator, (c) waveguide and copper reaction chamber, (d) closed end of the copper reaction chamber, (e) quartz vials and sample holders, and (f) sample preparation in sterilized quartz tubes.

4.2.3 Bacterial Propagation

Reference cultures of *P. aeruginosa* PAO1 were used to prepare standardized stock and working cultures were utilized for the inactivation studies. The reference culture was rehydrated in 25 mL LB medium in a 250-mL Erlenmeyer flask. The suspension was incubated for 20 ± 4 h at 36 ± 2 ºC on a shaker table operating at 150 rpm. Glycerol cryo-protectant was added to the flask (10 mL), mixed well, and distributed into cryogenic vials (1 mL aliquots) and stored at -80 ºC. This first passage of the bacteria is the stock culture. To prepare working cultures, one vial of stock culture was thawed at room temperature and inoculated on a LB agar plate by streak plating to obtain colonies. The agar plate was incubated for 20 ± 4 h at 36 ± 2 ºC, and after the colonies were visible, 3-5 individual colonies were aseptically inoculated into a 25-30 mL Erlenmeyer flask (250 mL). The suspension was then incubated for 5 ± 1 h at 36 ± 2 ºC on a shaker table operating at 150 rpm. Glycerol (10 mL) was added at the end of the incubation period. After mixing the suspension, 1-mL aliquots were prepared and stored at -80 ºC. Advantages of using working cultures include same starting conditions of the bacteria for every set of experiments and increased reproducibility of results. The protocol followed was modified from ISO 10705-1:1995 (Section 10. Preparation of Test Materials)[208].

4.2.4 Inactivation Efficiency

P. aeruginosa inactivation was used to benchmark the reactor study. Each experiment required preparation of a fresh bacterial culture. A working culture of *P. aeruginosa* was thawed overnight in fresh LB media, and the next morning, fresh LB media (15 mL) was inoculated with 200 μL of overnight culture. *P. aeruginosa* was

grown until the optical density measured at 600 nm reached 0.25-0.30, which occurred after 2.5 h of incubation. The suspension was then kept in wet ice at 4±1 °C to slow down replication of bacterial cells until ready for use. For optimal results, the bacterial suspension was used within 2 h of incubation. The suspension was then centrifuged (5810R, Eppendorf AG, Hamburg, Germany) at 5000 × g for 15 min, and the supernatant was removed. The remaining cell residue was re-suspended in 15 mL sterile 1X PBS solution (Fisher Scientific, Pittsburgh, PA). This procedure of centrifugation and re-suspension in PBS media was repeated twice to remove the remaining LB growth medium. A 10 mg/L concentration of NH-1 was used to prepare dilutions of 1 mg/L final nanoparticle concentration.

Two identical sets of samples were prepared for each experiment (Figure 4.3f); one set where bacteria was exposed to NH-1 (1 mg/L final concentration) and was irradiated with MW, while the second where bacteria was irradiated with MW but in absence of the NH-1. Positive controls, i.e., unirradiated bacteria and unirradiated bacteria exposed to NH-1, were also prepared for each run. Each sample was added to a quartz vial (10 × 75 mm, glassblowing shop, Department of Chemistry, The University of Texas at Austin, Austin, TX) (Figure 4.3e). Each sample was tested in triplicates, which were serially diluted (PBS) and plated on LB agar plates. Dried plates were incubated for 16 ± 4 h at 36 ± 2 ºC, and viable colonies were counted.

Inactivation efficiency is presented in terms of logarithmic fraction remaining and is calculated by:

$$Log\ reduction = \log_{10} \frac{N_0}{N} \qquad \textbf{Eq. 4.6}$$

where, N_0 and N are the number of viable microorganisms (i.e., formed colonies) before and after treatment, respectively.

4.2.5 Experimental Matrix

In order to determine the optimum conditions for spectral conversion, aqueous suspensions were exposed to different MW frequencies (2445, 2450, and 2455 MHz), MW power (20, 40, 60 W), and irradiation times (20, 40, and 60 s), as shown in Table 4.1. The temperature of the sample was monitored with a K-type stainless steel thermocouple (Omega, Model SC-GG-K- 30–36, ungrounded, 0.032'' diameter). The thermocouple was connected to a digital multimeter (HHM9007R), which read the temperature of the sample (range -200 to 1372 °C). The increase in temperature of aqueous suspensions was used to establish a baseline for wavelength, MW power, and exposure time for the experiments.

Table 4.1: Experimental matrix. MW frequency was maintained at 2445, 2450, and 2455 MHz.

Time (s) / MW Power (W)	20	40	60
20	✓	✓	✓
40	✓	✓	✓
60	✓	✓	✓

4.3 RESULTS AND DISCUSSION

4.3.1 Baseline Measurements

To establish a baseline, a series of measurements were conducted with the assembled copper reactor. Material selection and geometry of the sample holder were considered first. Borosilicate glass[v] ($\varepsilon_r'' = 0.001^*$) and fused quartz ($\varepsilon_r'' = 0.0001$) were compared using a 1 mL DI water while irradiating the samples with MW (2450 MHz at 70 W). Change in temperature of the transparent materials was monitored and is presented in Figure 4.4a. Quartz absorbs less MW radiation than borosilicate as was expected from the characteristic ε_r'' values of these materials. Consequently, quartz was used in all the microbial inactivation studies. Figure 4.4b, compares the change in temperature due to MW absorption for a sample of DI water and a sample of DI water with 1 mg/L NH-1. Temperature differences between the two samples were not significant; hence, NH-1 will not be a source of heat for these experiments.

[v] 10 × 75 mm, Fisherbrand 14-961-25, Fisher Scientific, Pittsburgh, PA.

[*] Retrieved from: https://brainresearchlab.com/wp-content/uploads/2013/12/Borosilicate-Glass%C2%A0Product-Information.pdf

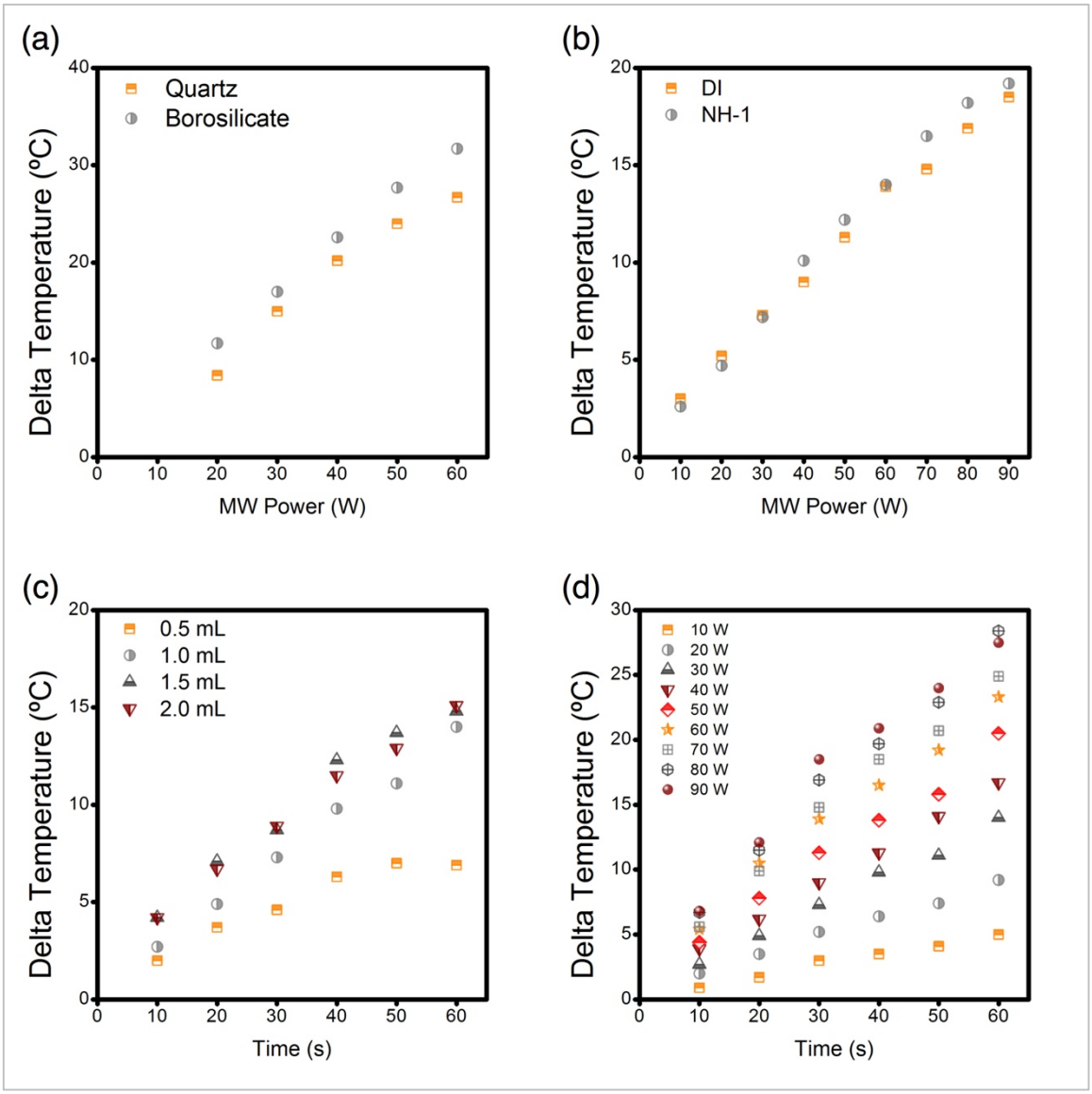

Figure 4.4: Temperature change for samples as a function of MW power input and irradiation time for: (a) DI water samples in borosilicate and quartz vials, (b) DI water samples with and without 1 mg/L NH-1, (c) different volume of DI samples (at 30 W MW power), and (d) DI samples in a quartz vial with a range of input power. All experiments were conducted under 2450 MHz MW irradiation.

To select a sample volume, quartz tubes with 0.5, 1.0, 1.5, and 2.0 mL were irradiated (2450 MHz at 30 W) and temperature was measured before and after irradiation (Figure 4.4c). Small volumes result in rapid temperature changes as samples tend to equilibrate with room temperature rapidly. Large volumes are not desired because of higher material preparation requirements. Thus, 1 mL volumes were selected for all inactivation studies.

Temperature changes were recorded when samples were irradiated (10-60s in 10 s increments) at 2450 MHz, for varying MW input power (10-90 W in 10 W increments) (Figure 4.4d). The objective of these measurements was to determine the operational conditions for the MW generator, so that temperature change in the sample can be kept to a minimum.

Table 4.2: Sample temperature changes after irradiation at different frequencies, MW power, and irradiation intervals (1X = 20 s, 3X = 3 times 20 s, and 6X = 6 times 20 s). Baseline temperature is 4 ºC.

	2445 MHz		**2450 MHz**			**2455 MHz**	
	40 W	**60 W**	**20 W**	**40 W**	**60 W**	**40 W**	**60 W**
1X	12±0.0	18.3±0.0	8.00±0.0	14.00±0.0	19.50±0.0	14.7±0.0	21.7±0.0
3X	11.8±1.3	17.97±0.3	8.00±0.0	13.17±0.7	19.95±0.7	14.77±1.2	21.03±0.7
6X	12.4±0.5	18.9±0.5	8.13±0.34	13.83±1.1	20.23±0.9	15.63±0.6	22.83±0.8

Finally, temperature changes were recorded as samples were irradiated for 20 s, 60 s (in three 20 s intervals), and 120 s (in six 20 s intervals), while varying the MW input power and frequency (Table 4.2). Samples were irradiated and immediately returned to wet ice within 5 s to control the temperature. Results of this measurement

indicate that *P. aeruginosa* samples irradiated in successive cycles will not be affected by temperature increase of the solution as the final temperatures do not increase more than 50 ºC.

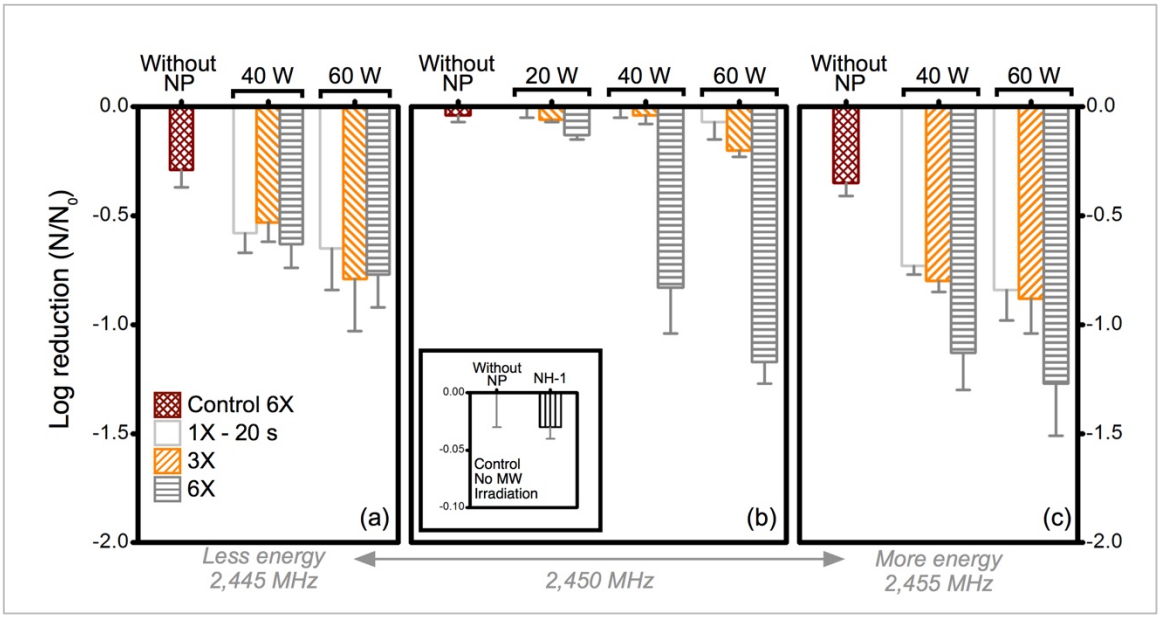

Figure 4.5: Log reduction of *P. aeruginosa* exposed to NH-1 when irradiated with (a) 2445 MHz, (b) 2450 MHz, and (c) 2455 MHz radiation for 1X = 20 s, 3X = 3 times 20 s, and 6X = 6 times 20 s at input power of 20 W, 40 W, and 60 W. Controls with no MW irradiation are presented in the inset figure. Irradiated controls were measured only for the highest irradiation condition (i.e., 6X irradiation time at 60 W). NH concentration utilized in all experiments is maintained at 1 mg/L. Initial concentration of *P. aeruginosa* ~10^7 CFU/mL. LOD is 100 CFU/mL. Error bars represent one standard deviation measured from triplicates.

4.3.2 Bacterial Inactivation Results and Optimization

Inactivation results of *P. aeruginosa* after irradiation with and without the presence of NH-1 under a wide range of incident radiation frequency (2445, 2450, and

2455 MHz), input power (20, 40, and 60 W), and irradiation time (1X = 20 s, 3X = 3 times 20 s, and 6X = 6 times 20 s) is presented in Figure 4.5. A maximum input power of 60 W was selected for a comparison between the three frequencies tested for protection of the MW power generator. Larger incidence MW power (e.g., 70 W) at 2455 MHz results in reflected power values above 50 W. Thus, the MW power generator is automatically shut down for protection of the electronic components.

Results indicate that maximum reduction of *P. aeruginosa* achieved at any condition is no more than 1.25 log units, irrespective of irradiation frequency, time, or input power. Increase in irradiation time and input power both showed minor influence on inactivation enhancement (except in the case of 2450 MHz frequency where 120 s irradiation time appeared to be most effective. Below, a detailed discussion of each of the panels are given below.

Figure 4.5a shows that inactivation increases slightly with the increase in power (from 0.63±0.11 to 0.77±0.15 log removal achieved for 40 and 60 W, respectively). However, no significant difference in inactivation was observed for increased irradiation time (values were within one standard deviation for all these cases). At this frequency, 60 s irradiation with 60 W input power will result in highest inactivation. Figure 4.5b shows interesting difference in trend, particularly for irradiation time. Input power showed consistent enhancement in activation; however, irradiation of 60 s showed the most effect for both 40 and 60 W power. These results appear to deviate from the expected trend, and require further analysis to verify accuracy of the measurements. However, it is to be noted that inactivation achieved for 120 s irradiation with 60 W power is comparable to

that achieved with the conventional MW, as presented earlier. Panel 'c' shows a similar trend as observed in panel 'a', that is influence of irradiation time and input power was minor at 2455 MHz. However, this frequency showed the highest log removal (1.27±0.24) among any of the cases studied, when irradiated for 120 s at 60 W input power. It is to be noted that these are the first evidences of bacterial inactivation using a controlled MW system. Further optimization of the NH design as well as device engineering are necessary to achieve higher inactivation.

4.3.3 Key Findings

This chapter describes design and construction of a MW waveguide enabled reactor, which can now be utilized to study microbial inactivation with MW with a high degree of control over key irradiation parameters. Baseline measurements performed on this setup has identified guideline values of MW frequency, input power, and irradiation time that limit the temperature rise to a maximum of 20 °C. Inactivation of *P. aeruginosa* has been achieved for a range of MW frequency, input power, and irradiation time. Increasing these parameters results in a minor increase of bacterial inactivation. However, the maximum inactivation achieved has not exceeded 1.25 log units, regardless of the irradiation parameter utilized. These results are encouraging. Using the waveguide-reactor and guidelines parameter values the use of these materials can be elevated to a disinfection technology.

Chapter 5: Evaluation of Inactivation Efficacy for a Wide Range of Waterborne Microorganisms

5.1 INTRODUCTION

Disinfection of water involves inactivation of a wide variety of disease-causing microorganisms. Pathogenic microorganisms in drinking water come in all varieties and types including bacteria, viruses, algae, protozoa, and helminths[209]. Some pathogenic microorganisms in these groups originate from fecal discharges of humans and other animals. Examples include *E. coli* O157, *Legionella*, rotaviruses, hepatitis E virus, norovirus, *Cryptosporidium*, and *Giardia*[210]. Conventional disinfection methods, such as chlorination, ozonation, and UV disinfection, have proven to be highly effective in bacterial[4] inactivation. However, the formation of harmful disinfection by-products during chemical-based disinfection (i.e., chlorination and ozonation), has raised concerns and initiated development of alternate non-chemical-based technologies[9]. Furthermore, highly effective alternative technologies are desired to inactive some pathogens, e.g., protozoan cysts[4] and viruses[211], that have high resistance to chemical disinfectants.

Understanding the efficacy of the developed NH to inactivate a wide range of waterborne microorganisms is essential for this technology to progress further as a potential disinfection solution. This chapter presents assessment results of the nanohybrids (NH) to inactivate surrogates of pathogenic bacteria, viruses, and protozoa. These species are *Bacillus subtilis*, *Legionella pneumophila*, *Escherichia coli* bacteriophage MS2, and *Flavobacterium columnare* (relevant to aquaculture water quality). Details on each of the microorganisms are described in the following section. To inactivate these microorganisms, the waveguide-reactor setup described in Chapter 4 has

been used. Conventional MW frequency (2450 MHz) and 70 W input power have been employed for all inactivation studies. Baseline measurements for each microorganism have been performed to establish initial resistance to inactivation. Results presented in this chapter can serve as a guideline for redesign of the NHs to achieve higher log-removal of a wide range of waterborne microorganisms.

5.1.1 Selected Microorganisms

Bacillus subtilis

B. subtilis is a Gram-positive disinfection-resistant spore-forming bacterium, ubiquitous in nature[212]. *B. subtilis* has been shown to be less sensitive than common Gram-negative bacteria to the effects of alternative disinfection technologies such as UV[18,190]. Because of their high resistance to disinfection, spores of *B. subtilis* have been used as an appropriate surrogate to assess inactivation of protozoan cysts, i.e., *Giardia lamblia* cysts and *Cryptosporidium parvum* (oo)cysts, in drinking water[213,214]. Even if bacillus spores are not indicators of the presence of protozoan parasites in environmental systems (Lytle et al., 1996), it is possible to correlate their inactivation with that of the protozoan cysts[213]. Use of an indicator is needed due to the high costs associated with cyst detection, their complex identification techniques, and difficult reproducibility of results. Conventional irradiation based disinfection methods are not successful to eliminate protozoa cysts from water[215]. Thus, this study offers a great opportunity to explore a new irradiation method on these infectious microorganisms.

Legionella pneumophila

L. pneumophila, is a motile, rod-shaped, Gram-negative, aerobic, and facultative organism that affects the elderly, those with chronic or pulmonary diseases, and those ewith a suppressed immune system. *Legionella* thrives in warm aquatic environments (shower heads, air conditioning systems, cooling towers, etc.) and in rust, algae, and organic particles[216]. Infections to humans are frequently caused by inhalation of aerosolized droplets containing infectious cells[217]. *L. pneumophila* is the leading cause of Legionnaires' disease[218] and the bacterium selects to grow inside other organisms, e.g., amoebae, where it reproduces intracellularly using the internal constituents of its host[216]. *L. pneumophila* is more challenging to inactivate when associated with amoeba and even more challenging when associated with amoeba cysts[216]. Currently, chemical disinfectants, e.g., chlorine, bromine, iodine, chlorine dioxide, and copper and silver ions, are used with thermal treatment, i.e., heat treatment at >60 ºC, to inactivate this pathogen. Alternatives to conventional water disinfection technologies are being explored[219]. *Legionella* spp. have shown to be sensitive to relatively low levels of H_2O_2 and $O_2^{\bullet-}$[220], which is why this MW irradiation based technique might be effective.

MS2 bacteriophage

MS2 phage is a RNA coliphage virus within the family Leviviridae that infects *E. coli*[221,222]. Because of its small size (capsid 23 nm), shape (icosahedral), relatively simple composition (molecular weight 3.5-4.3 × 10^6 kb), and ease of culture[222], MS2 is used as a model organism to study viral inactivation[190]. MS2 have also been frequently used as surrogates of human enteric viruses and thus has extensively been studied in water during drinking water treatment processes[223-225]. MS2 infects coliform bacteria by attaching to

the side of their pilus via its single maturation protein. F-pili are the mating organelles of *E. coli*, enabling male bacteria to transfer a partial single-stranded copy of their chromosome to female bacteria, which do not possess pili. These ribbon-like structures are composed of a single protein polymerized into a long flagellum (1-2 μm), that protrudes from the cell. The precise mechanism by which this phage's RNA enters the bacterium is unknown. However, once inside the cell, viral RNA begins to function as messenger RNA for the assembly of phage proteins. In a highly-regulated process, coat proteins are immediately translated, and only then, the lysis gene is expressed enabling the bacterial machinery to produce additional lysis proteins. Additional information on replication of MS2 is available elsewhere[222]. Bacterial lysis is then activated, and release of newly formed MS2 virions occurs when sufficient lysis protein has been produced. Irreversibly, lysis proteins attack the host's cytoplasmic membrane, resulting in loss of membrane potential and release of new viral particles[221,222]. This new batch of MS2 viral particles, are then protected by their coat of proteins, which makes them more resistant to UV disinfection than are enteroviruses and enteric bacteria; thus, making it an excellent surrogate candidate for enteric virus disinfection studies[226].

Flavobacterium columnare

To expand the possible use of this new technology to indoor aquaculture setting, *Flavobacterium columnare*, a waterborne microorganism that causes the disease columnaris in fishes in the southeastern U.S., also has been selected. Most species of fish are susceptible to *F. columnare,* particularly after temperature related environmental stress (25-32 ºC range) in the spring through fall seasons[227]. Inactivation of this pathogens in aquaculture water is essential to maintain production volume. Though

aquaculture is the fastest growing food-producing sector in the U.S. and is currently constitutes nearly 50% of seafood supply[228], the presence of waterborne pathogens in high-density fish farming operations is identified as a primary cause for global aquaculture crop loss. One-fifth to half of the aquaculture production is lost to bacterial, viral, protozoan, and fungal attacks[229].

F. columnare are fastidious, filamentous, Gram-negative, slender gliding rods that are slow-growing microorganisms requiring specialized medium for optimal growth in the laboratory[230]. This species is strictly aerobic and can survive for extended periods in water[230]. Additionally, *F. columnare* has been recovered from biofilms that act as reservoirs and thus allows them to protect themselves from environmental stressors in aquaculture ponds, during columnaris outbreaks[231]. Chemical disinfectant options (e.g., chloramines-T, potassium permanganate, copper sulfate, hydrogen peroxide, sodium chloride) are undesirable for the food industry due to possible bioaccumulation and biomagnification[232]. Therefore, alternative disinfection technologies, e.g., UV disinfection, are commonly utilized[233]. UV disinfection becomes ineffective in such cases, where high hardness in water causes scaling and compromises the transparency of the water, that is required for UV to be effective. As discussed in Chapter 1, MW irradiation does not require a clear optical path, thus making this technology attractive for inactivating such pathogens in these conditions.

5.2 EXPERIMENTAL

5.2.1 Materials

Bacillus subtilis subsp. subtilis (ATCC® 6051™), *Legionella pneumophila* (ATCC® 33152 ™), *E. coli* bacteriophage MS2 (ATCC® 15597-B1 ™), *E. coli* host (ATCC® 15597 ™), and *F. columnare* (ATCC® 23463 ™) were obtained from the American Type Culture Collection (Rockville, MD).

Tryptone dehydrated, dextrose anhydrous (glucose), calcium chloride, thiamine, iron (II) sulfate heptahydrate, magnesium chloride, calcium nitrate, potassium chloride, magnesium sulfate, nutrient agar Difco (BD213000), nutrient broth Difco (BD234000), peptone powder, ACES buffer, sodium acetate, sodium chloride, and beef extract were purchased from Fisher Scientific (Houston, TX). Yeast extract, charcoal (Sigma C-5510), L-cysteine hydrochloride, iron (III) pyrophosphate, potassium hydroxide, were obtained from Sigma (St. Louis, MO). Other reagents were purchased from Fisher Scientific (Houston, TX), unless otherwise noted.

5.2.2 Preparation of Bacterial and Viral Strains

Bacterial stocks and working cultures were prepared using the protocol described in Chapter 4. Freeze-dried MS2 phages were recovered by rehydrating them in ATCC 271 Escherichia medium (Appendix E). Phage stocks are kept at 4±1 ºC until ready to assay. Reference cultures of bacteria were rehydrated in specific broth media and acclimatized by incubating them at their specific growth conditions (see Table 5.1). Cryovials were then prepared by adding glycerol to the acclimatized cultures. Standard working cultures for each experiment also were prepared by isolating individual colonies

formed on agar plates. Colonies were then aseptically transferred into fresh growth media, incubated, and transferred to cryovials with cryoprotectant media, and stored at -80 ºC. Other details are presented in Chapter 4.

5.2.3 Inactivation Efficiency

Inactivation experiments followed closely the protocol developed in 4.3.4. Each experiment required the preparation of fresh bacterial cultures, i.e., *B. subtilis*, *L. pneumophila*, *F. columnare*, and *E. coli* host, and a viral suspension, i.e., MS2. The general steps followed for the preparation of bacterial and viral strains and typical growth characteristics of each microorganism are presented in Table 5.1.

Table 5.1: Steps for the preparation of bacterial and viral strains, and their particular culturing conditions.

	B. subtilis	*L. pneumophila*	*F. columnare*	*E. coli* host	MS2 phage
1. Working culture strain	• Previously prepared working culture stored at -80 ºC				Reference stock was rehydrated and phages are kept at 4°C ± 1°C.
	• A vial of working culture is thawed and added to 25 mL fresh prewarmed broth media, specific for each strain.				NA
2. Growth / maintenance media*	Nutrient broth (BD234000)	ATCC 1099 CYE buffered medium	Anacker and Ordal medium	ATCC 271 Escherichia medium	ATCC 271 Escherichia medium
3. Acclimatization	Overnight at 30 ± 2 ºC and 150 rpm	48-72 hr at 37 ± 2 ºC and 150 rpm	72-96 hr at 20°C ± 2 ºC and 150 rpm	Overnight at 37 ± 2 ºC and 150 rpm	NA
4. Inoculation of fresh broth	500 μL of overnight or acclimatized culture are inoculated into 25 mL fresh broth media.				NA
	Cultures are allowed to grow until log-phase is achieved and their optical density is monitored.				NA
	After reaching log-phase, bacterial suspensions are chilled on wet ice to slow replication until ready for use.				NA
5. Resuspension in buffer media	Cells are harvested, separated from growth media by centrifugation at 5000 × g for 15 min, and resuspended in PBS to maintain bacterial permeability after each cycle.			NA	NA
6. Dilutions	Suspensions are diluted accordingly.				NA

NA: not applicable

Identical sets of samples were prepared for each experiment: i) an irradiated set composed of bacteria or MS2 samples with and without NH-1 (1 and/or 10 mg/L final concentration) and ii) an unirradiated set for the same samples. For each experiment, a 1 mL sample was MW irradiated in sterile quartz tube. Samples were then serially diluted (PBS) in 96-well plates, and 10 μL of sample dilutions were pipetted onto agar plates, following the protocol developed in Chapter 3. Each sample was tested in triplicates. Dried plates were incubated following the individual conditions of the different bacterial

* See appendix E for growth media composition.

strains (i.e., temperature and incubation time, see Table 5.1), and viable colonies were enumerated at the end of incubation by plate counts. Inactivation efficiency is presented in terms of logarithmic reduction and is calculated using Eq. 4.6. For phage inactivation, MS2 bacteriophages were quantified by a plaque assay (double agar layer), which is validated by ISO 10705-1[208].

The irradiation protocol is described in details in Chapter 4. Briefly, agar plates of ATCC 271 Escherichia medium were prepared following the recipe shown in Appendix E. Soft agar of the same growth media is also produced, autoclaved, divided into 2.5-mL sterile tubes, and kept in a water bath at 45-48°C. After a fresh bacterial host batch is ready, i.e., has reached mid-exponential phase (Table 5.1), a small volume (50 μL) is inoculated into each of the tubes of molten soft agar and kept in the hot water bath. The solution is gently mixed, to avoid introducing bubbles to the agar, and is rapidly added on top of the agar plates, where it is spread by inclining the plate and allowed to solidify. At the same time, a set of samples is irradiated with MW energy, while another identical set is kept away from direct light exposure. Samples are then serially diluted (PBS) at six different dilutions and pipetted onto soft agar plates. For each dilution, agar is punctured to leave a reference point where MS2 was injected. Dried plates are incubated at 37±2 ºC for 16 to 24 h, and circular zones of clearing (typically 1 mm diameter) in lawn of host bacteria are enumerated. Inactivated bacteriophages do not infect and multiply in the bacterial host, and thus, no clearings are obtained. Resulting plaques are reported in plaque-forming units (PFU/mL)_for MS2. Inactivation efficiency is presented in terms of logarithmic reduction as calculated by Eq. 4.6.

For *B. subtilis* studies, sporulation was carried out in 2X SG medium (Appendix E), and spores were allowed to form while incubating after 7 days at 30±2 ºC and 150 rpm. Following incubation, *B. subtilis* spores were isolated and washed as previously described. A heat shock treatment at 65 ºC for 30 min is performed to the freshly harvested cells, in order to inactivate any remaining vegetative cells. This heat treatment has no effect on the viability of spores.

5.3 RESULTS AND DISCUSSION

5.3.1 *B. subtilis* inactivation

Baseline experiments were performed with *B. subtilis* spores exposed to NH-1 (1 mg/L final concentration) and irradiated for 20 s at 70 W input power at 2450 MHz irradiation (results not shown). Preliminary data did not result in successful inactivation of the bacterial spores. Thus, a longer irradiation regime (60 s, 3X 30s, and 9X 30s) combined with an increase of the NH-1 concentration (10 mg/L final concentration) was selected. Figure 5.1 shows that no significant inactivation of *B. subtilis* spores is achieved until irradiation was applied for 270 s. When the concentration of NH-1 is increased to 10 mg/L, irradiation produced a minor increase in log reduction (0.38±0.17) compared to the 1 mg/L concentration. These results are encouraging but still not satisfactory if compared to other technologies. However, results are consistent with studies that use combined UV/H_2O_2 advanced oxidation[234], where H_2O_2 and UV/H_2O_2 combined treatment did not show any inactivation of *B. subtilis* spores. In another study, OH radicals seemed to play a minor role in the inactivation of the spores and ozone is presented as the most efficient chemical disinfectant available to inactivate them[235]. However, a proper inactivation of

the more resistant *C. parvum* oocysts with ozone, might generate harmful concentrations of DBPs because of the high doses and contact times required[235]. Thus, an altered design of the NHs, for these spores, capable of producing higher concentration of ROS is desired.

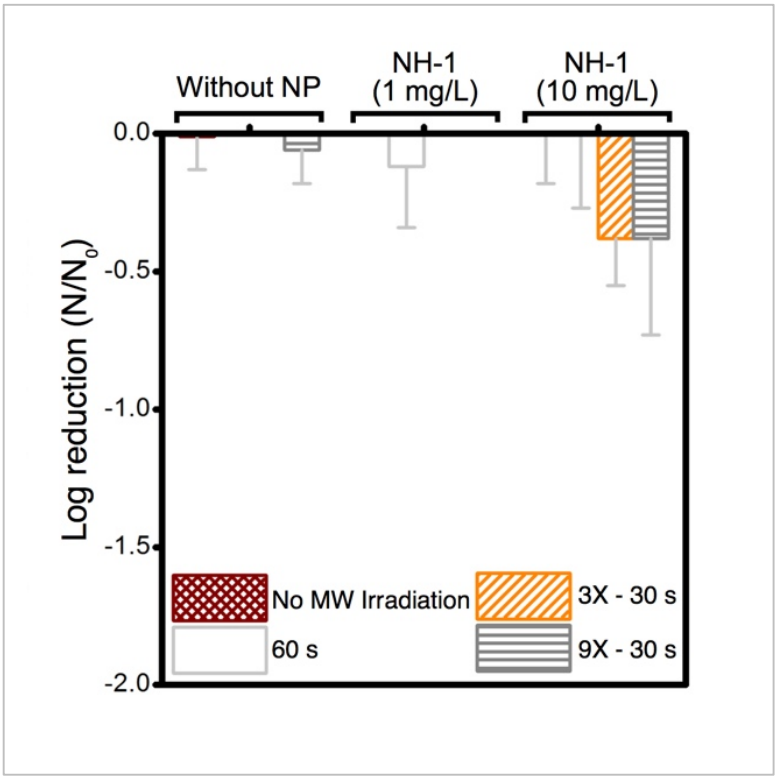

Figure 5.1: Inactivation of *B. subtilis* exposed to NH-1, and appropriate controls. Material concentration utilized in all experiments was varied at 1 and 10 mg/L. Initial concentration of *B. subtilis* ~10^7 CFU/mL. LOD is 100 CFU/mL. Error bars represent one standard deviation measured from experimental triplicates.

5.3.2 *L. pneumophila* inactivation

Baseline experiments where ~2×10^4 CFU/mL cells were irradiated for 20 s at 70 W at 2450 MHz (results not shown), did not result in significant differences between controls and bacteria exposed to NH-1 (1 mg/L). For extended irradiation conditions (70 W at 2450 MHz for 60, 180, and 360 s), the temperature of the sample was controlled between irradiations cycles (with a cold water bath) to minimize convolution of inactivation mechanisms. Figure 5.2 shows that irradiation time plays a significant role in inactivation for NHs used at 1 mg/L concentration. Increasing the NH concentration to 10 mg/L did not improve the log removal and also showed less sensitivity to higher irradiation time. The highest inactivation was observed for 1 mg/L NH concentration irradiated 360 s (1.17 ± 0.17 log reduction).

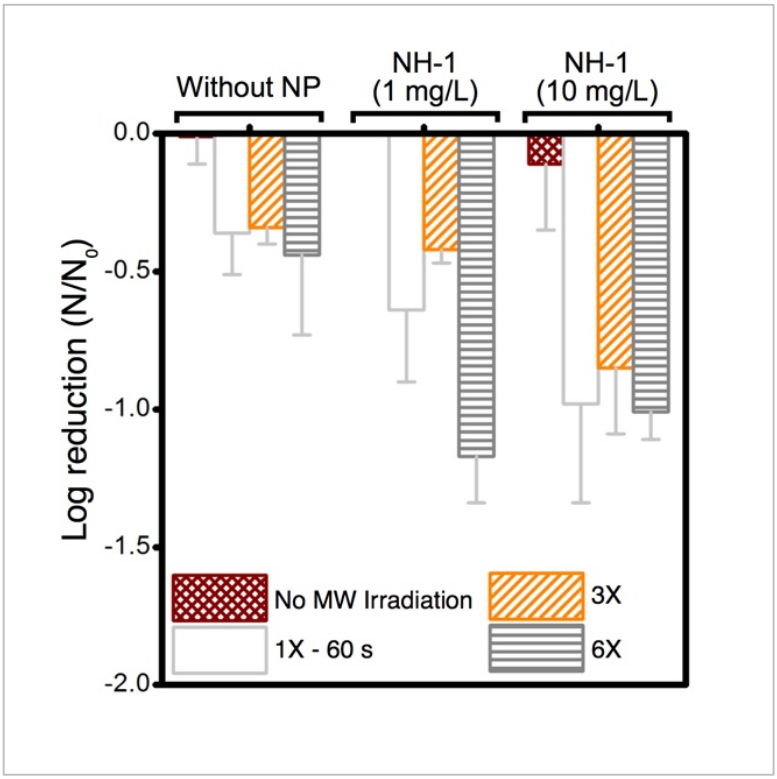

Figure 5.2: Inactivation of *L. pneumophila* exposed to NH-1 and appropriate controls. 1 and 10 mg/L NH concentration was utilized up to three cycles of irradiation. Initial concentration of *L. pneumophila* ~2×10^4 CFU/mL. LOD is 100 CFU/mL. Error bars represent one standard deviation measured from experimental triplicates.

Results obtained are comparable to the those for *P. aeruginosa* discussed in Chapter 4. Our results are in agreement with other literature findings using photocatalytic materials and UV radiation[236]. Inactivation of *L. pneumophila* by photocatalytic oxidation results in effective disintegration of the cytoplasmic membrane of cells due to ROS formation and inactivation of bacterial strains [219]. Additionally, *L. pneumophila* has exhibited sensitivity to relatively low levels of H_2O_2[220], making this bacteria especially

susceptible to this technology. Improvement in material composition could enhance log removal of this important waterborne microorganism.

5.3.3 *F. columnare* inactivation

An initial concentration of ~2×10^8 CFU/mL was exposed to NH-1 and an identical sample was irradiated with MW power for 60 s (70 W and 2450 MHz). Irradiation of NH-1 for 60 s resulted in 4.13±0.7 log reduction, while its irradiated control (bacteria without NPs) resulted in 2.22±0.06 log reduction. Clearly, temperature is important in inactivating *F. columnare*, but the treatment with MW irradiation in the presence of NH-1 resulted in two-orders of magnitude higher reduction. Similar irradiation-based technologies, i.e., photocatalytic irradiation, are able to obtain more than 5-log and 2-log reduction upon 30 min of irradiation, with initial cell concentrations of 10^8-10^9 CFU/mL and 10^4-10^6 CFU/mL, respectively[237]. Additionally, hardness and pH also have been shown to play important role in the photocatalytic inactivation process[237]. Clearly, this MW irradiation technology provides an economic/energetic advantage over the existing radiation based disinfection technologies with comparable removal efficiency. These preliminary results are not only promising but could be a new way of disinfecting aquaculture ponds with an innovative irradiation technology that do not pose the same risks as the chemical-based disinfectants used conventionally[229,232].

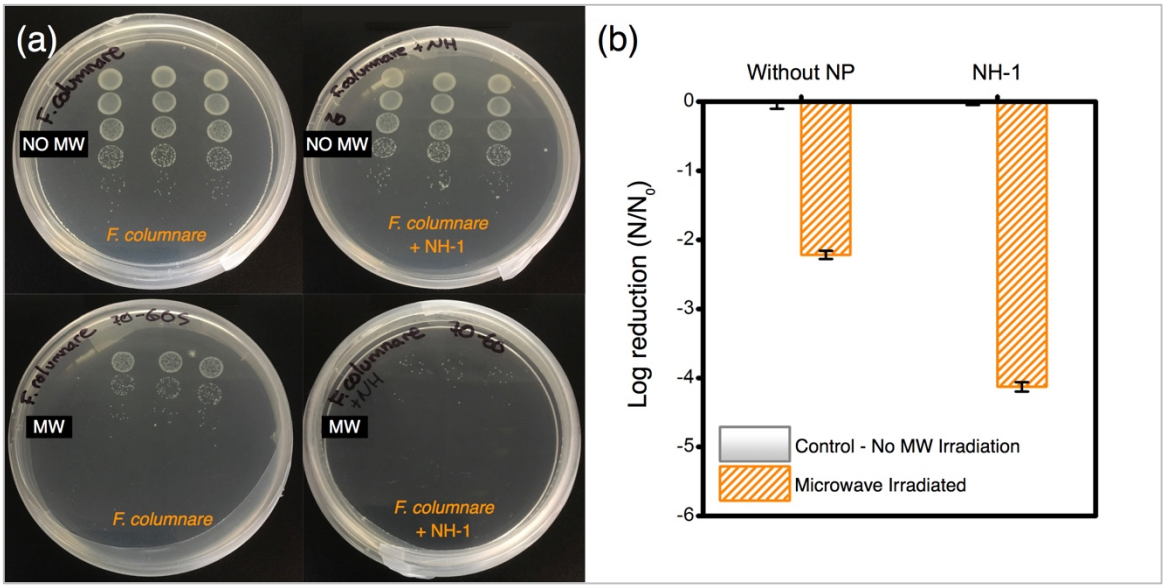

Figure 5.3: (a) Colonies of *F. columnare* grown in Anacker and Ordal agar and (b) inactivation of *F. columnare* exposed to NH-1. 1 and 10 mg/L NH concentration was utilized up to three cycles of irradiation. Initial concentration of *F. columnare* ~2×10^8 CFU/mL. LOD is 100 CFU/mL. Error bars represent one standard deviation measured from experimental triplicates.

5.3.4 MS2 inactivation

Baseline experiments are performed with ~6×10^8 PFU/mL MS2 exposed to 1 mg/L NH and irradiated for 20 s at 70 W power at 2450 MHz (results not shown). Preliminary data did not result in successful inactivation of the MS2, and hence, a longer irradiation cycle (i.e., 180 and 360 s) and increased NH concentration (10 mg/L final concentration) are utilized.

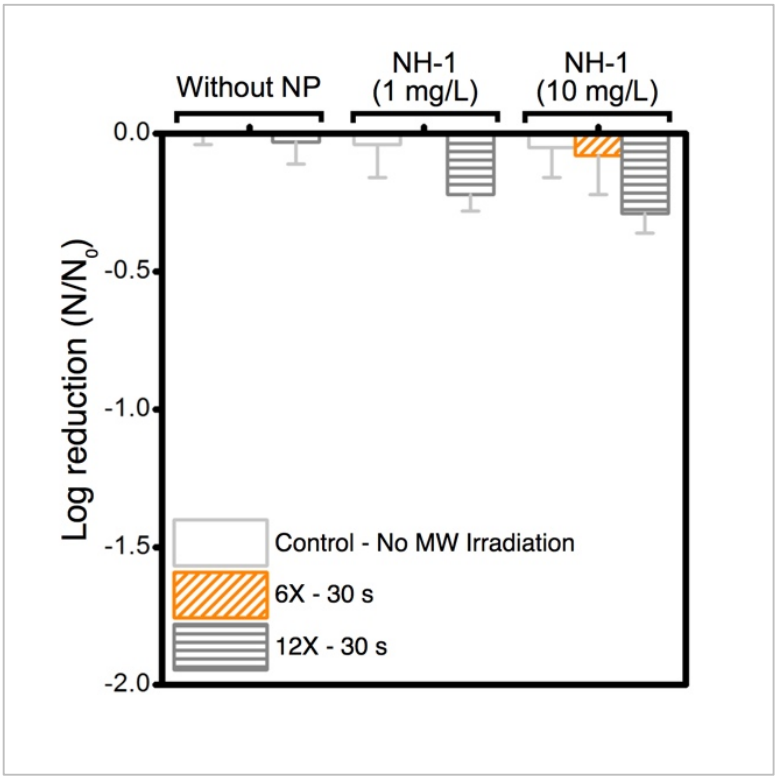

Figure 5.4: Inactivation of MS2 bacteriophage exposed to NH-1 and appropriate controls. 1 and 10 mg/L NH concentration was utilized up to three cycles of irradiation. Initial concentration of MS2 ~6×10^{8} PFU/mL. LOD is 50 PFU/mL. Error bars represent one standard deviation measured from experimental triplicates.

Figure 5.4 shows that at least 360 s irradiation is required to achieve any noticeable inactivation of MS2. Increase in the concentration of the NHs did not enhance MS2 inactivation, substantially. The highest inactivation achieved was 0.29±0.078 log with the higher NH concentration and at maximum irradiation time. Evidence shows that MS2 phages when exposed directly to a high dose of H_2O_2 (150 mg/L), are only inactivated up to 0.2 log [211]. However, other studies have shown that OH· might enhance inactivation efficacy of MS2 by causing damage to the viral capsid, and facilitating

diffusion of other types of ROSs into the virions[238]. Thus ROS produced by this specific NH might not be sufficient to achieve adequate inactivation but enhanced material design might lead to improved inactivation.

5.3.5 Key Findings

This chapter assessed the efficacy of the designed NHs to inactivate a wide range of surrogates of pathogenic bacteria, viruses, and protozoa. Different degrees of inactivation were obtained for different species studied. *B. subtilis* spores showed no significant inactivation after these were irradiated for 270 s. Increasing material concentration (from 1 to 10 mg/L) produced a minor increase in the removal of viable colonies. For *L. pneumophila*, results are more in agreement with those obtained with *P. aeruginosa* (in Chapter 3 and 4). However, 1.17 log reduction is only achieved after 360 s of irradiation. Significant removal of the aquaculture-relevant microorganism *F. columnare* (~4 log reduction) has been achieved, which shows promise for this technology to those microorganisms that are sensitive to ROS. These results are promising and indicate that a better material design is necessary to elevate this to a disinfection technology.

Chapter 6: Conclusions and Recommendations

In this dissertation, the design, synthesis, characterization, and efficacy of a new NH that can harness the power of MW to inactivate a wide range of pathogens has been presented. This is the first report to-date where MW irradiation utilized over a short duration was successful in inactivating a variety of waterborne pathogens. Though the results obtained show promise, significant improvement in bacterial and viral log removal is necessary to elevate this technology as an effective disinfection process for point-of-use applications. The key findings from this dissertation and recommendations for future work are discussed in this chapter.

Objective 1 (Chapter 2). Perform a detailed literature review to better understanding the multifunctional properties of NHs.

A comprehensive review was performed on stimuli-responsive materials, to better understand synergy between multiple nano-scale entities. During this review, it was found that when MWNTs are hybridized with metal oxides, the resulting hybrids exhibit excellent absorption properties in visible light region and thus can be engineered to extract useful photocatalytic properties [38,84]. From this review, a NH based on MWNT and lanthanide series components, that can absorb electromagnetic (EM) radiation and subsequently produce ROS, was found to be a potential candidate for inactivation of bacteria. EM stimulation in the form of MW radiation was of particular interest since MW applications have spread in all economies worldwide, and the MW market continues to grow[16]. Further, MW radiation constitutes an affordable technology that can be

adopted for unintended uses, such as disinfection, making it a versatile technology with potential applications at both centralized or point-of use scales.

Objective 2 (Chapter 3). Design, synthesize, and characterize a novel NH, capable of MW spectral conversion for inactivation of *P. aeruginosa*.

Successful hybridization of MWNT-Er_2O_3 NH with a wide range of metal oxide has been achieved utilizing a modified sol gel process developed in a parallel dissertation work[34]. The design of these materials was independently done and the sol-gel method was utilized with a unique objective of utilizing the MW absorption capabilities of MWNTs and spectral conversion abilities of lanthanide series metals. Characterization of the materials showed metal/metal oxide crystalline features that were chemically bound to MWNTs. Control over synthesis with loading and distribution uniformity of erbium oxide on MWNTs is demonstrated via STEM images, elemental mapping, and elemental composition using STEM, XPS, XRD, and TGA characterization techniques.

Inactivation potency of the NHs has been achieved upon irradiating *P. aeruginosa* with MW in the presence of NHs. The results show the first evidence of nano-scale heterostructures that can harness MW radiation to produce ROS and subsequently inactivate a waterborne microorganism. The energy footprint for achieving these results is also low (0.0006 kW·h) and hence demonstrates promise of this technology to be used as a point-of-use treatment solution in a practical and affordable way.

Objective 3 (Chapter 4). Exploring the roles of MW wavelength and irradiation time on inactivation effectiveness of *P. aeruginosa* in an effort to unlock the energetic balance in the disinfection system.

With an objective to better understand the role of irradiation parameters (i.e., irradiation time, radiation frequency, and input power) on inactivation, a MW radiation device has been designed and constructed. The efficiency of the reactor design was tested with *P. aeruginosa* inactivation.

This constitutes the first development of a reactor with appropriate control of MW radiation for samples of bacteria exposed to NHs. The setup includes a MW power generator and a copper waveguide that has been designed exclusively for this purpose. The initial studies show that the reactor transmitted MW radiation as expected (via temperature measurements) and that bacterial inactivation studies can be performed using such a setup, controlling the necessary parameters. The design and start up experiments served as a methodical approach to inactivation of waterborne pathogens.

Inactivation of *P. aeruginosa* was achieved while varying wavelength, MW input power, and MW irradiation time. Exposing samples to a higher energy, results in a slight increase in bacterial inactivation. However, the maximum inactivation achieved at any condition did not exceeded 1.25 log units regardless of irradiation frequency, input power, or irradiation exposure. The inactivation achieved is still not adequate for this technology to be used for water disinfection. However, future studies should concentrate on redesign of the NH material for improved inactivation. Results in this chapter serve to

further confirm that NHs are able to harness MW irradiation for inactivation of waterborne microorganisms at an even lower MW input power (60 W).

Objective 4 (Chapter 5). Determine the inactivation efficacy of the MW spectral conversion NHs for a wide range of waterborne microorganisms.

With the goal of determining efficacy of the MW-enabled NH technology at inactivating a wide range of waterborne pathogens of environmental relevance, four species, of both pathogenic and surrogate microorganisms, were examined. Samples were irradiated using the frequency of conventional MW appliances (2450 MHz) at the maximum input power that the generator can allow for the design of the waveguide (70 W).

Baseline inactivation experiments served to establish working protocols for each microorganism and their resistance to inactivation. Irradiation times were adjusted individually, and samples were irradiated in cycles to minimize interference between inactivation mechanisms. Distinctive amounts of inactivation were obtained for each microorganism:

- *B. subtilis* spores showed no significant inactivation after irradiation for 270 s. Increasing material concentration (from 1 to 10 mg/L) produced a minor increase in the removal of viable spores.

- *L. pneumophila*, results are more in agreement with results obtained with *P. aeruginosa*. However, 1.2-log reduction was only achieved after 360 s of irradiation in 60 s cycles.
- *F. columnare strains* resulted in an important accomplishment after obtaining ~4 log reduction of viable counts after only 60 s irradiation. This result is an important finding for the aquaculture industry in need of new disinfection methods to prevent the accumulation of chemical byproducts in the food chain.
- Insubstantial inactivation of MS2 viruses was observed.

Future Work

Though this dissertation presents one of the first evidences that successfully utilized MW (one of the lowest energy radiation) to inactivate, i.e., reduce viable plate counts, waterborne microorganisms, there is substantial room for improvement. The inactivation achieved by the combination of the NH material and the MW power generation and irradiation setup did not achieve the levels of inactivation needed for reliable disinfection. Improved material design to better harness MW radiation and subsequently produce increased amount of ROS to inactive waterborne pathogens is necessary. Furthermore, device engineering utilizing the NHs also is desired for practical use of this technology as a point-of-use treatment solution.

Future work can focus on the following key areas:

- Redesign of NHs with a lower loading of Er_2O_3, which might enable improved absorption of MW radiation and thus will likely facilitate ROS production.

- Identify the most adequate loading/absorption of MW radiation ratio for the MWNT-Erbium NH or new materials.
- Systematically assessing the role of surface charge of the microorganisms and the state of aggregation of the NHs on production of ROS and subsequent pathogenic inactivation is necessitated.
- Evaluate responses of microorganisms to H_2O_2 disinfection processes with different qualities of water and NOM content, for any possible blocking effects.
- Consider designing a NH where local heating of the material with highly heat conductive metals (like Ag) as well as ion donation (e.g., from Ag nanoparticles) can provide multi-pronged attack to better inactivate pathogens.
- Developing new protocols to rapidly assess the inactivation efficiency of the system.
- Obtaining and improving techniques for measuring ROS. ROS probes are expensive and their preparation is complex. Spin-trapping for small concentrations of nanomaterials is challenging.
- Optimizing NH and/or bacterial concentration for achieving higher removal.
- Further experimental investigations are needed to estimate the energetic balance of the system. As the optimal efficiency in the present study is not satisfactory for practical application, more efficient NHs and waveguide designs can now be implemented and tested with this development.

Potentiostats can elaborate on current produced while infra-red cameras can be used to assess local heating of the samples.

- Redesigned NHs should be immobilized on a surface for enabling practical use of these materials. Ceramic membranes can be used as an option for such immobilization and testing. Later, ceramic vessels lined with the NHs can be designed and used as point-of-use devices.
- Water quality can influence the efficiency and performance of the MW inactivation process. The role of natural organic matter (which can serve as scavengers of ROS) and turbidity should be studied
- The safety of these materials needs to be assessed for this technology to be commercialized. Also, possible chemical by-product formation by unintended reactions of ROS with synthetic or natural organic molecules needs to be evaluated.

Appendices

APPENDIX A – TABLES

Table A.1: Loading ratios of the 3 NHs.

No.	Name	Amount of MWNTs (mg)	Amount of salt* (mg)	Molar Ratio ($C:Er^{3+}$)
1	NH-1	50	115	16.04:1
2	NH-2	50	230	8.02:1
3	NH-3	50	460	4.01:1

* Erbium salt: $Er(NO_3)_3 \cdot 5H_2O$

Table A.2: EDX elemental composition of the NHs synthesized.

Element	**Weight %***		
	NH-1	**NH-2**	**NH-3**
Carbon	41.36	23.82	7.47
Erbium	47.91	64.12	80.11
Oxygen	10.73	12.06	12.41
Relative Ratios $C:Er^{3+}$	0.86	0.37	0.09

*Weight % calculated as the atomic percentage times molecular weight divided by the total sum of elements detected.

Table A.3: Summary of XPS data and weight percentage of elements.

XPS Region	**Weight %***		
	NH-1	**NH-2**	**NH-3**
C 1s	49.08	35.71	12.90
Er 4d	38.16	49.35	69.13
O 1s	12.76	14.94	17.97
Relative Ratios $C:Er^{3+}$	1.29	0.72	0.19

*Weight % calculated as the atomic percentage times molecular weight divided by the total sum of elements detected.

Table A.4: Temperature increase after 20 s MW irradiation time at 10% power (0.0006 kW·h).

	Initial Temperature, ºC	Final Temperature, ºC	Delta Temp, ºC
DI	22.10	23.27	1.17±0.12
MWNT	23.23	24.03	0.80±0.10
Salt*	23.27	24.37	1.10±0.17
NH-1	23.40	25.50	2.10±0.30
NH-2	23.67	24.87	1.20±0.17
NH-3	23.33	24.37	1.03±0.06

* Erbium salt: $Er(NO_3)_3 \cdot 5H_2O$

APPENDIX B – FIGURES

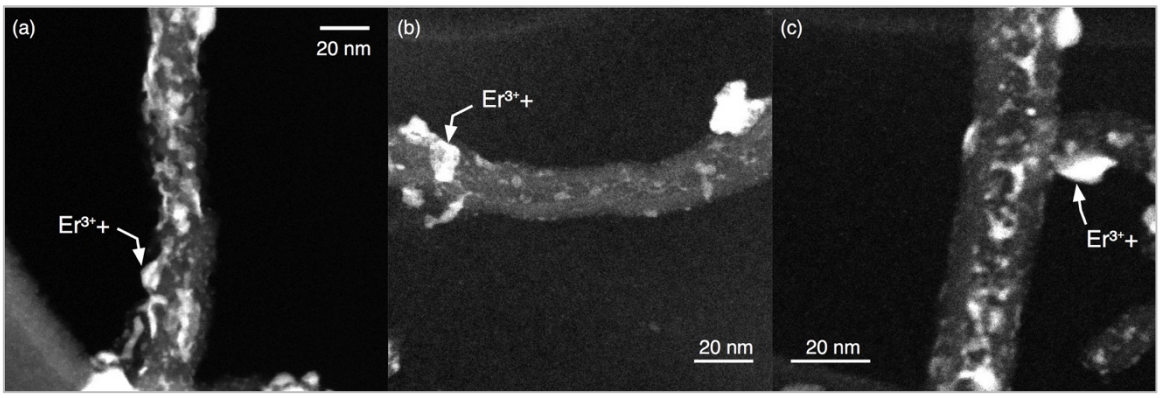

Figure A.1: STEM HAADF images of a representative ion-beam irradiated samples of NH-1.

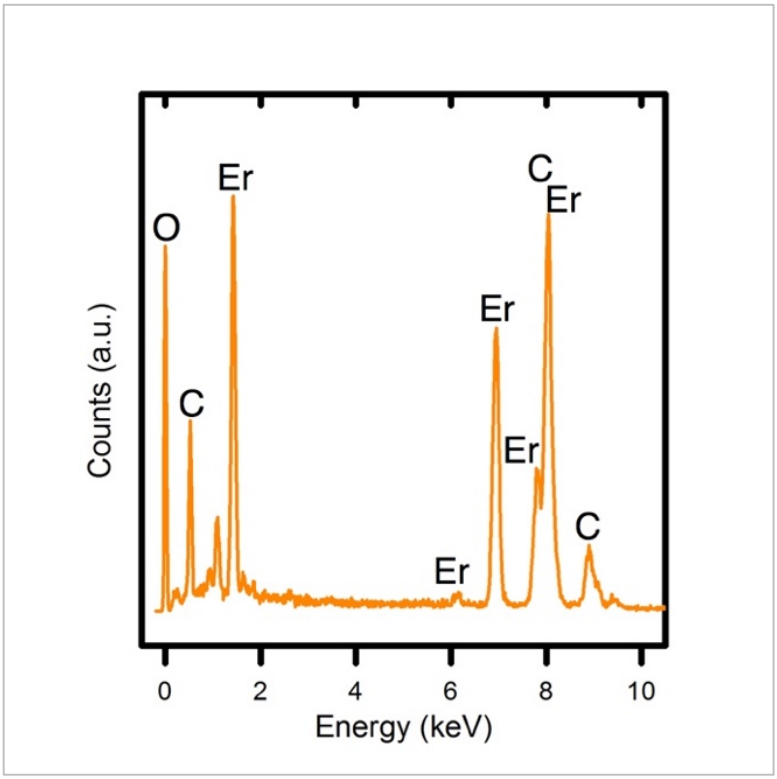

Figure A.2: EDX spectrum of representative NH-1. Erbium, carbon, and oxygen elements are all identifiable.

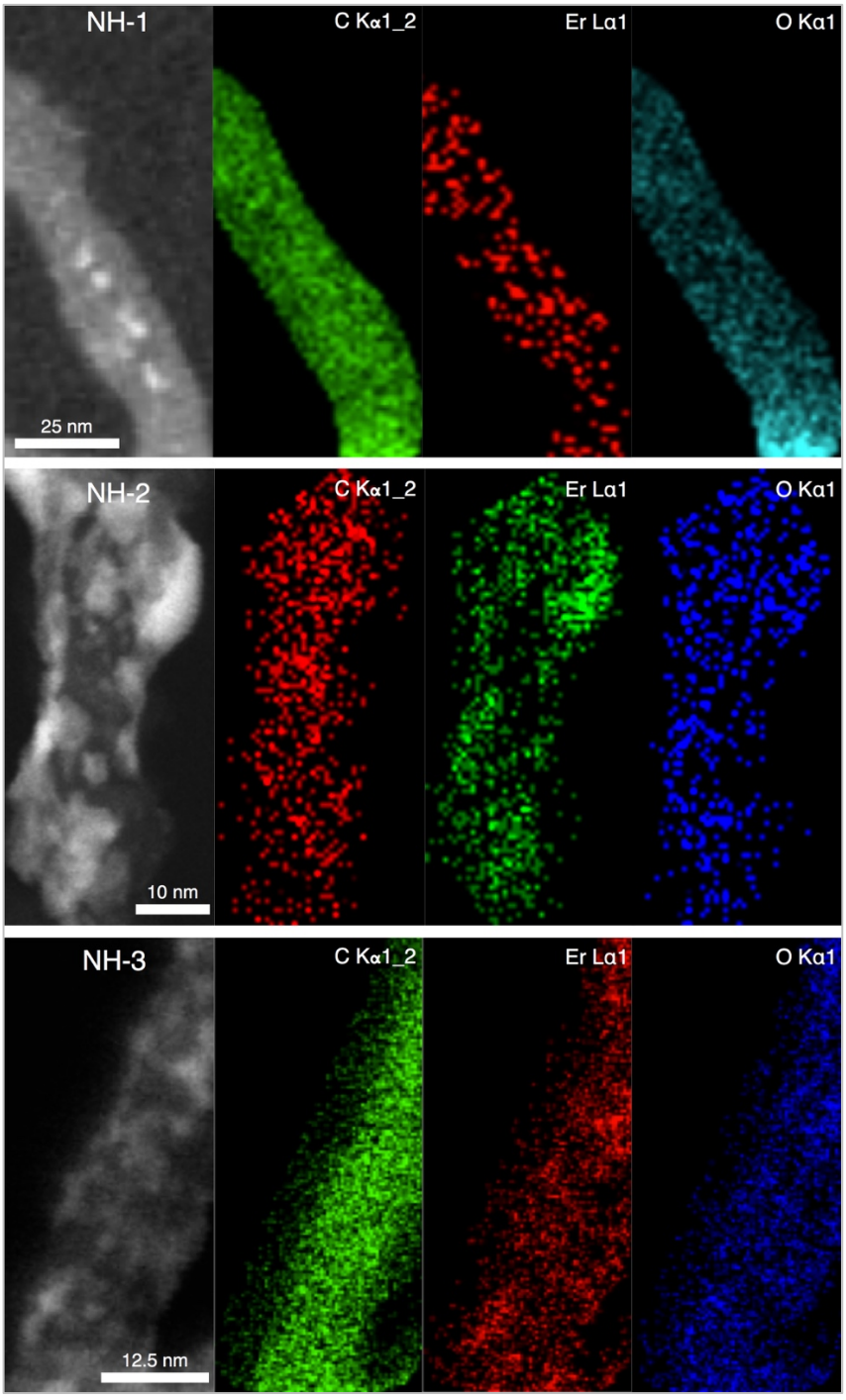

Figure A.3: STEM images and elemental mapping of the NHs synthesized.

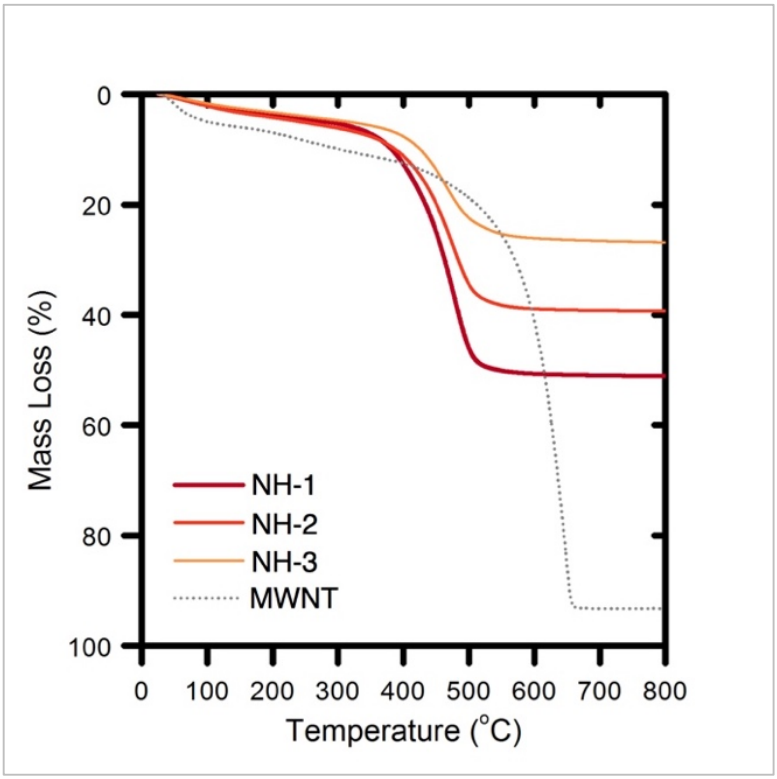

Figure A.4: TGA analyses of representative functionalized MWNT and NH samples. Temperatures of oxidation for the NHs are 475 ºC (NH-1), 474 ºC (NH-2), and 467 ºC (NH-3) respectively.

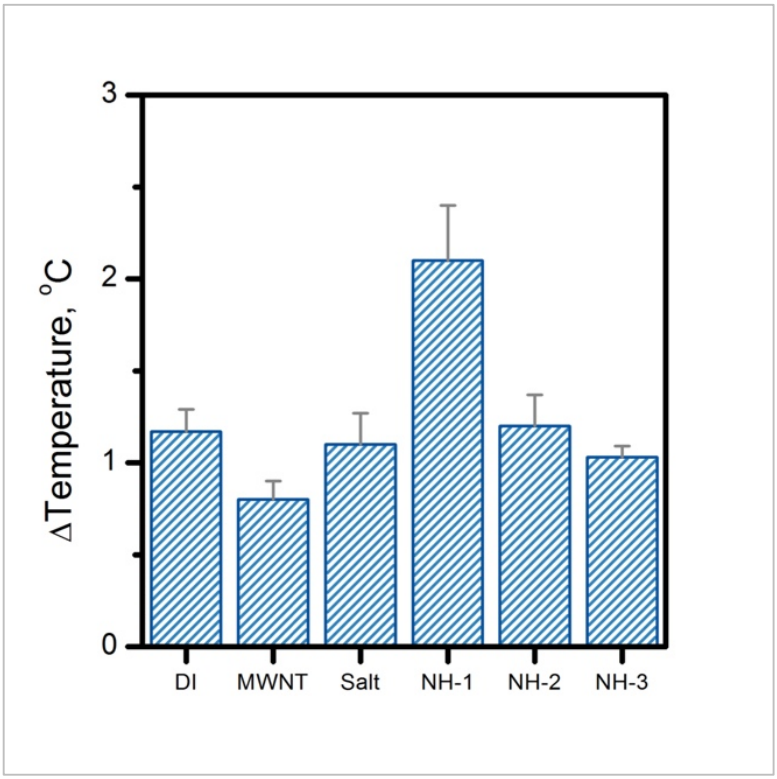

Figure A.5: Temperature differences between irradiated and microwave radiated samples. Differences are presented from room temperature (21 ºC).

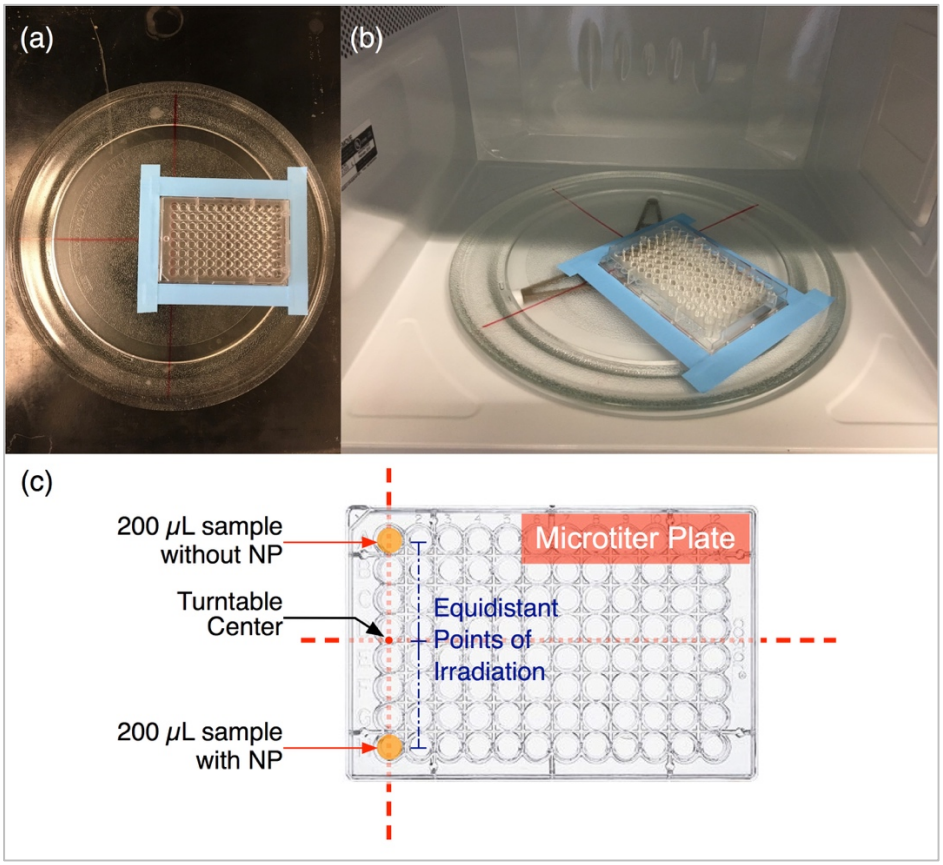

Figure A.6: Irradiation setup for the MW oven. (a) Top view of the microtiter plate positioned on the turntable. (b) Microtiter plate as the samples are ready to be irradiated in the MW cavity. (c) Sample location at the microtiter plate (top view).

APPENDIX C – ROS GENERATION

Oxidative stress is one of the key mechanisms causing antimicrobiality when nanoparticles interact with bacteria[239]. Such stresses are caused by an imbalance between damaging oxidants (e.g., H_2O_2 and $OH^{\bullet}$) and protective antioxidants (e.g., vitamin C and glutathione)[239] within a nano-bio system. Studies have shown ROS generation from surfaces of metal oxide nanocrystals[240,241]. Oxygen can be activated to form ROS by both energy transfer and electron transfer processes. The former leads to the formation of singlet oxygen ($^1O_2$), while the latter results in the generation of superoxide ($O_2^{\bullet-}$), which undergoes further chemical transformation in water.

When illuminated, metal oxides such as ZnO[242] and TiO_2[179], cause charge separation, generating a hole (h^+) in the valence band (E_V) and an electron (e^-) in the conduction band (E_C) (Table A.5). Holes extract electrons from water and/or hydroxyl ions, generating $OH^{\bullet}$. Electrons reduce O_2 producing $O_2^{\bullet-}$ and other ROS in a cascade of consecutive reactions (Table A.5).

Studies have shown that $^1O_2$ can be generated indirectly from metal oxide nanoparticles via the oxidation of $O_2^{\bullet-}$[243,244] and when sufficient energy capable of reversing the spin on one of the unpaired electrons of O_2 is absorbed, primarily through an energy transfer process[245]. Carbon-based photosensitizers (i.e. C_{60} fullerenes) have been shown to absorb UV or visible electromagnetic radiation and transfer it to surrounding molecules, and thereby facilitate energy or electron transfer that lead to the formation of $^1O_2$ or $O_2^{\bullet-}$, respectively[246]. In particular, MWNTs can accept electrons and

aid in ballistic transport along MWNT[25] axes, making these carbon structures excellent candidates to scatter electrons with enhanced surface area.

Table A.5: ROS generating reactions[247].

$metal\ oxide + light \rightarrow h^+ + e^-$
$H_2O + h^+ \rightarrow OH^\bullet + H^+; \quad OH^\bullet + H^+ + e^- \rightarrow H_2O$
$O_2 + e^- \rightarrow O_2^{\bullet -}$
$O_2^{\bullet -} + H^+ \rightarrow HO_2^\bullet$
$O_2^{\bullet -} + H^+ + e^- \rightarrow H_2O_2$
$2HO_2^\bullet \rightarrow H_2O_2 + O_2$
$O_2 + 2H^+ + 2e^- \rightarrow H_2O_2$
$H_2O_2 + O_2^{\bullet -} \rightarrow OH^\bullet + O_2 + OH^-$
$H_2O_2 + e^- + H^+ \rightarrow H_2O + OH^\bullet$

APPENDIX D – ELECTRONIC STRUCTURE OF METAL OXIDES

The band architecture of semiconductors can be used to understand the ROS generation mechanisms when comparing with redox potentials (E_H) of different ROS. The electronic structure of semiconductors is characterized by the band-gap (E_G), which is essentially an energy difference between the valence (E_V) and conduction (E_C) bands. Values of E_G for metal oxides are dependent on the growth method, crystal structure, and defects. Different values of E_G for TiO_2 (2.9-3.3 eV), SiO_2 (8-11 eV), ZnO (3.20-3.44 eV), and lanthanide series Er_2O_3 (1.4-3.26 eV) have been reported[248]. When E_G is small (0-4 eV) the material is considered to be a semiconductor; whereas for materials with higher E_G values (e.g., 4-12 eV) are considered as insulators[248]. Although E_G is reported extensively for different materials, there is a critical need for accurate measurements and/or theoretical estimations for the E_G and the band structure of most semiconductors. Furthermore, E_V and E_C values are often presented in ways that prevent a straight-forward comparison to the redox potentials of aqueous electrolytes. For instance, in materials science the band energy positions are expressed with respect to the Fermi level of the material, rather than to the absolute vacuum scale (AVS). On the other hand, geochemical and electrochemical literature reports standard redox potentials for aqueous redox couples and with respect to the normal hydrogen electrode (NHE)[249].

In the context of electron transfer between semiconductors and aqueous redox species, it is crucial to identify the highest occupied molecular orbital (HOMO) and the lowest unoccupied molecular orbital (LUMO) in the semiconductor because those are the energy levels involved in the transfer. In most semiconductors, the energy states in the E_V are completely occupied whereas those in the E_C are empty. The Fermi level (E_F)

represents the chemical potential of electrons in a semiconductor and can be considered as the absolute electronegativity ($-\chi$) of a pristine semiconductor. The relationships between band edge energies (i.e., the bottom of E_C and the top of E_V) and electronegativity are shown in Eqs. A.1 and A.2[249].

$$E_C = -\chi + 0.5E_G \qquad \textbf{Eq. A.1}$$

$$E_V = -\chi - 0.5E_G \qquad \textbf{Eq. A.2}$$

Solution chemistry affects band edges, shifting them to higher or lower energy levels following a linear relation with respect to the solution's pH, according to the Nernstian relation (Eqs. A.3 and A.4)[250].

$$E_C = -\chi + 0.5E_G + 0.059(PZZP - pH) \qquad \textbf{Eq. A.3}$$

$$E_V = -\chi - 0.5E_G + 0.059(PZZP - pH) \qquad \textbf{Eq. A.4}$$

Where, PZZP is the point of zero zeta potential of the bulk oxide.

Thus, the values of conduction and valence band energies can be estimated using these set of equations. In Table S6, we present a comparison of the calculated values of band edge energies for TiO_2, SiO_2, ZnO, and Er_2O_3 at neutral pH for values of PZZP, electronegativities, and band gap energies found in the literature.

Table A.6: Calculated band edge energies of semiconductors at absolute vacuum scale (AVS) and normal hydrogen electrode (NHE).

Metal Oxide	PZZP	χ (eV)	E_G (eV)[d]	E_C (eV) AVS	E_V (eV) AVS	E_C (eV) NHE	E_V (eV) NHE
SiO_2	2[a]	6.46[a]	8, 10.4, 11	- 1.86±0.79	11.66±0.79	- 2.65±0.79	7.16±0.79
ZnO	8.8[a]	5.75[a]	3.26, 3.35, 3.44	- 3.97±0.04	-7.32±0.04	- 0.53±0.04	2.82±0.04
TiO_2	5.8[a]	5.83[a]	2.9, 3.3, 3.75	- 4.24±0.21	-7.56±0.21	- 0.26±0.98	3.06±0.21
Er_2O_3	8.8[b]	2.96[c]	1.4, 3.26, 5.3[c]	- 0.19±0.98	-4.51±0.98	- 3.31±0.98	0.01±0.98

Values found in literature: [a250], [b251], [c252], [d248]. The energy positions of band edges in the electrochemical scale can be converted as: $E_{(NHE)} = -E_{(AVS)} - 4.5$.

In nanoparticle-mediated photocatalysis, ROS generation is dictated by an interfacial electron transfer processes. Only metal-oxide NPs with E_G less than the incident photon energy (e.g., 3.1 eV [400 nm UV] and 12.4 eV [100 nm UV]) can be photo-excited[253]. Thus, TiO_2 and Er_2O_3 with E_G values as reported in Table S6 could potentially be photo-excited by 365 nm UV light (3.4 eV), while ZnO and SiO_2 will not. The photo-excited electrons and holes can then react with an aqueous electron acceptor (i.e., molecular oxygen) and/or donor (i.e., water and hydroxyl ions), respectively to produce different ROS.

To determine if ROS generation reactions are thermodynamically favorable, one can align the calculated values of E_V and E_C from Table S6 and E_H values reported in Table S7. Such comparison shows evidence that the $O_2^{\bullet-}$ generation potentials from excited electrons donated from SiO_2, ZnO, TiO_2, and Er_2O_3 with E_C values of -2.65±0.79 eV, -0.53±0.04 eV, -0.26±0.98 eV and -3.31±0.98 eV, respectively are less than the value

of E_H for the $O_2/O_2^{\bullet-}$ couple (-0.33 eV). Values of E_C for TiO_2 is greater than the E_H of $O_2/O_2^{\bullet-}$ (-0.33 eV); which indicates that at this pH, its reducing ability is insufficient to reduce O_2. For other species such as H_2O_2 generation, theoretical estimation shows that metal oxides with E_V values larger than E_H value of 0.94-1.06 eV at pH 7 with respect to NHE can produce this ROS. Thus, SiO_2 (7.16±0.79 eV), ZnO (2.82±0.04 eV), TiO_2 (3.06±0.21 eV), and Er_2O_3 (0.01±0.98 eV) can possibly generate H_2O_2. Similarly, $OH^{\bullet}$ generation might also be theoretically achieved by metal oxides with E_V values larger than E_H 2.2 eV at pH 7 with respect to NHE. Thus, SiO_2, ZnO, and TiO_2, might theoretically oxidize H_2O into $OH^{\bullet}$, while Er_2O_3 would not.

Table A.7. Standard one-electron reduction potentials (E_H) of ROS at pH 7 with respect to NHE.

Couple*	E_H (eV)
$OH^{\bullet}, H^+/H_2O$	2.31
$HOO^{\bullet}, H^+/H_2O_2$	1.06
$O_2^{\bullet-}, 2H^+/H_2O_2$	0.94
$O_2(\,^1\Delta g)/O_2^{\bullet-}$	0.65
$H_2O_2, H^+/H_2O, OH^{\bullet}$	0.32
$O_2/O_2^{\bullet-}$	-0.33
$O_2, H^+/HO_2^{\bullet}$	-0.46
H_2O/e_{aq}^-	-2.87

*Listed in order from highly oxidizing to highly reducing[247].

APPENDIX E – GROWTH MEDIA FORMULATIONS

Anacker and Ordal medium

Ingredient	Amount (g/L)
Tryptone	0.5
Yeast extract	0.5
Sodium acetate	0.2
Beef extract	0.2
DI water	1.0

Adjust medium for final pH 7.3 ± 0.1. Autoclave at 121 ºC for 15 minutes. For solid medium, add 10 g of agar to above medium.

ATCC Medium: 1099 CYE Buffered Medium

Base Medium

Ingredient	Amount (g/L)
Yeast Extract	10.0
Charcoal (Sigma C-5510)	2.0
ACES Buffer	10.0
DI Water	0.980

Adjust pH to 6.90 ± 0.05 using KOH (pH is critical). Autoclave at 121 ºC. Cool to 50 ºC. Aseptically add Solutions A and B (see below). Recheck pH and adjust if necessary. Allow sample to cool to room temperature before reading pH. Keep charcoal in suspension when dispensing. For solid medium, add 17 grams of agar to above base medium.

**Note: Medium should be wrapped in foil to protect from light.

**Note: Be sure to allow solid products adequate time to dry (at least two days). Agar will become soft and unusable if it does not dry properly.

Solution A*

Ingredient	Amount (g/L)
L-Cysteine HCl	0.4
DI Water	0.010

*Filter Sterilize.

Solution B*

Ingredient	Amount (g/L)
Fe-pyrophosphate	0.25
DI Water	0.010

*Filter Sterilize. Note: Keep soluble Ferric pyrophosphate dry and in the dark. Do not use if the chemical loses its green color and becomes brown or yellow. Do not heat over 60 ºC to dissolve. The mixture dissolves readily in a 50 ºC water bath.

ATCC Medium: 271 Escherichia Medium

Solution A

Ingredient	Amount (g/L)
Tryptone	10.0
Yeast extract	1.0
NaCl	8.0
DI Water	0.950

Autoclave at 121 ºC. Cool to 50 ºC. Aseptically add Solutions B (see below). For solid medium, add 15 grams of agar. For soft agar plates, add 3.75 grams of agar.

Solution B*

Ingredient	Amount (g/L)
Glucose	1.0
$CaCl_2$	0.294
Thiamine	0.010
DI Water	0.050

*Filter Sterilize.

2X SG medium – Sporulation of B. subtilis

Ingredient	Amount (g/L)
Nutrient broth Difco (BD234000)	16
Magnesium sulfate heptahydrate	0.5
Potassium chloride	2
Calcium nitrate	10-3 M
Magnesium cloride	10-4 M
Iron sulfate	10-6 M
Glucose	0.1%

References

(1) Stoneman, P.; Diederen, P. Technology diffusion and public policy. *The Economic Journal* **1994**, *104* (425), 918.

(2) Istepanian, R. S. H.; Jovanov, E.; Zhang, Y. T. Guest Editorial Introduction to the Special Section on M-Health: Beyond Seamless Mobility and Global Wireless Health-Care Connectivity. *IEEE Trans. Inform. Technol. Biomed.* **2004**, *8* (4), 405–414.

(3) Lester, R. T.; Ritvo, P.; Mills, E. J.; Kariri, A.; Karanja, S.; Chung, M. H.; Jack, W.; Habyarimana, J.; Sadatsafavi, M.; Najafzadeh, M.; et al. Effects of a mobile phone short message service on antiretroviral treatment adherence in Kenya (WelTel Kenya1): a randomised trial. *Lancet* **2010**, *376* (9755), 1838–1845.

(4) Shannon, M. A.; Bohn, P. W.; Elimelech, M.; Georgiadis, J. G.; Mariñas, B. J.; Mayes, A. M. Science and technology for water purification in the coming decades. *Nature* **2008**, *452* (7185), 301–310.

(5) Richardson, S. D.; Thruston, A. D., Jr; Caughran, T. V.; Chen, P. H.; Collette, T. W.; Schenck, K. M.; Lykins, B. W., Jr; Rav-Acha, C.; Glezer, V. Identification of New Drinking Water Disinfection by-Products from Ozone, Chlorine Dioxide, Chloramine, and Chlorine. In *Environmental Challenges*; Springer Netherlands: Dordrecht, 2000; pp 95–102.

(6) Deborde, M.; von, G. U. Reactions of chlorine with inorganic and organic compounds during water treatment-Kinetics and mechanisms: A critical review. *Water Research* **2008**, *42* (1-2), 13–51.

(7) Aieta, E. M.; Berg, J. D. A review of chlorine dioxide in drinking water treatment. *Journal American Water Works Association* **1986**, *78* (6), 62–72.

(8) Hoigne, J.; Bader, H. The role of hydroxyl radical reactions in ozonation processes in aqueous solutions. *Water Research* **1976**, *10* (5), 377–386.

(9) Richardson, S. D. Disinfection by-products and other emerging contaminants in drinking water. *TrAC Trends in Analytical Chemistry* **2003**, *22* (10), 666–684.

(10) Wolfe, R. L. Ultraviolet disinfection of potable water. *Environ. Sci. Technol.* **1990**, *24* (6), 768–773.

(11) Tobin, R. S.; Smith, D. K.; Horton, A.; Armstrong, V. C. Methods for testing the efficacy of ultraviolet light disinfection devices for drinking water. *Journal American Water Works Association* **1983**, *75* (9), 481–484.

(12) Zhou, H.; Smith, D. W. Advanced technologies in water and wastewater treatment. *Can. J. Civ. Eng.* **2001**, *28* (S1), 49–66.

(13) Christensen, J.; Linden, K. G. How particles affect UV light in the UV disinfection of unfiltered drinking water. *Journal American Water Works Association* **2003**, *95* (4), 179–189.

(14) Massé, D. I.; Masse, L.; Topp, E.; Séguin, G.; Ortega, L. M.; Scott, A.; Pariseau, É. Maintenance strategies for on-site water disinfection by ultraviolet lamps on dairy farms. *Water Quality Research Journal of Canada* **2011**, *46* (1), 2–11.
(15) Parrotta, M. UV disinfection of small groundwater supplies. *Journal American Water Works Association* **1998**, *90* (2), 71–81.
(16) Bisht, P. *Microwave Oven Market by Type (Convection, Grill, Solo), Application (Household, Commercial) and Structure (Built-in, Counter Top) - Global Opportunity Analysis and Industry Forecast, 2014 - 2020*; 2015; p 102.
(17) Li, Q.; Mahendra, S.; Lyon, D. Y.; Brunet, L.; Liga, M. V.; Li, D.; Alvarez, P. J. J. Antimicrobial nanomaterials for water disinfection and microbial control: Potential applications and implications. *Water Research* **2008**, *42* (18), 4591–4602.
(18) Adams, L. K.; Lyon, D. Y.; Alvarez, P. J. J. Comparative eco-toxicity of nanoscale TiO_2, SiO_2, and ZnO water suspensions. *Water Research* **2006**, *40* (19), 3527–3532.
(19) Kim, J.-H.; Kim, J.-H. Encapsulated Triplet–Triplet Annihilation-Based Upconversion in the Aqueous Phase for Sub-Band-Gap Semiconductor Photocatalysis. *J. Am. Chem. Soc.* **2012**, *134* (42), 17478–17481.
(20) Cates, E. L.; Wilkinson, A. P.; Kim, J.-H. Delineating Mechanisms of Upconversion Enhancement by Li^+ Codoping in $Y_2SiO_5:Pr^3$. *J. Phys. Chem. C* **2012**, *116* (23), 12772–12778.
(21) Wang, F.; Liu, X. Recent advances in the chemistry of lanthanide-doped upconversion nanocrystals. *Chem. Soc. Rev.* **2009**, *38* (4), 976–989.
(22) Zhou, B.; Shi, B.; Jin, D.; Liu, X. Controlling upconversion nanocrystals for emerging applications. *Nature Nanotech* **2015**, *10* (11), 924–936.
(23) Chen, J.; Zhao, J. X. Upconversion Nanomaterials: Synthesis, Mechanism, and Applications in Sensing. *Sensors* **2012**, *12* (12), 2414–2435.
(24) Li, X.; Zhang, F.; Zhao, D. Highly efficient lanthanide upconverting nanomaterials: Progresses and challenges. *Nano Today* **2013**, *8* (6), 643–676.
(25) Vázquez, E.; Prato, M. Carbon Nanotubes and Microwaves: Interactions, Responses, and Applications. *ACS Nano* **2009**, *3* (12), 3819–3824.
(26) Vergani, C.; Pavarina, A. C.; Ribeiro, D. G.; Dovigo, L. N.; Sanita, P. V. Microwave Assisted Disinfection Method in Dentistry; Chandra, U., Ed.; 2011; pp 63–89.
(27) Mingos, D. M. P.; Baghurst, D. R. Tilden Lecture. Applications of microwave dielectric heating effects to synthetic problems in chemistry. *Chem. Soc. Rev.* **1991**, *20* (1), 1–47.
(28) Grandbois, M.; Beyer, M.; Rief, M.; Clausen-Schaumann, H.; Gaub, H. E. How strong is a covalent bond? *Science* **1999**, *283* (5408), 1727–1730.
(29) Keller, M. D.; Bellows, W. K.; Guillard, R. Microwave treatment for sterilization of phytoplankton culture media. *Journal of Experimental Marine*

Biology and Ecology **1988**, *117* (3), 279–283.
(30) Neppelenbroek, K. H.; Pavarina, A. C.; Palomari Spolidorio, D. M.; Sgavioli Massucato, E. M.; Spolidorio, L. C.; Vergani, C. E. Effectiveness of microwave disinfection of complete dentures on the treatment of Candida-related denture stomatitis. *J Oral Rehabil* **2008**, *35* (11), 836–846.
(31) Dovigo, L. N.; Pavarina, A. C.; Ribeiro, D. G.; de Oliveira, J. A.; Vergani, C. E.; Machado, A. L. Microwave Disinfection of Complete Dentures Contaminated In Vitrowith Selected Bacteria. *Journal of Prosthodontics* **2009**, *18* (7), 611–617.
(32) Yeo, C. B.; Watson, I. A.; Stewart-Tull, D. E.; Koh, V. H. Heat transfer analysis of staphylococcus aureus on stainless steel with microwave radiation. *J. Appl. Microbiol.* **1999**, *87* (3), 396–401.
(33) Zimmermann, U.; Pilwat, G.; Riemann, F. Dielectric Breakdown of Cell Membranes. *Biophysical Journal* **1974**, *14* (11), 881–899.
(34) Das, D.; Plazas-Tuttle, J.; Sabaraya, I. V.; Jain, S. S.; Sabo-Attwood, T.; Saleh, N. B. An elegant method for large scale synthesis of metal oxide–carbon nanotube nanohybrids for nano-environmental application and implication studies. *Environmental Science: Nano* **2017**, *4*, 60–68.
(35) Aich, N.; Plazas-Tuttle, J.; Lead, J. R.; Saleh, N. B. A critical review of nanohybrids: synthesis, applications and environmental implications. *Environ. Chem.* **2014**, *11* (6), 609.
(36) Saleh, N. B.; Aich, N.; Plazas-Tuttle, J.; Lead, J. R.; Lowry, G. V. Research strategy to determine when novel nanohybrids pose unique environmental risks. *Environmental Science: Nano* **2015**, *2* (1), 11–18.
(37) Saleh, N. B.; Afrooz, A.; Bisesi, J., Jr; Aich, N.; Plazas-Tuttle, J.; Sabo-Attwood, T. Emergent Properties and Toxicological Considerations for Nanohybrid Materials in Aquatic Systems. *Nanomaterials* **2014**, *4* (2), 372–407.
(38) Plazas-Tuttle, J.; Rowles, L., III; Chen, H.; Bisesi, J., Jr; Sabo-Attwood, T.; Saleh, N. B. Dynamism of Stimuli-Responsive Nanohybrids: Environmental Implications. *Nanomaterials* **2015**, *5* (2), 1102–1123.
(39) Roco, M. C. The long view of nanotechnology development: the National Nanotechnology Initiative at 10 years. *J Nanopart Res* **2011**, *13* (2), 427–445.
(40) Wei, G.; Keller, T. F.; Zhang, J.; Jandt, K. D. Novel 1-D biophotonic nanohybrids: protein nanofibers meet quantum dots. *Soft Matter* **2011**, *7* (5), 2011.
(41) Prakash, S.; Malhotra, M.; Shao, W.; Tomaro-Duchesneau, C.; Abbasi, S. Polymeric nanohybrids and functionalized carbon nanotubes as drug delivery carriers for cancer therapy. **2011**, *63* (14-15), 1340–1351.
(42) Ipe, B. I.; Niemeyer, C. M. Nanohybrids Composed of Quantum Dots and Cytochrome P450 as Photocatalysts. *Angew. Chem. Int. Ed.* **2006**, *45* (3), 504–507.

(43) Wang, K.; Li, H.-N.; Wu, J.; Ju, C.; Yan, J.-J.; Liu, Q.; Qiu, B. TiO2-decorated graphene nanohybrids for fabricating an amperometric acetylcholinesterase biosensor. *Analyst* **2011**, *136* (16), 3349.

(44) Ren, D.-M.; Guo, Z.; Du, F.; Liu, Z.-F.; Zhou, Z.-C.; Shi, X.-Y.; Chen, Y.-S.; Zheng, J.-Y. A Novel Soluble Tin(IV) Porphyrin Modified Single-Walled Carbon Nanotube Nanohybrid With Light Harvesting Properties. **2008**, 1–11.

(45) Si, H.-Y.; Liu, C.-H.; Xu, H.; Wang, T.-M.; Zhang, H.-L. Shell-Controlled Photoluminescence in CdSe/CNT Nanohybrids. *Nanoscale Res Lett* **2009**, *4* (10), 1146–1152.

(46) Ghosh, S.; Goudar, V. S.; Padmalekha, K. G.; Bhat, S. V.; Indi, S. S.; Vasan, H. N. ZnO/Ag nanohybrid: synthesis, characterization, synergistic antibacterial activity and its mechanism. *RSC Adv*. **2012**, *2* (3), 930.

(47) Chen, B.; Zhu, Z.; Ma, J.; Yang, M.; Hong, J.; Hu, X.; Qiu, Y.; Chen, J. One-pot, solid-phase synthesis of magnetic multiwalled carbon nanotube/iron oxide composites and their application in arsenic removal. *JOURNAL OF COLLOID AND INTERFACE SCIENCE* **2014**, *434* (C), 9–17.

(48) Chen, L.-J.; Zhao, G.-Z.; Jiang, B.; Sun, B.; Wang, M.; Xu, L.; He, J.; Abliz, Z.; Tan, H.; Li, X.; et al. Smart Stimuli-Responsive Spherical Nanostructures Constructed from Supramolecular Metallodendrimers via Hierarchical Self-Assembly. *J. Am. Chem. Soc*. **2014**, *136* (16), 5993–6001.

(49) Pennakalathil, J.; Özgün, A.; Durmaz, I.; Cetin-Atalay, R.; Tuncel, D. pH-responsive near-infrared emitting conjugated polymer nanoparticles for cellular imaging and controlled-drug delivery. *J. Polym. Sci. Part A: Polym. Chem*. **2014**, *53* (1), 114–122.

(50) Shim, M. S.; Kwon, Y. J. Stimuli-responsive polymers and nanomaterials for gene delivery and imaging applications. *Advanced Drug Delivery Reviews* **2012**, *64* (11), 1046–1059.

(51) Sahoo, B.; Devi, K. S. P.; Banerjee, R.; Maiti, T. K.; Pramanik, P.; Dhara, D. Thermal and pH Responsive Polymer-Tethered Multifunctional Magnetic Nanoparticles for Targeted Delivery of Anticancer Drug. *ACS Appl. Mater. Interfaces* **2013**, *5* (9), 3884–3893.

(52) Wu, T.; Boyer, J.-C. C.; Barker, M.; Wilson, D.; Branda, N. R. A "plug-and-play" method to prepare water-soluble photoresponsive encapsulated upconverting nanoparticles containing hydrophobic molecular switches. *Chemistry of Materials* **2013**, *25* (12), 2495–2502.

(53) Tokarev, I.; Minko, S. Tunable plasmonic nanostructures from noble metal nanoparticles and stimuli-responsive polymers. *Soft Matter* **2012**, *8* (22), 5980.

(54) Luo, Y.; Liu, X.; Tang, X.; Luo, Y.; Zeng, Q.; Deng, X.; Ding, S.; Sun, Y. Gold nanoparticles embedded in Ta2O5/Ta3N5 as active visible-light plasmonic photocatalysts for solar hydrogen evolution. *Journal of Materials Chemistry A: Materials for energy and sustainability* **2014**, *2*, 14927–14939.

(55) Liu, Y.; Yu, Y.-X.; Zhang, W.-D. Photoelectrochemical study on charge

transfer properties of nanostructured Fe2O3 modified by g-C3N4. *International Journal of Hydrogen Energy* **2014**, *39* (17), 9105–9113.

(56) Motornov, M.; Roiter, Y.; Tokarev, I.; Minko, S. Stimuli-responsive nanoparticles, nanogels and capsules for integrated multifunctional intelligent systems. *Progress in Polymer Science* **2010**, *35* (1-2), 174–211.

(57) Mura, S.; Nicolas, J.; Couvreur, P. Stimuli-responsive nanocarriers for drug delivery. *Nature Materials* **2013**, *12* (11), 991–1003.

(58) Stefaniu, C.; Chanana, M.; Wang, D.; Brezesinski, G.; Möhwald, H. Stimuli-Responsive Magnetite Nanoparticle Monolayers. *J. Phys. Chem. C* **2011**, *115* (13), 5478–5484.

(59) Kulkarni, S. A.; Lyles, V. D.; Serem, W. K.; Lu, L.; Kumar, R.; Garno, J. C. Solvent-Responsive Properties of Octadecyltrichlorosiloxane Nanostructures Investigated Using Atomic Force Microscopy in Liquid. *Langmuir* **2014**, *30* (19), 5466–5473.

(60) Lapresta-Fernández, A.; García-García, J. M.; París, R.; Huertas-Roa, R.; Salinas-Castillo, A.; la Llana, de, S. A.; Huertas-Pérez, J. F.; Guarrotxena, N.; Capitán-Vallvey, L. F.; Quijada-Garrido, I. Thermoresponsive Gold Polymer Nanohybrids with a Tunable Cross-Linked MEO 2MA Polymer Shell. *Part. Part. Syst. Charact.* **2014**, *31* (11), 1183–1191.

(61) Zimny, K.; Mascaro, B.; Brunet, T.; Poncelet, O.; Aristégui, C.; Leng, J.; Sandre, O.; Mondain-Monval, O. Design of a fluorinated magneto-responsive material with tuneable ultrasound scattering properties. *J. Mater. Chem. B* **2014**, *2* (10), 1285.

(62) Mimura, K.; Yogo, T. Field-responsive BaTiO3 nanoparticle/organic hybrid synthesized from metal alkoxide. *Journal of the Ceramic Society of Japan* **2011**.

(63) Wu, T.; Wilson, D.; Branda, N. R. Fluorescent Quenching of Lanthanide-Doped Upconverting Nanoparticles by Photoresponsive Polymer Shells. *Chem. Mater* **2014**, *26* (14), 4313–4320.

(64) Miura, R.; Ando, Y.; Hotta, Y.; Nagatani, Y.; Tsuda, A. Acoustic Alignment of a Supramolecular Nanofiber in Harmony with the Sound of Music. *ChemPlusChem* **2014**, *79* (4), 516–523.

(65) Yerushalmi, R.; Scherz, A.; van der Boom, M. E.; Kraatz, H.-B. Stimuli responsive materials: new avenues toward smart organic devices. *J. Mater. Chem.* **2005**, *15* (42), 4480.

(66) Alvarez-Lorenzo, C.; Guney, O.; Oya, T.; Sakai, Y.; Kobayashi, M.; Enoki, T.; Takeoka, Y.; Ishibashi, T.; Kuroda, K.; Tanaka, K.; et al. Reversible adsorption of calcium ions by imprinted temperature sensitive gels. *J. Chem. Phys.* **2001**, *114* (6), 2812.

(67) Hariharasubramanian, A.; Ravichandran, Y. D.; Rajesh, R.; Rajkumari, R.; Selvan, G. K.; Arumugam, S. Functionalization of Multi-walled Carbon Nanotubes with 6-Aminobenzothiazole and their Temperature-dependent

Magnetic Studies. *Fullerenes, Nanotubes and Carbon Nanostructures* **2014**, *22* (10), 874–886.

(68) Fang, W.; Yang, J.; Gong, J.; Zheng, N. Photo- and pH-Triggered Release of Anticancer Drugs from Mesoporous Silica-Coated Pd@Ag Nanoparticles. *Adv. Funct. Mater.* **2011**, *22* (4), 842–848.

(69) Li, Q.; He, X.; Cui, Y.; Shi, P.; Li, S.; Zhang, W. Doubly thermo-responsive nanoparticles constructed with two diblock copolymers prepared through the two macro-RAFT agents co-mediated dispersion RAFT polymerization. *Polym. Chem.* **2015**, *6* (1), 70–78.

(70) He, T.; Di Lena, F.; Neo, K. C.; Chai, C. L. L. Direct synthesis of pH-responsive polymer nanoparticles based on living radical polymerization and traditional radical polymerization. *Soft Matter* **2011**, *7* (7), 3358.

(71) Cammas, S.; Suzuki, K.; Sone, C.; Sakurai, Y. Thermo-responsive polymer nanoparticles with a core-shell micelle structure as site-specific drug carriers. *Journal of controlled …* **1997**.

(72) Tedja, R.; Marquis, C.; Lim, M.; Amal, R. Biological impacts of TiO2 on human lung cell lines A549 and H1299: particle size distribution effects. *J Nanopart Res* **2011**, *13* (9), 3801–3813.

(73) Nel, A. E.; Mädler, L.; Velegol, D.; Xia, T.; Hoek, E. M. V.; Somasundaran, P.; Klaessig, F.; Castranova, V.; Thompson, M. Understanding biophysicochemical interactions at the nano–bio interface. **2009**, *8* (7), 543–557.

(74) Nel, A.; Zhao, Y.; Mädler, L. Environmental Health and Safety Considerations for Nanotechnology. *Acc. Chem. Res.* **2013**, *46* (3), 605–606.

(75) Klaine, S. J.; Alvarez, P. J. J.; Batley, G. E.; Fernandes, T. F.; Handy, R. D.; Lyon, D. Y.; Mahendra, S.; McLaughlin, M. J.; Lead, J. R. Nanomaterials in the environment: behavior, fate, bioavailability, and effects. *Environmental Toxicology and Chemistry* **2009**, *27* (9), 1825–1851.

(76) Lowry, G. V.; Gregory, K. B.; Apte, S. C.; Lead, J. R. Transformations of Nanomaterials in the Environment. *Environ. Sci. Technol* **2012**, *46* (13), 6893–6899.

(77) Sanpui, P.; Zheng, X.; Loeb, J. C.; Bisesi, J. H., Jr; Khan, I. A.; Afrooz, A. R. M. N.; Liu, K.; Badireddy, A.; Wiesner, M. R.; Ferguson, P.; et al. Single-walled carbon nanotubes increase pandemic influenza A H1N1 virus infectivity of lung epithelial cells. *Part Fibre Toxicol* **2014**, *11* (1), 66.

(78) Liu, J.; Legros, S.; Ma, G.; Veinot, J. G. C.; Kammer, von der, F.; Hofmann, T. Influence of surface functionalization and particle size on the aggregation kinetics of engineered nanoparticles. *Chemosphere* **2012**, *87* (8), 918–924.

(79) Diegoli, S.; Manciulea, A. L.; Begum, S.; Jones, I. P.; Lead, J. R.; Preece, J. A. Interaction between manufactured gold nanoparticles and naturally occurring organic macromolecules. *Science of The Total Environment* **2008**, *402* (1), 51–61.

(80) Kim, S. T.; Saha, K.; Kim, C.; Rotello, V. M. The Role of Surface Functionality in Determining Nanoparticle Cytotoxicity. **2013**, *46* (3), 681–691.
(81) Qiu, Y.; Liu, Y.; Wang, L.; Xu, L.; Bai, R.; Ji, Y.; Wu, X.; Zhao, Y.; Li, Y.; Chen, C. Surface chemistry and aspect ratio mediated cellular uptake of Au nanorods. *Biomaterials* **2010**, *31* (30), 7606–7619.
(82) Peng, H.; Dong, R.; Wang, S.; Zhang, Z.; Luo, M.; Bai, C.; Zhao, Q.; Li, J.; Chen, L.; Xiong, H. A pH-responsive nano-carrier with mesoporous silica nanoparticles cores and poly(acrylic acid) shell-layers: Fabrication, characterization and properties for controlled release of salidroside. *International Journal of Pharmaceutics* **2013**, *446* (1-2), 153–159.
(83) Lu, Y.; Mei, Y.; Drechsler, M.; Ballauff, M. Thermosensitive Core–Shell Particles as Carriers for Ag Nanoparticles: Modulating the Catalytic Activity by a Phase Transition in Networks. *Angew. Chem. Int. Ed.* **2006**, *45* (5), 813–816.
(84) Ahmad, M.; Ahmed, E.; Hong, Z. L.; Jiao, X. L.; Abbas, T.; Khalid, N. R. Enhancement in visible light-responsive photocatalytic activity by embedding Cu-doped ZnO nanoparticles on multi-walled carbon nanotubes. *Applied Surface Science* **2013**, *285*, 702–712.
(85) Li, J.; Wu, W.; Han, C.; Zhang, S.; Zhou, H.; Guo, J. Aggregation behavior of pH- and thermo-responsive block copolymer protected gold nanoparticles. *Colloid Polym Sci* **2014**, *292* (7), 1657–1664.
(86) Li, C.; Bolisetty, S.; Chaitanya, K.; Adamcik, J.; Mezzenga, R. Tunable Carbon Nanotube/Protein Core-Shell Nanoparticles with NIR- and Enzymatic-Responsive Cytotoxicity. *Adv. Mater.* **2012**, *25* (7), 1010–1015.
(87) Li, S.; Hu, K.; Cao, W.; Sun, Y.; Sheng, W.; Li, F.; Wu, Y.; Liang, X.-J. pH-responsive biocompatible fluorescent polymer nanoparticles based on phenylboronic acid for intracellular imaging and drug delivery. *Nanoscale* **2014**, *6* (22), 13701–13709.
(88) Guo, J.; Wang, N.; Wu, J.; Ye, Q.; Zhang, C.; Xing, X.-H.; Yuan, J. Hybrid nanoparticles with CO2-responsive shells and fluorescence-labelled magnetic cores. *J. Mater. Chem. B* **2013**, *2* (4), 437.
(89) Liu, X.; Wang, X.; Zha, L.; Lin, D.; Yang, J.; Zhou, J.; Zhang, L. Temperature- and pH-tunable plasmonic properties and SERS efficiency of the silver nanoparticles within the dual stimuli-responsive microgels. *Journal of Materials Chemistry C: Materials for optical and electronic devices* **2014**, *2*, 7326–7335.
(90) Popat, A.; Liu, J.; Lu, G. Q. M.; Qiao, S. Z. A pH-responsive drug delivery system based on chitosan coated mesoporous silica nanoparticles. *J. Mater. Chem.* **2012**, *22* (22), 11173.
(91) Lupitskyy, R.; Motornov, M.; Minko, S. Single Nanoparticle Plasmonic Devices by the "Grafting to" Method. *Langmuir* **2008**, *24* (16), 8976–8980.
(92) Liras, M.; Peinado, E.; Cañamero, P.; Quijada-Garrido, I.; García, O. Smart photoluminescent nanohybrids based on CdSe quantum dots capped with

multidentate thiolated pH-responsive and thermoresponsive polymers for nanosensing. *J. Polym. Sci. Part A: Polym. Chem.* **2014**, *52* (21), 3087–3095.
(93) Ast, S.; Rutledge, P. J.; Todd, M. H. pH-Responsive quantum dots (RQDs) that combine a fluorescent nanoparticle with a pH-sensitive dye. *Phys. Chem. Chem. Phys.* **2014**, *16*, 25255–25257.
(94) Iatridi, Z.; Tsitsilianis, C. pH responsive MWCNT–star terpolymer nanohybrids. *Soft Matter* **2012**, *9* (1), 185.
(95) Nadrah, P.; Porta, F.; Planinšek, O.; Kros, A.; Gaberšček, M. Poly(propylene imine) dendrimer caps on mesoporous silica nanoparticles for redox-responsive release: smaller is better. *Phys. Chem. Chem. Phys.* **2013**, *15* (26), 10740.
(96) Chen, J.-K.; Chang, C.-J. Fabrications and Applications of Stimulus-Responsive Polymer Films and Patterns on Surfaces: A Review. **2014**, *7* (2), 805–875.
(97) Shalviri, A.; Chan, H. K.; Raval, G.; Abdekhodaie, M. J.; Liu, Q.; Heerklotz, H.; Wu, X. Y. Design of pH-responsive nanoparticles of terpolymer of poly(methacrylic acid), polysorbate 80 and starch for delivery of doxorubicin. *Colloids and Surfaces B: Biointerfaces* **2013**, *101*, 405–413.
(98) Sun, J.; Yi, C.; Wei, W.; Zhao, D.; Hu, Q.; Liu, X. Nanohybrids from Direct Chemical Self-Assembly of Poly(styrene- alt-maleic anhydride) as pH-Responsive Particulate Emulsifiers. *Langmuir* **2014**, *30* (49), 14757–14764.
(99) Wang, K.; Peng, H.; Thurecht, K. J.; Puttick, S.; Whittaker, A. K. pH-responsive star polymer nanoparticles: potential 19F MRI contrast agents for tumour-selective imaging. *Polym. Chem.* **2013**, *4* (16), 4480–10.
(100) Li, D.; He, Q.; Cui, Y.; Li, J. Fabrication of pH-Responsive Nanocomposites of Gold Nanoparticles/Poly(4-vinylpyridine). *Chem. Mater* **2007**, *19* (3), 412–417.
(101) Miyata, T.; Onakamae, K.; Hoffman, A. S.; Kanzaki, Y. Stimuli-Sensitivities of Hydrogels Containing Phosphate Groups. *Macromol. Chem. Phys.* **1994**, *195* (4), 1111–1120.
(102) Lavignac, N.; Lazenby, M.; Foka, P.; Malgesini, B.; Verpilio, I.; Ferruti, P.; Duncan, R. Synthesis and Endosomolytic Properties of Poly(amidoamine) Block Copolymers. *Macromol. Biosci.* **2004**, *4* (10), 922–929.
(103) Tarn, D.; Ashley, C. E.; Xue, M.; Carnes, E. C.; Zink, J. I.; Brinker, C. J. Mesoporous Silica Nanoparticle Nanocarriers: Biofunctionality and Biocompatibility. *Acc. Chem. Res.* **2013**, *46* (3), 792–801.
(104) Kotsuchibashi, Y.; Wang, Y.; Kim, Y.-J.; Ebara, M.; Aoyagi, T.; Narain, R. Simple Coating with pH-Responsive Polymer-Functionalized Silica Nanoparticles of Mixed Sizes for Controlled Surface Properties. *ACS Appl. Mater. Interfaces* **2013**, *5* (20), 10004–10010.
(105) Qiu, Y.; Park, K. Environment-sensitive hydrogels for drug delivery. *Advanced Drug Delivery Reviews* **2001**, *53* (3), 321–339.
(106) Chiantore, O.; Guaita, M.; Trossarelli, L. Solution properties of poly (N-isopropylacrylamide). *Makromol. Chem.* **1979**, *180*, 969–973.

(107) Murray, M.; Rana, F.; Haq, I.; Cook, J.; Chowdhry, B. Z.; Snowden, M. J. Colloidal microgel systems: phase transition properties in aqueous solution of poly(N-isopropylacrylamide). *J. Chem. Soc., Chem. Commun.* **1994**, No. 15, 1803–2.

(108) Mikheeva, L. M.; Grinberg, N. V.; Mashkevich, A. Y.; Grinberg, V. Y.; Le Thi Minh Thanh; Makhaeva, E. E.; Khokhlov, A. R. Microcalorimetric Study of Thermal Cooperative Transitions in Poly(N -vinylcaprolactam) Hydrogels. *Macromolecules* **1997**, *30* (9), 2693–2699.

(109) Popescu, I.; Prisacaru, A. I.; Suflet, D. M.; Fundueanu, G. Thermo- and pH-sensitivity of poly(N-vinylcaprolactam-co-maleic acid) in aqueous solution. *Polym. Bull.* **2014**, *71* (11), 2863–2880.

(110) Schild, H. G. Poly(N-isopropylacrylamide): experiment, theory and application. *Progress in Polymer Science* **1992**, *17* (2), 163–249.

(111) Carregal-Romero, S.; Buurma, N. J.; Pérez-Juste, J.; Liz-Marzán, L. M.; Hervés, P. Catalysis by Au@pNIPAM Nanocomposites: Effect of the Cross-Linking Density. *Chem. Mater* **2010**, *22* (10), 3051–3059.

(112) Lee, R.-S.; Wang, S.-W.; Li, Y.-C.; Fang, J.-Y. Synthesis and characterization of thermo-responsive and photo-cleavable block copolymers as nanocarriers. *RSC Adv.* **2014**, *5*, 497–512.

(113) Liu, X.; Tian, Z.; Chen, C.; Allcock, H. R. UV-cleavable unimolecular micelles: synthesis and characterization toward photocontrolled drug release carriers. *Polym. Chem.* **2013**, *4* (4), 1115–11.

(114) Apostol, M.; Mironava, T.; Yang, N.-L.; Pernodet, N.; Rafailovich, M. H. Cell sheet patterning using photo-cleavable polymers. **2011**, *43* (8), 723–732.

(115) Vivero-Escoto, J. L.; Vega, D. L. Stimuli-responsive protoporphyrin IX silica-based nanoparticles for photodynamic therapy in vitro. *RSC Adv.* **2014**, *4* (28), 14400.

(116) Feng, W.; Luo, W.; Feng, Y. Photo-responsive carbon nanomaterials functionalized by azobenzene moieties: structures, properties and application. *Nanoscale* **2012**, *4* (20), 6118.

(117) Bobrovsky, A.; Shibaev, V.; Cigl, M.; Hamplová, V.; Hampl, F.; Elyashevitch, G. Photochromic LC–polymer composites containing azobenzene chromophores with thermally stable Z-isomers. *J. Mater. Chem. C* **2014**, *2* (22), 4482–4488.

(118) Shinmori, H.; Takeuchi, M.; Shinkai, S. Spectroscopic detection of diols and sugars by a colour change in boronic acid-appended spirobenzopyrans. *J. Chem. Soc., Perkin Trans. 2* **1996**, No. 1, 1–3.

(119) Sidhaye, D. S.; Kashyap, S.; Sastry, M.; Hotha, S.; Prasad, B. L. V. Gold Nanoparticle Networks with Photoresponsive Interparticle Spacings. *Langmuir* **2005**, *21* (17), 7979–7984.

(120) Luo, J.; Zhou, Q.; Sun, J.; Jiang, J.; Zhou, X.; Zhang, H.; Liu, X. Photoresponsive water-dispersible polyaniline nanoparticles through template

synthesis with copolymer micelle containing coumarin groups. *J. Polym. Sci. Part A: Polym. Chem.* **2012**, *50* (19), 4037–4045.

(121) Takenaka, T.; Endo, M.; Suzuki, Y.; Yang, Y.; Emura, T.; Hidaka, K.; Kato, T.; Miyata, T.; Namba, K.; Sugiyama, H. Photoresponsive DNA Nanocapsule Having an Open/Close System for Capture and Release of Nanomaterials. *Chem. Eur. J.* **2014**, *20* (46), 14951–14954.

(122) Valentini, L.; Cardinali, M.; Kenny, J. M.; Prato, M.; Monticelli, O. A Photoresponsive Hybrid Nanomaterial Based on Graphene and Polyhedral Oligomeric Silsesquioxanes. *Eur. J. Inorg. Chem.* **2012**, *2012* (32), 5282–5287.

(123) Meng, F.; Hennink, W. E.; Zhong, Z. Reduction-sensitive polymers and bioconjugates for biomedical applications. *Biomaterials* **2009**, *30* (12), 2180–2198.

(124) Li, J.; Zhang, X.; Chen, S.; You, Q.; He, R.; Shi, J.; Cao, Y.; Chen, Y. Multi-responsive drug release from hydrogen-bonding multilayers containing PEGylated nanoparticles and azobenzenes. *J. Mater. Chem. B* **2014**, *2* (28), 4422.

(125) Wang, Y.; Wu, G.; Li, X.; Wang, Y.; Gao, H.; Ma, J. On–off switchable drug release from multi-responsive degradable poly(ether urethane) nanoparticles. *Biomater. Sci.* **2013**, *1* (6), 614–11.

(126) Chang, B.; Sha, X.; Guo, J.; Jiao, Y.; Wang, C.; Yang, W. Thermo and pH dual responsive, polymer shell coated, magnetic mesoporous silica nanoparticles for controlled drug release. *J. Mater. Chem.* **2011**, *21* (25), 9239–9239.

(127) Morones-Ramírez, J. R. Coupling Metallic Nanostructures to Thermally Responsive Polymers Allows the Development of Intelligent Responsive Membranes. *International Journal of Polymer Science* **2014**, *2014* (6), 1–7.

(128) Ma, R.; Shi, L. Phenylboronic acid-based glucose-responsive polymeric nanoparticles: synthesis and applications in drug delivery. **2014**, *5* (5), 1503–1518.

(129) Wang, D.; Xu, Z.; Chen, Z.; Liu, X.; Hou, C.; Zhang, X.; Zhang, H. Fabrication of Single-Hole Glutathione-Responsive Degradable Hollow Silica Nanoparticles for Drug Delivery. *ACS Appl. Mater. Interfaces* **2014**, *6* (15), 12600–12608.

(130) Hu, Q.; Katti, P. S.; Gu, Z. Enzyme-responsive nanomaterials for controlled drug delivery. *Nanoscale* **2014**, *6* (21), 12273–12286.

(131) Afrooz, A. R. M. N.; Sivalapalan, S. T.; Murphy, C. J.; Hussain, S. M.; Schlager, J. J.; Saleh, N. B. Spheres vs. rods: The shape of gold nanoparticles influences aggregation and deposition behavior. *Chemosphere* **2013**, *91* (1), 93–98.

(132) Schneider, G. F.; Subr, V.; Ulbrich, K.; Decher, G. Multifunctional Cytotoxic Stealth Nanoparticles. A Model Approach with Potential for Cancer Therapy. *Nano Lett.* **2009**, *9* (2), 636–642.

(133) Ryman-Rasmussen, J. P.; Riviere, J. E.; Monteiro-Riviere, N. A. Surface

Coatings Determine Cytotoxicity and Irritation Potential of Quantum Dot Nanoparticles in Epidermal Keratinocytes. *J Investig Dermatol* **2006**, *127* (1), 143–153.

(134) Pakrashi, S.; Kumar, D.; Iswarya, V.; Bhuvaneshwari, M.; Chandrasekaran, N.; Mukherjee, A. A comparative ecotoxicity analysis of α- and γ-phase aluminium oxide nanoparticles towards a freshwater bacterial isolate Bacillus licheniformis. *Bioprocess Biosyst Eng* **2014**, *37* (12), 2415–2423.

(135) Chambers, B.; Afrooz, A. R. M. N.; Bae, S.; Aich, N.; Katz, L.; Saleh, N. B.; Kirisits, M. J. Effects of Chloride and Ionic Strength on Physical Morphology, Dissolution, and Bacterial Toxicity of Silver Nanoparticles. *Environ. Sci. Technol.* **2014**, *48* (1), 761–769.

(136) Liu, X.; Chen, G.; Su, C. Influence of Collector Surface Composition and Water Chemistry on the Deposition of Cerium Dioxide Nanoparticles: QCM-D and Column Experiment Approaches. *Environ. Sci. Technol.* **2012**, *46* (12), 6681–6688.

(137) Afrooz, A. R. M. N.; Khan, I. A.; Hussain, S. M.; Saleh, N. B. Mechanistic Heteroaggregation of Gold Nanoparticles in a Wide Range of Solution Chemistry. *Environ. Sci. Technol.* **2013**, *47* (4), 1853–1860.

(138) Elimelech, M.; Jia, X.; Gregory, J.; Williams, R. *Particle Deposition & Aggregation*; Butterworth-Heinemann, 1998.

(139) Afrooz, A. R. M. N.; Hussain, S. M.; Saleh, N. B. Aggregate size and structure determination of nanomaterials in physiological media: importance of dynamic evolution. *J Nanopart Res* **2014**, *16* (12), 2771–2777.

(140) Sabo-Attwood, T.; Unrine, J. M.; Stone, J. W.; Murphy, C. J.; Ghoshroy, S.; Blom, D.; Bertsch, P. M.; Newman, L. A. Uptake, distribution and toxicity of gold nanoparticles in tobacco (Nicotiana xanthi) seedlings. *Nanotoxicology* **2012**, *6* (4), 353–360.

(141) Brant, J.; Lecoanet, H.; Wiesner, M. R. Aggregation and Deposition Characteristics of Fullerene Nanoparticles in Aqueous Systems. *J Nanopart Res* **2005**, *7* (4-5), 545–553.

(142) Sergio, M.; Behzadi, H.; Otto, A.; van der Spoel, D. Fullerenes toxicity and electronic properties. *Environ Chem Lett* **2012**, *11* (2), 105–118.

(143) Dupin, D.; Rosselgong, J.; Armes, S. P.; Routh, A. F. Swelling Kinetics for a pH-Induced Latex-to-Microgel Transition. *Langmuir* **2007**, *23* (7), 4035–4041.

(144) Domingos, R. F.; Franco, C.; Pinheiro, J. P. The role of charged polymer coatings of nanoparticles on the speciation and fate of metal ions in the environment. *Environ Sci Pollut Res* **2014**, *22* (4), 2900–2906.

(145) Felix, L. C.; Ortega, V. A.; Ede, J. D.; Goss, G. G. Physicochemical Characteristics of Polymer-Coated Metal-Oxide Nanoparticles and their Toxicological Effects on Zebrafish (Danio rerio) Development. *Environ. Sci. Technol.* **2013**, 130603125147001–130603125147008.

(146) Su, H.-L.; Chiao; Lin; Shen; Liao, J.-W.; Bau; Wei; Tseng; Hsu, S.; Lai; et al.

Efficacy and safety of nanohybrids comprising silver nanoparticles and silicate clay for controlling Salmonella infection. *IJN* **2012**, 2421–12.

(147) Gonçalves, M.; Figueira, P.; Maciel, D.; Rodrigues, J.; Qu, X.; Liu, C.; Tomás, H.; Li, Y. pH-sensitive Laponite®/doxorubicin/alginate nanohybrids with improved anticancer efficacy. *Acta Biomaterialia* **2014**, *10* (1), 300–307.

(148) Ghosh, M.; Brahmachari, S.; Das, P. K. pH-Responsive Single Walled Carbon Nanotube Dispersion for Target Specific Release of Doxorubicin to Cancer Cells. *Macromol. Biosci.* **2014**, *14* (12), 1795–1806.

(149) Hu, C.; Liu, Y.; Li, X.; Li, M. Biochemical Responses of Duckweed (Spirodela polyrhiza) to Zinc Oxide Nanoparticles. *Arch Environ Contam Toxicol* **2012**, *64* (4), 643–651.

(150) Oukarroum, A.; Bras, S.; Perreault, F.; Popovic, R. Inhibitory effects of silver nanoparticles in two green algae, Chlorella vulgaris and Dunaliella tertiolecta. *Ecotoxicology and Environmental Safety* **2012**, *78* (C), 80–85.

(151) Alloy, M. M.; Roberts, A. P. Effects of suspended multi-walled carbon nanotubes on daphnid growth and reproduction. *Ecotoxicology and Environmental Safety* **2011**, *74* (7), 1839–1843.

(152) Ibarra, L. E.; Tarres, L.; Bongiovanni, S.; Barbero, C. A.; Kogan, M. J.; Rivarola, V. A.; Bertuzzi, M. L.; Yslas, E. I. Assessment of polyaniline nanoparticles toxicity and teratogenicity in aquatic environment using Rhinella arenarum model. *Ecotoxicology and Environmental Safety* **2015**, *114* (C), 84–92.

(153) Lin, D.; Ji, J.; Long, Z.; Yang, K.; Wu, F. The influence of dissolved and surface-bound humic acid on the toxicity of TiO_2 nanoparticles to Chlorella sp. *Water Research* **2012**, *46* (14), 4477–4487.

(154) Yang, H.; Masse, S.; Zhang, H.; Hélary, C.; Li, L.; Coradin, T. Surface reactivity of hydroxyapatite nanocoatings deposited on iron oxide magnetic spheres toward toxic metals. *JOURNAL OF COLLOID AND INTERFACE SCIENCE* **2014**, *417* (C), 1–8.

(155) Miller, R. J.; Bennett, S.; Keller, A. A.; Pease, S.; Lenihan, H. S. TiO2 Nanoparticles Are Phototoxic to Marine Phytoplankton. *PLoS ONE* **2012**, *7* (1), e30321–e30327.

(156) Xiong, D.; Fang, T.; Yu, L.; Sima, X.; Zhu, W. Effects of nano-scale TiO2, ZnO and their bulk counterparts on zebrafish: Acute toxicity, oxidative stress and oxidative damage. *Science of the Total Environment, The* **2011**, *409* (8), 1444–1452.

(157) Dale, A. L.; Casman, E. A.; Lowry, G. V.; Lead, J. R.; Viparelli, E.; Baalousha, M. Modeling Nanomaterial Environmental Fate in Aquatic Systems. *Environ. Sci. Technol.* **2015**, *49* (5), 2587–2593.

(158) Nel, A.; Xia, T.; Meng, H.; Wang, X.; Lin, S.; Ji, Z.; Zhang, H. Nanomaterial Toxicity Testing in the 21st Century: Use of a Predictive Toxicological Approach and High-Throughput Screening. *Acc. Chem. Res.* **2013**, *46* (3), 607–

621.
(159) Epa, V. C.; Burden, F. R.; Tassa, C.; Weissleder, R.; Shaw, S.; Winkler, D. A. Modeling Biological Activities of Nanoparticles. *Nano Lett*. **2012**, *12* (11), 5808–5812.
(160) De Volder, M. F. L.; Tawfick, S. H.; Baughman, R. H.; Hart, A. J. Carbon Nanotubes: Present and Future Commercial Applications. *Science* **2013**, *339* (6119), 535–539.
(161) Iijima, S. Helical microtubules of graphitic carbon. *Nature* **1991**, *354* (6348), 56–58.
(162) Peter, J.; Harris, F. *Carbon nanotube science—synthesis, properties and applications*; Synthesis, Properties and Applications; Cambridge University Press: Cambridge, 2009; pp 1–301.
(163) Imholt, T. J.; Dyke, C. A.; Hasslacher, B.; Perez, J. M.; Price, D. W.; Roberts, J. A.; Scott, J. B.; Wadhawan, A.; Ye, Z.; Tour, J. M. Nanotubes in Microwave Fields: Light Emission, Intense Heat, Outgassing, and Reconstruction. **2003**, *15* (21), 3969–3970.
(164) MacKenzie, K.; Dunens, O.; Harris, A. T. A review of carbon nanotube purification by microwave assisted acid digestion. *Separation and Purification Technology* **2009**, *66* (2), 209–222.
(165) Wu, Z.; Wang, Z.; Yu, F.; Thakkar, M.; Mitra, S. Variation in chemical, colloidal and electrochemical properties of carbon nanotubes with the degree of carboxylation. *J Nanopart Res* **2017**, 1–9.
(166) Higginbotham, A. L.; Moloney, P. G.; Waid, M. C.; Duque, J. G.; Kittrell, C.; Schmidt, H. K.; Stephenson, J. J.; Arepalli, S.; Yowell, L. L.; Tour, J. M. Carbon nanotube composite curing through absorption of microwave radiation. *Composites Science and Technology* **2008**, *68* (15-16), 3087–3092.
(167) Frank, S.; Poncharal, P.; Wang, Z.; Heer, W. Carbon nanotube quantum resistors. *Science* **1998**, *280* (5370), 1744–1746.
(168) Dresselhaus, M. S.; Dresselhaus, G.; Saito, R. Physics of carbon nanotubes. *Carbon* **1995**, *33* (7), 883–891.
(169) Gannon, C. J.; Cherukuri, P.; Yakobson, B. I.; Cognet, L.; Kanzius, J. S.; Kittrell, C.; Weisman, R. B.; Pasquali, M.; Schmidt, H. K.; Smalley, R. E.; et al. Carbon nanotube-enhanced thermal destruction of cancer cells in a noninvasive radiofrequency field. *Cancer* **2007**, *110* (12), 2654–2665.
(170) Galema, S. A. Microwave chemistry. *Chem. Soc. Rev*. **1997**, *26* (3), 233–236.
(171) Riaz, U.; Ashraf, S. M.; Farooq, M. Effect of pH on the microwave-assisted degradation of methyl orange using poly(1-naphthylamine) nanotubes in the absence of UV–visible radiation. *Colloid Polym Sci* **2014**.
(172) Roberts, J. A.; Imholt, T.; Ye, Z.; Dyke, C. A.; Price, D. W., Jr.; Tour, J. M. Electromagnetic wave properties of polymer blends of single wall carbon nanotubes using a resonant microwave cavity as a probe. *J. Appl. Phys*. **2004**, *95* (8), 4352–4356.

(173) Higginbotham, A. L.; Stephenson, J. J.; Smith, R. J.; Killips, D. S.; Kempel, L. C.; Tour, J. M. Tunable Permittivity of Polymer Composites through Incremental Blending of Raw and Functionalized Single-Wall Carbon Nanotubes. *J. Phys. Chem. C* **2007**, *111* (48), 17751–17754.
(174) Kekeç, Ö.; Gökalsın, B.; Karaltı, İ.; Kayhan, F. E.; Sesal, N. C. Effects of Chlorine Stress on Pseudomonas aeruginosa Biofilm and Analysis of Related Gene Expressions. *Current Microbiology* **2016**, *73* (2), 228–235.
(175) Guerfi, N.; Bourbia, O.; Achour, S. Study of Erbium Oxidation by XPS and UPS. *MSF* **2005**, *480-481*, 193–196.
(176) Rigdon, W. A.; Huang, X. Carbon monoxide tolerant platinum electrocatalysts on niobium doped titania and carbon nanotube composite supports. *Journal of Power Sources* **2014**, *272* (c), 845–859.
(177) Miritello, M.; Savio, Lo, R.; Piro, A. M.; Franzò, G.; Priolo, F.; Iacona, F.; Bongiorno, C. Optical and structural properties of Er_2O_3 films grown by magnetron sputtering. *J. Appl. Phys.* **2006**, *100* (1).
(178) Li, C.; Liu, H.; Yang, J. A facile hydrothermal approach to the synthesis of nanoscale rare earth hydroxides. *Nanoscale Res Lett* **2015**, *10* (1), 5687–6.
(179) Aksel, S.; Eder, D. Catalytic effect of metal oxides on the oxidation resistance in carbon nanotube–inorganic hybrids. **2010**, *20* (41), 9149–9146.
(180) Mosquera, E.; Diaz-Droguett, D. E.; Carvajal, N.; Roble, M.; Morel, M.; Espinoza, R. Characterization and hydrogen storage in multi-walled carbon nanotubes grown by aerosol-assisted CVD method. *Diamond & Related Materials* **2014**, *43* (C), 66–71.
(181) Foster, H. A.; Sheel, D. W.; Sheel, P.; Evans, P.; Varghese, S.; Rutschke, N.; Yates, H. M. Antimicrobial activity of titania/silver and titania/copper films prepared by CVD. *Journal of Photochemistry and Photobiology A: Chemistry* **2010**, *216* (2-3), 283–289.
(182) Dunlop, P. S. M.; Sheeran, C. P.; Byrne, J. A.; McMahon, M. A. S.; Boyle, M. A.; McGuigan, K. G. Inactivation of clinically relevant pathogens by photocatalytic coatings. *Journal of Photochemistry and Photobiology A: Chemistry* **2010**, *216* (2-3), 303–310.
(183) Lonnen, J.; Kilvington, S.; Kehoe, S. C.; Al-Touati, F.; McGuigan, K. G. Solar and photocatalytic disinfection of protozoan, fungal and bacterial microbes in drinking water. *Water Research* **2005**, *39* (5), 877–883.
(184) Chen, Z.; Chen, H.; Hu, H.; Yu, M.; Li, F.; Zhang, Q.; Zhou, Z.; Yi, T.; Huang, C. Versatile Synthesis Strategy for Carboxylic Acid–functionalized Upconverting Nanophosphors as Biological Labels. *J. Am. Chem. Soc.* **2008**, *130* (10), 3023–3029.
(185) O'Toole, A.; Ricker, E. B.; Nuxoll, E. Thermal mitigation of Pseudomonas aeruginosa biofilms. *Biofouling* **2015**, *31* (8), 665–675.
(186) Park, H.; Park, H.-J.; Kim, J. A.; Lee, S. H.; Kim, J. H.; Yoon, J.; Park, T. H. Inactivation of Pseudomonas aeruginosa PA01 biofilms by hyperthermia using

superparamagnetic nanoparticles. *Journal of Microbiological Methods* **2011**, *84* (1), 41–45.
(187) Kuchma, T. Synergistic effect of microwave heating and hydrogen peroxide on inactivation of microorganisms. *J Microw Power Electromagn Energy* **1998**, *33* (2), 77–87.
(188) Elkins, J. G.; Hassett, D. J.; Stewart, P. S.; Schweizer, H. P.; McDermott, T. R. Protective role of catalase in Pseudomonas aeruginosa biofilm resistance to hydrogen peroxide. *Applied and Environmental Microbiology* **1999**, *65* (10), 4594–4600.
(189) He, W.; Jia, H.; Cai, J.; Han, X.; Zheng, Z.; Wamer, W. G.; Yin, J.-J. Production of Reactive Oxygen Species and Electrons from Photoexcited ZnO and ZnS Nanoparticles: A Comparative Study for Unraveling their Distinct Photocatalytic Activities. *J. Phys. Chem. C* **2016**, *120* (6), 3187–3195.
(190) Sun, P.; Tyree, C.; Huang, C.-H. Inactivation of Escherichia coli, Bacteriophage MS2, and Bacillus Spores under UV/H_2O_2 and UV/Peroxydisulfate Advanced Disinfection Conditions. *Environ. Sci. Technol.* **2016**, *50* (8), 4448–4458.
(191) Chang, Q.; He, H.; Ma, Z. Efficient disinfection of Escherichia coli in water by silver loaded alumina. *Journal of Inorganic Biochemistry* **2008**, *102* (9), 1736–1742.
(192) Dimkpa, C. O.; Calder, A.; Gajjar, P.; Merugu, S.; Huang, W.; Britt, D. W.; McLean, J. E.; Johnson, W. P.; Anderson, A. J. Interaction of silver nanoparticles with an environmentally beneficial bacterium, Pseudomonas chlororaphis. *Journal of Hazardous Materials* **2011**, *188* (1-3), 428–435.
(193) Hoffmann, M. R.; Martin, S. T.; Choi, W. Y.; Bahnemann, D. W. Environmental Applications of Semiconductor Photocatalysis. *Chemical reviews* **1995**, *95* (1), 69–96.
(194) Wang, W.; Serp, P.; Kalck, P.; Faria, J. L. Visible light photodegradation of phenol on MWNT-TiO2 composite catalysts prepared by a modified sol–gel method. *Journal of Molecular Catalysis A: Chemical* **2005**, *235* (1-2), 194–199.
(195) Woan, K.; Pyrgiotakis, G.; Sigmund, W. Photocatalytic Carbon-Nanotube-TiO_2 Composites. **2009**, *21* (21), 2233–2239.
(196) Banerjee, S.; Wong, S. S. Synthesis and Characterization of Carbon Nanotube–Nanocrystal Heterostructures. *Nano Lett.* **2002**, *2* (3), 195–200.
(197) Sun, S.; Gao, L.; Liu, Y. Enhanced dye-sensitized solar cell using graphene-TiO_2 photoanode prepared by heterogeneous coagulation. *Appl. Phys. Lett.* **2010**, *96* (8), 083113–083113.
(198) Kamat, P. V. Composite semiconductor nanoclusters. *Semiconductor Nanoclusters- Physical, Chemical, and Catalytic Aspects* **1997**, *103*, 237–259.
(199) Kamat, P. V.; Flumiani, M.; Dawson, A. Metal-metal and metal-semiconductor composite nanoclusters. *Colloids and Surfaces a-Physicochemical and*

Engineering Aspects **2002**, *202* (2-3), 269–279.
(200) Lettmann, C.; Hildenbrand, K.; Kisch, H.; Macyk, W.; Maier, W. F. Visible light photodegradation of 4-chlorophenol with a coke-containing titanium dioxide photocatalyst. *"Applied Catalysis B, Environmental"* **2001**, *32* (4), 215–227.
(201) Peigney, A.; Laurent, C.; Flahaut, E.; Bacsa, R. R.; Rousset, A. Specific surface area of carbon nanotubes and bundles of carbon nanotubes. *Carbon* **2001**, *39* (4), 507–514.
(202) Zhang, L.; Zhu, H.; Song, Y.; Zhang, Y.; Huang, Y. The electromagnetic characteristics and absorbing properties of multi-walled carbon nanotubes filled with Er_2O_3 nanoparticles as microwave absorbers. *Materials Science and Engineering: B* **2008**, *153* (1-3), 78–82.
(203) Metaxas, A. C.; Meredith, R. J. *Industrial Microwave Heating: IEE Power Engineering*; Peter Peregrinus Ltd.: London, UK, 1983.
(204) Feynman, R. P.; Leighton, R. B.; Sands, M. *The Feynman Lectures on Physics*; Basic Books, 2015.
(205) Marcuvitz, N. *Waveguide Handbook*; McGraw-Hill Book Company, Inc.: New York, 1951.
(206) Irin, F.; Shrestha, B.; Cañas, J. E.; Saed, M. A.; Green, M. J. Detection of carbon nanotubes in biological samples through microwave-induced heating. *Carbon* **2012**, *50* (12), 4441–4449.
(207) Li, S.; Irin, F.; Atore, F. O.; Green, M. J.; Cañas-Carrell, J. E. Determination of multi-walled carbon nanotube bioaccumulation in earthworms measured by a microwave-based detection technique. *Science of The Total Environment* **2013**, *445-446*, 9–13.
(208) International Organization for Standardization. Water quality — Detection and enumeration of bacteriophages — Part 1: Enumeration of F-specific RNA bacteriophages (ISO 10705-1:1995). **1998**, 1–10.
(209) World Health Organization. *Emerging Issues in Water and Infectious Disease*; 2003.
(210) World Health Organization; UNICEF. Progress on Sanitation and Drinking Water. **2015**, 1–90.
(211) Koivunen, J.; Heinonen-Tanski, H. Inactivation of enteric microorganisms with chemical disinfectants, UV irradiation and combined chemical/UV treatments. *Water Research* **2005**, *39* (8), 1519–1526.
(212) Li, M.; Pokhrel, S.; Jin, X.; Mädler, L.; Damoiseaux, R.; Hoek, E. M. V. Stability, Bioavailability, and Bacterial Toxicity of ZnO and Iron-Doped ZnO Nanoparticles in Aquatic Media. *Environ. Sci. Technol.* **2011**, *45* (2), 755–761.
(213) Facile, N.; Barbeau, B.; Prevost, M.; Koudjonou, B. Evaluating bacterial aerobic spores as a surrogate for Giardia and Cryptosporidium inactivation by ozone. *Water Research* **2000**, *34* (12), 3238–3246.
(214) Barbeau, B.; Boulos, L.; Desjardins, R. A modified method for the enumeration

of aerobic spore-forming bacteria. *Canadian Journal of Microbiology* **1997**, *43* (10), 976–980.
(215) Abeledo-Lameiro, M. J.; Reboredo-Fernández, A.; Polo-López, M. I.; Fernandez-Ibañez, P.; Ares-Mazás, E.; Gómez-Couso, H. Photocatalytic inactivation of the waterborne protozoan parasite Cryptosporidium parvum using TiO2/H2O2 under simulated and natural solar conditions. *Catalysis Today* **2017**, *280* (Part 1), 132–138.
(216) Kim, B. R.; Anderson, J. E.; Mueller, S. A.; Gaines, W. A. Literature review—efficacy of various disinfectants against Legionella in water systems. *Water Research* **2002**, *36* (18), 4433–4444.
(217) Nogueira, R.; Utecht, K. U.; Exner, M.; Verstraete, W.; Rosenwinkel, K. H. Strategies for the reduction of Legionella in biological treatment systems. *Water Science & Technology* **2016**, *74* (4), 816–823.
(218) Fraser, D. W.; Tsai, T. R.; Orenstein, W.; Parkin, W. E.; Beecham, H. J.; Sharrar, R. G.; Harris, J.; Mallison, G. F.; Martin, S. M.; McDade, J. E.; et al. Legionnaires' Disease. *New England Journal of Medicine* **1977**, *297* (22), 1189–1197.
(219) Cheng, Y. W.; Chan, R. C. Y.; Wong, P. K. Disinfection of Legionella pneumophila by photocatalytic oxidation. **2007**, *41* (4), 842–852.
(220) Hoffman, P. S.; Pine, L.; Bell, S. Production of superoxide and hydrogen peroxide in medium used to culture Legionella pneumophila: catalytic decomposition by charcoal. *Applied and Environmental Microbiology* **1983**, *45* (3), 784–791.
(221) Kuzmanovic, D. A.; Elashvili, I.; Wick, C.; O'Connell, C. Bacteriophage MS2: molecular weight and spatial distribution of the protein and RNA components by small-angle neutron scattering and virus counting. *Structure* **2003**, *11* (11), 1339–1348.
(222) Calendar, R. *The Bacteriophages*; Oxford University Press on Demand, 2006.
(223) Wentsel, R. S.; O'Neill, P. E.; Kitchens, J. F. Evaluation of coliphage detection as a rapid indicator of water quality. *Applied and Environmental Microbiology* **1982**, *43* (2), 430–434.
(224) Herrmann, J. Persistence of enteroviruses in lake water. *J. Appl. Microbiol.* **1974**, *28* (5), 895–896.
(225) Allwood, P. B.; Malik, Y. S.; Hedberg, C. W.; Goyal, S. M. Survival of F-Specific RNA Coliphage, Feline Calicivirus, and Escherichia coli in Water: a Comparative Study. *Applied and Environmental Microbiology* **2003**, *69* (9), 5707–5710.
(226) Batch, L. F.; Schulz, C. R.; Linden, K. G. Evaluating water quality effects on UV disinfection of MS2 coliphage. *Journal American Water Works Association* **2004**, *96* (7), 75–87.
(227) Durborow, R. M.; Thune, R. L.; Hawke, J. P.; Camus, A. C. *Columnaris disease: a bacterial infection caused by Flavobacterium columnare*. *Southern*

Regional Aquaculture Center, Publication No. 479. Stoneville, …; US Department of Agriculture, 1998.
(228) Olin, P. G. *National Aquaculture Sector Overview. United States of America*; 2011; pp 1–11.
(229) Schrader, K. K.; Bommer, J. C.; Jori, G. In Vitro Evaluation of the Antimicrobial Agent AquaFrin as a Bactericide and Selective Algicide for Use in Channel Catfish Aquaculture. *North American Journal of Aquaculture* **2010**, *72* (4), 304–308.
(230) Declercq, A. M.; Haesebrouck, F.; Van den Broeck, W.; Bossier, P.; Decostere, A. Columnaris disease in fish: a review with emphasis on bacterium-host interactions. *Vet. Res.* **2013**, *44* (1).
(231) Welker, T. L.; Shoemaker, C. A.; Arias, C. R.; Klesius, P. H. Transmission and detection of Flavobacterium columnare in channel catfish Ictalurus punctatus. *Diseases of Aquatic Organisms* **2005**, *63* (2-3), 129–138.
(232) Thomas Jinu, S.; Goodwin, A. E. Acute columnaris infection in channel catfish, Ictalurus punctatus (Rafinesque): efficacy of practical treatments for warmwater aquaculture ponds. *Journal of Fish Diseases* **2004**, *27* (1), 23–28.
(233) Leonard, N.; Blancheton, J. P.; Guiraud, J. P. Populations of heterotrophic bacteria in an experimental recirculating aquaculture system. *Aquacultural Engineering* **2000**, *22* (1-2), 109–120.
(234) Mamane, H.; Shemer, H.; Linden, K. G. Inactivation of E. coli, B. subtilis spores, and MS2, T4, and T7 phage using UV/H2O2 advanced oxidation. *Journal of Hazardous Materials* **2007**, *146* (3), 479–486.
(235) von, G. U. Ozonation of drinking water: Part II. Disinfection and by-product formation in presence of bromide, iodide or chlorine. **2003**, *37* (7), 1469–1487.
(236) Cervero-Aragó, S.; Sommer, R.; Araujo, R. M. Effect of UV irradiation (253.7 nm) on free *Legionella* and *Legionella* associated with its amoebae hosts. *Water Research* **2014**, *67* (C), 299–309.
(237) Cohen-Yaniv, V.; Narkis, N.; Armon, R. Photocatalytic inactivation of Flavobacterium and E. coli in water by a continuous stirred tank reactor (CSTR) fed with suspended/immobilised TiO 2medium. *Water Science & Technology* **2008**, *58* (1), 247–6.
(238) Rattanakul, S.; Oguma, K. Analysis of Hydroxyl Radicals and Inactivation Mechanisms of Bacteriophage MS2 in Response to a Simultaneous Application of UV and Chlorine. *Environ. Sci. Technol* **2017**, *51* (1), 455–462.
(239) Stone, V.; Donaldson, K. Nanotoxicology - Signs of stress. *Nature Nanotech* **2006**, *1* (1), 23–24.
(240) Long, T. C.; Saleh, N. B.; Tilton, R. D.; Lowry, G. V.; Veronesi, B. Titanium Dioxide (P25) Produces Reactive Oxygen Species in Immortalized Brain Microglia (BV2): Implications for Nanoparticle Neurotoxicity †. *Environ. Sci. Technol.* **2006**, *40* (14), 4346–4352.
(241) Burello, E.; Worth, A. P. A theoretical framework for predicting the oxidative

stress potential of oxide nanoparticles. *Nanotoxicology* **2011**, *5* (2), 228–235.
(242) Arguinzoniz, A. G.; Ruggiero, E.; Habtemariam, A.; Hernández-Gil, J.; Salassa, L.; Mareque-Rivas, J. C. Light Harvesting and Photoemission by Nanoparticles for Photodynamic Therapy. *Part. Part. Syst. Charact.* **2013**, *31* (1), 46–75.
(243) Daimon, T.; Nosaka, Y. Formation and Behavior of Singlet Molecular Oxygen in TiO 2Photocatalysis Studied by Detection of Near-Infrared Phosphorescence. *J. Phys. Chem. C* **2007**, *111* (11), 4420–4424.
(244) Hirakawa, K.; Hirano, T. Singlet oxygen generation photocatalyzed by TiO2 particles and its contribution to biomolecule damage. *Chemistry Letters* **2006**, *35* (8), 832–833.
(245) Sharma, P.; Jha, A. B.; Dubey, R. S.; Pessarakli, M. Reactive Oxygen Species, Oxidative Damage, and Antioxidative Defense Mechanism in Plants under Stressful Conditions. *Journal of Botany* **2012**, *2012* (1), 1–26.
(246) Brunet, L.; Lyon, D. Y.; Hotze, E. M.; Alvarez, P. J. J.; Wiesner, M. R. Comparative Photoactivity and Antibacterial Properties of C 60Fullerenes and Titanium Dioxide Nanoparticles. *Environ. Sci. Technol.* **2009**, *43* (12), 4355–4360.
(247) Buettner, G. R. The Pecking Order of Free-Radicals and Antioxidants - Lipid-Peroxidation, Alpha-Tocopherol, and Ascorbate. *Arch. Biochem. Biophys.* **1993**, *300* (2), 535–543.
(248) Strehlow, W. H.; Cook, E. L. Compilation of Energy Band Gaps in Elemental and Binary Compound Semiconductors and Insulators. *Journal of Physical and Chemical Reference Data* **1973**, *2* (1), 163–200.
(249) Xu, Y.; Schoonen, M. A. A. The absolute energy positions of conduction and valence bands of selected semiconducting minerals. *American Mineralogist* **2000**, *85* (3-4), 543–556.
(250) Butler, M. A.; Ginley, D. S. Prediction of Flatband Potentials at Semiconductor-Electrolyte Interfaces from Atomic Electronegativities. *Journal of The Electrochemical Society* **1978**, *125* (2), 228–232.
(251) Ozawa, M.; Hattori, M. Ultrasonic vibration potential and point of zero charge of some rare earth oxides in water. *Journal of Alloys and Compounds* **2006**, *408-412*, 560–562.
(252) Dagenais, K.; Chamberlin, M.; Constantin, C. Modeling Energy Band Gap as a Function of Optical Electronegativity for Binary Oxides. *Journal of Young Investigators* **2013**, *25* (3), 1–6.
(253) Li, Y.; Zhang, W.; Niu, J.; Chen, Y. Mechanism of Photogenerated Reactive Oxygen Species and Correlation with the Antibacterial Properties of Engineered Metal-Oxide Nanoparticles. *ACS Nano* **2012**, *6* (6), 5164–5173.

Vita

Jaime Plazas-Tuttle was born in Bogotá, Colombia. After graduating from Colegio El Triángulo (Rionegro, Antioquia, Colombia), he earned his Bachelor's Degree in Civil Engineering from Pontificia Universidad Javeriana in 2000. In 2003, he obtained a Master of Science in Water Resources and Management from Ben Gurion University of the Negev (Sde Boker, Israel). During his M.S. studies Jaime evaluated the performance of an immersed ultrafiltration membrane for the treatment of dairy wastewater. After graduating, Jaime entered as an instructor professor at Universidad de los Andes (Bogotá, Colombia) where he taught undergraduate level courses for three consecutive years, after which he was appointed as Civil and Environmental Engineering Undergraduate Coordinator and Faculty Advisor for two more years. Jaime continued his journey of higher education after obtaining a Fulbright Scholarship in 2009. Later that same year, he joined the master's program in Civil Engineering at the University of Illinois at Urbana-Champaign. He obtained his second M.S. in Civil Engineering in Environmental Engineering in 2012. In the fall of 2012, Jaime joined Dr. Navid Saleh's research group at the University of South Carolina (Columbia, SC), to begin his journey to a Ph.D., and in January 2014 he transferred to the University of Texas at Austin, where his Ph.D. advisor joined as an Assistant Professor.

Permanent email address: jplazas@hotmail.com

This dissertation was typed by the author.